Light Water Reactor Sustainability Program

Status Update on the Long-Term Crack Initiation Testing of Alloy 690 and Its Weld Metals in PWR Primary Water

Ziqing Zhai
Mychailo Toloczko
Pacific Northwest National Laboratory
David Sprouster
Stony Brook University

June 2024

Status Update on the Long-Term Crack Initiation Testing of Alloy 690 and Its Weld Metals in PWR Primary Water

Ziqing Zhai
Mychailo Toloczko
Pacific Northwest National Laboratory

David Sprouster
Stony Brook University

June 2024

Page intentionally left blank

ABSTRACT

Determining the stress corrosion crack (SCC) initiation resistance and the aging behavior of high-Cr Ni-base Alloy 690 and its weld metals is needed to confirm their viability as the replacement materials for Alloy 600/182/82 and to ensure safe and economical power production over extended operation of light water reactors. This report provides a progress summary of research activities performed from October 2023 to June 2024 at Pacific Northwest National Laboratory (PNNL) to address these topics.

The first part of this report provides an update on the ongoing SCC initiation tests on Alloy 690 materials in 360°C simulated PWR primary water. Effects of selected material (thermal-mechanical history, starting microstructure, surface finish) and mechanical (applied stress, cold work) factors on grain boundary degradation and crack initiation are being investigated on forty specimens from seven commercial Alloy 690 heats. A progress update is also given on the collaboration with EPRI on long-term aging evaluation of LWRS Alloy 690 SCC initiation specimens using synchrotron X-ray diffraction. The second part of this report summarizes the testing and characterization results for the 1st-year creep testing of cold worked Alloy 690 specimens in 330, 360, and 400°C air, with the aim to better understand the mechanism and kinetics of creep-induced cavity evolution and accelerate data collection for predicting long-term behavior of Alloy 690 in service. The third part of this report provides an update on the long-term SCC initiation testing performed in collaboration with NRC on two blunt notch compact tension specimens machined from welding defects-containing Alloy 52/52M weld mockups. New insights obtained from these testing results to improve the mechanistic understanding of crack initiation in these alloys will be discussed and the implications on their long-term performance will be summarized.

Page intentionally left blank

ACKNOWLEDGEMENTS

CONTENTS

FIGURES

TABLES

Page intentionally left blank

ACRONYMS

AC	Air cool
AR	As-received
BNCT	Blunt notch compact tension
BSE	Backscatter electron
CF	Cold forged
CGR	Crack growth rate
CR	Cold rolled
CRDM	Control rod drive mechanism
CTS	Cold tensile strained
CW	Cold worked
DCPD	Direct current potential drop
DDC	Ductility dip cracking
EBSD	Electron backscatter diffraction
EPRI	Electric Power Research Institute
FIB	Focused ion beam
FY	Fiscal year
GB	Grain boundary
HAGB	High-angle grain boundary
IG	Intergranular
IGSCC	Intergranular stress corrosion cracking
LAS	Low alloy steel
LRO	Long range ordering
LWR	Light water reactors
MA	Mill annealed
NNL	Naval Nuclear Laboratory
NRC	Nuclear Regulatory Commission
PFIB	Plasma focused ion beam
PNNL	Pacific Northwest National Laboratory
PWR	Pressurized water reactor
RT	Room temperature
SA	Solution annealed
SCC	Stress corrosion cracking
SEM	Scanning electron microscopy
SXRD	Synchrotron X-ray diffraction
TG	Transgranular
TT	Thermally treated
WQ	Water quench
XCT	X-ray computed tomography
YS	Yield stress

Page intentionally left blank

Status Update on the Long-Term Crack Initiation Testing of Alloy 690 and Its Weld Metals in PWR Primary Water

1.   Project Background

1.1   Objective

The first objective of the LWRS task at Pacific Northwest National Laboratory (PNNL) is to identify underlying mechanisms controlling stress corrosion cracking (SCC) initiation and other possible long-term degradation modes that can potentially degrade SCC resistance in Ni-base alloys. Understanding and modeling the fundamental processes causing crack nucleation is a key step in predicting and mitigating SCC in the primary and secondary water systems of light water reactors (LWRs). It is also important to understand the long-term microstructural stability and performance of these alloys as a crucial step moving forward to fulfill their promise for broader applications in LWRs. Mechanistic information obtained could provide key insights to mitigate or control SCC in these materials, optimize inspection and maintenance schedules for the most susceptible materials and locations, and potentially define SCC-resistant materials. The second objective of this task is to evaluate the impact of emerging technologies proposed for sustaining reliable and economical operation of LWRs on SCC resistance of Ni-base alloys. The research scope is defined with regulatory and industry needs and is linked to state-of-the-art laboratory testing and microscopic characterizations.

1.2   Focus of Current Report

The first part of this report provides an update on the ongoing SCC initiation test on cold work (CW) Alloy 690 materials in 360°C simulated pressurized water reactor (PWR) primary water. Effects of selected material (thermal-mechanical history, starting microstructure, surface finish) and mechanical (applied stress, cold work) factors on grain boundary degradation and crack initiation are being investigated on forty specimens from seven commercial Alloy 690 heats. A progress update is also given on the collaboration with the Electric Power Research Institute (EPRI) on long-term aging evaluation of LWRS Alloy 690 SCC specimens using synchrotron X-ray diffraction. The second part of this report summarizes the testing and characterization results for the first year creep testing of cold worked Alloy 690 specimens in air at 330, 360, and 400°C. The objective of this testing is to better understand the mechanism and kinetics of creep-induced cavity evolution and to accelerate data collection for predicting the long-term behavior of Alloy 690 in service. The third part of this report provides an update on the long-term SCC initiation testing performed in collaboration with the U.S. Nuclear Regulatory Commission (NRC) on two blunt notch compact tension specimens machined from welding defects-containing Alloy 52/52M weld mockups. New insights obtained from these testing results to improve the mechanistic understanding of crack initiation in these alloys will be discussed and the implication on their long-term performance will be summarized.

Page intentionally left blank

2. SCC Initiation Testing of Cold Worked Alloy 690

2.1 Chapter Overview

SCC initiation testing on CW Alloy 600 in PWR primary water has demonstrated that intergranular (IG) oxidation is the precursor to SCC initiation in this material [1-3]. In comparison, an equivalent degradation and cracking process does not exist in CW Alloy 690. Due to a much higher Cr content in alloy composition, a compact chromia layer readily forms on the surface above grain boundaries (GBs) intersecting the surface when the material is exposed to high-temperature water. This chromia layer remains protective after long-term exposure to high stresses. As a result, CW Alloy 690 is considered resistant to SCC initiation. However, recent laboratory studies have revealed an alternate mechanism of crack initiation in this material through the formation and growth of GB cavities induced by creep when the material is highly cold worked [4-9]. To better understand the evolution of GB cavities and to predict the degradation of Alloy 690 in realistic PWR operating conditions, systematic long-term SCC initiation testing is being performed at PNNL to evaluate factors influencing GB cavity evolution in Alloy 690 materials. Seven commercial Alloy 690 heats with variations in thermal-mechanical history (solution annealed (SA), mill annealed (MA), and thermally treated (TT)), cold work level (12–31%), and applied stress (1.0 vs. 0.9 yield stress (YS)) are being investigated. To date, the test consists of five phases with ~1-year exposure for Phase I–III, 2-year exposure for Phase IV, and ongoing Phase V. Precursor damage and crack morphology observed during the test interruption after each of the first four phases were reported in detail in previous milestone reports [10-13]. This chapter will provide a status update on the ongoing Phase V testing and a new task made possible this fiscal year in collaboration with EPRI to perform synchrotron X-ray diffraction (SXRD) on selected SCC initiation specimens to study the long-term aging behavior of Alloy 690.

2.2 Experimental

2.2.1 Materials

Three Alloy 690 control rod drive mechanism (CRDM) heats and four plate/bar heats are being investigated in this project. The chemical composition and heat treatment history for each heat in the as-received condition are listed in Tables 1 and 2. Prior to testing, the materials were either cold-forged (CF) in the direction orthogonal to the processing plane or cold-rolled (CR) along the processing direction to produce a cold work level ranging from 12 to 31% reduction in thickness (Figure 1). Most combinations of these material and cold work conditions had already been evaluated for SCC growth behavior as part of an NRC project at PNNL, where six of the seven heats (except Allvac X87N-1) in the 20-30%CW condition exhibited moderate-to-high SCC crack growth rates in simulated PWR primary water (Figure 2[14]). Pre-testing microstructures were characterized for these materials in both the as-received (AR) and CW conditions, which are summarized in Sections 2.2.1.1 and 2.2.1.2 to facilitate results interpretation in the latter sections.

Table 1.   Composition of the AR Alloy 690 materials.

Source/Manufacturer and Heat #	Composition, wt%
Valinox/Valinox RE243 CRDM Tube 2360	Ni-28.9Cr-10.4Fe-0.02C-0.3Mn-0.35Si-0.14Al-0.23Ti-0.024N-0.008P-0.0005S
EPRI/Sumitomo E67074C CRDM Tube	Ni-29.8Cr-9.8Fe-0.02C-0.29Mn-0.23Si-0.03Cu-0.0002S
EPRI/TK-VDM (Doosan) 133454 CRDM Bar	Ni-29.1Cr-8.9Fe-0.020C-0.26Mn-0.29Si-0.26Al-0.32Ti-0.01Cu-0.02N-0.005P-<0.002S-0.002B
ANL/Special Metals NX3297HK12 plate	Ni-29.5Cr-9.9Fe-0.03C-0.20Mn-0.07Si-0.01Cu-<0.001S
GEG/Allvac B25K bar	Ni-29.3Cr-9.2Fe-0.034C-0.22Mn-0.06Si-0.26Al-0.37Ti-<0.01Cu-0.03N-0.006P-<0.0003S-<0.001B
EPRI/TK-VDM 114092 plate	Ni-29.5Cr-9.5Fe-0.020C-0.25Mn-0.26Si-0.32Al-0.36Ti-<0.01Cu-0.003P-<0.002S
EPRI/Allvac X87N-1	Ni-30.0Cr-9.2Fe-0.020C-0.20Mn-0.05Si-<0.01Cu-<0.0003S

Table 2.   Heat treatment and mechanical properties of the AR Alloy 690 materials (RT: room temperature, WQ: water quenched, AC: air cool, NM: not measured).

Source/Manufacturer and Heat #	Heat Treatments	RT Yield Stress (MPa)	Hardness (HV)
Valinox/Valinox RE243 CRDM Tube 2360	1122°C/~1 min, WQ + 716-725°C/10.5 h, AC	255	157
EPRI/Sumitomo E67074C CRDM Tube	Anneal + 725°C/10 h/AC	NM	NM
EPRI/TK-VDM (Doosan) 133454 CRDM Bar	1045°C/4 h/WQ + 720°C/10 h/AC	263	165
ANL/Special Metals NX3297HK12 plate	1038°C/2 h/AC	NM	173
GEG/Allvac B25K bar	996°C/20 min/AC	294	173
EPRI/TK-VDM 114092 plate	1030°C/1 h/WQ + 715°C/10 h/AC	285	155
EPRI/Allvac X87N-1	1030°C/4 h/WQ +727°C/5 h/AC	265	NM
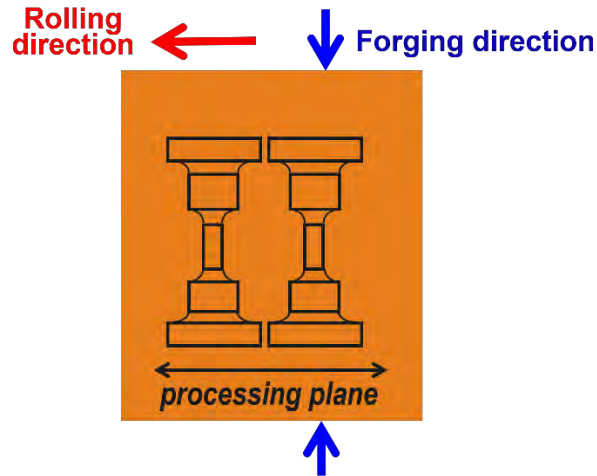
Figure 1. Illustration showing the orientation of specimens and cold work direction in the Alloy 690 materials.
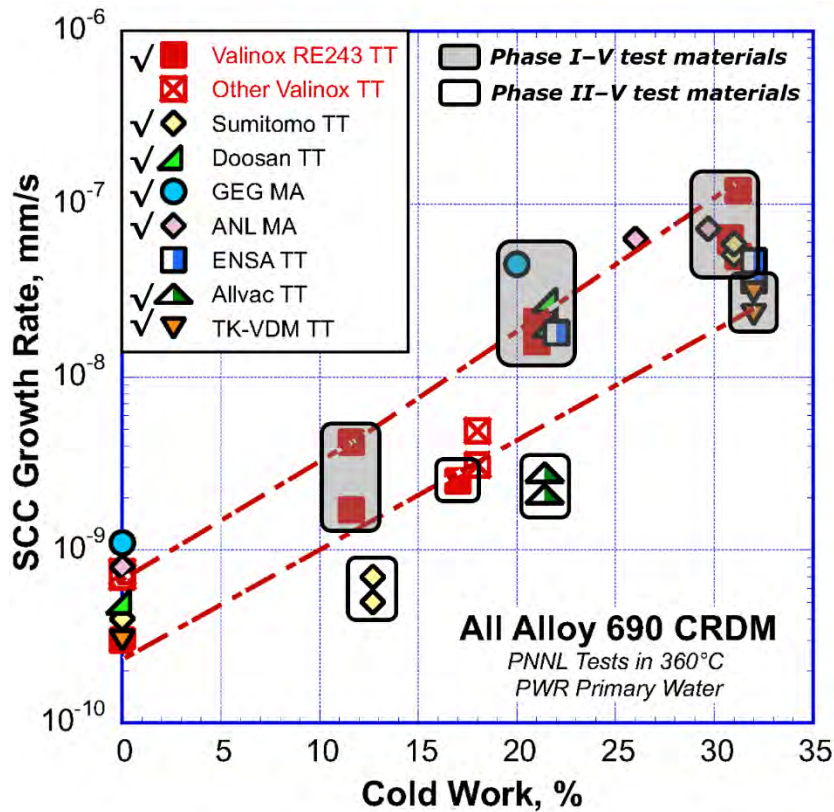
Figure 2. SCCGR response of TT/MA Alloy 690 materials at ~30 MPa√m acquired from the NRC SCC crack growth program [14, 15]. The heat and cold work levels selected for SCC initiation evaluation at each stage were checked in the label box and circled in the plots.

2.2.1.1   As-Received Alloy 690 Microstructures

Alloy 690 is usually MA or TT for plant applications, which introduces carbide precipitation in the matrix or at high-angle grain boundaries (HAGBs). In all the tested Alloy 690 heats, carbide precipitation

was limited to a few isolated GBs in the MA GEG B25K bar heat with a planar banded microstructure. All the other heats exhibit a semi-continuous GB carbide coverage, but the size and spacing between carbides vary significantly from heat to heat, as shown in the scanning electron microscopy (SEM) backscatter electron (BSE) images in Figure 3 for the CRDM tubing materials and in Figure 4 for the plate/bar materials. The TT CRDM tubing heats Sumitomo E67074C and Valinox RE243 exhibit the most uniform and closely spaced small, sub-micrometer carbides, while the TT plate heat TK-VDM 114092 exhibits similar size carbides but an up-to-10 times larger spacings in between. In comparison, the TT CRDM bar heat Doosan 133454 and MA plate heat ANL HK3297HK12 have much larger, micrometer-sized IG carbides that are more widely spaced. The MA ANL plate heat also features a unique distribution of extensive intragranular TiN particles.

Electron backscatter diffraction (EBSD) pattern quality maps were also acquired on these materials to document grain orientations and size. As shown in the pattern quality maps in Figure 5, the CRDM materials generally have a larger grain size than the plate/bar materials. The Valinox and Doosan CRDM materials have a similar grain size of ~90 μm, while the Sumitomo CRDM has a smaller average grain size of ~35 μm with significant twinning. The TK-VDM plate material has a similar grain size to Sumitomo CRDM but much less twinning. The ANL and Allvac plate materials have the same average grain size of ~25 μm, and the GEG bar material exhibits the finest microstructure with an average grain size of ~15 μm. The grain size measurements did not count the twining boundaries. Table 3 provides a more detailed summary of the grain size and carbide distribution for all the Alloy 690 CRDM and plate/bar heats currently being evaluated in the SCC initiation test.
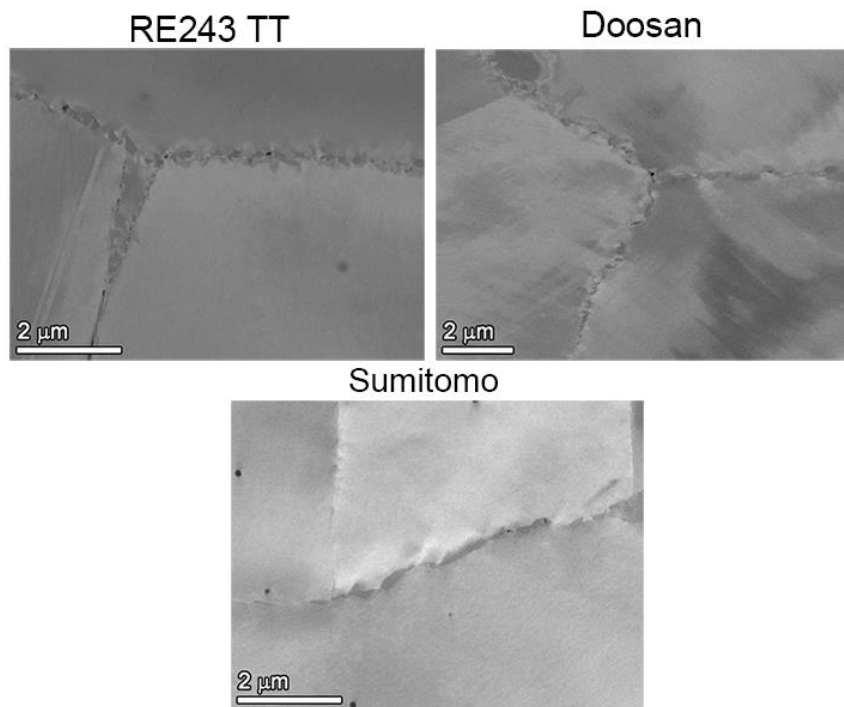
Figure 3.   SEM-BSE images illustrating the GB microstructures for the three Alloy 690TT CRDM materials in the as-received condition.
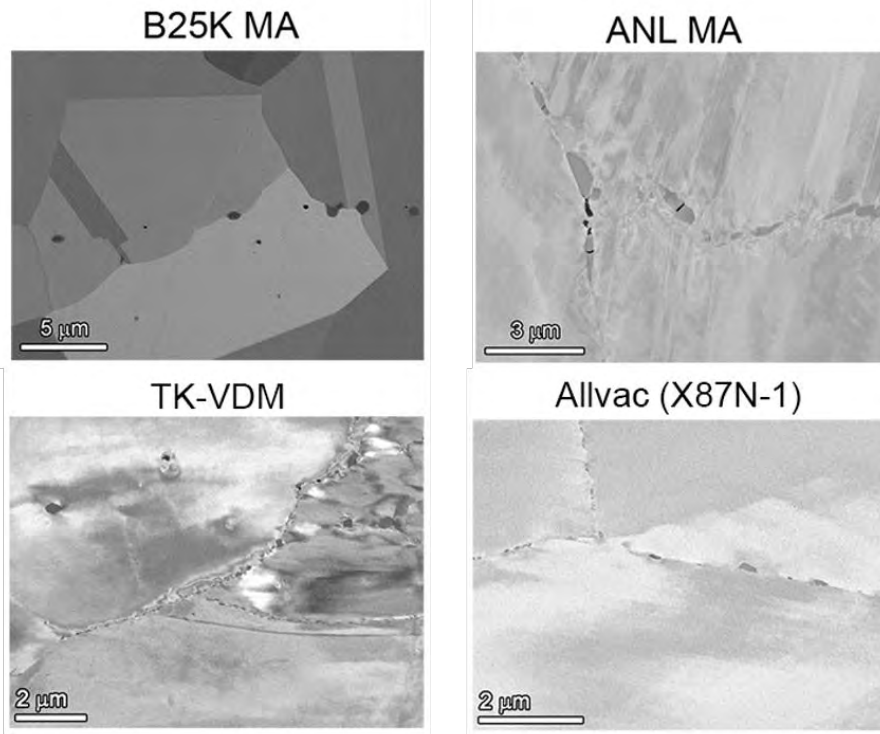
Figure 4. SEM-BSE images illustrating differences in the GB carbide microstructures for each of the four Alloy 690 plate/bar materials in the as-received condition.
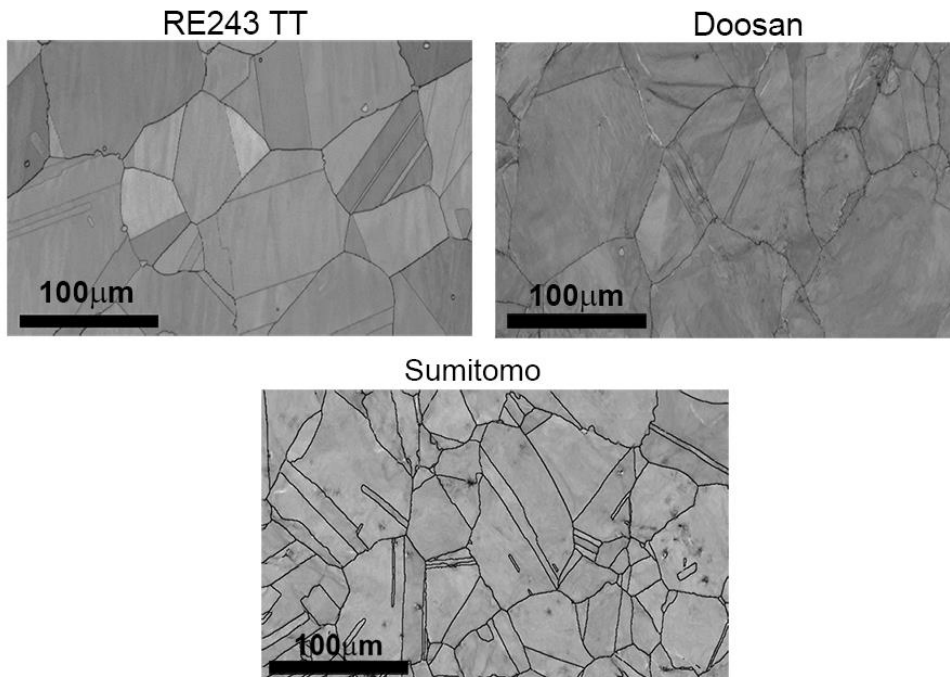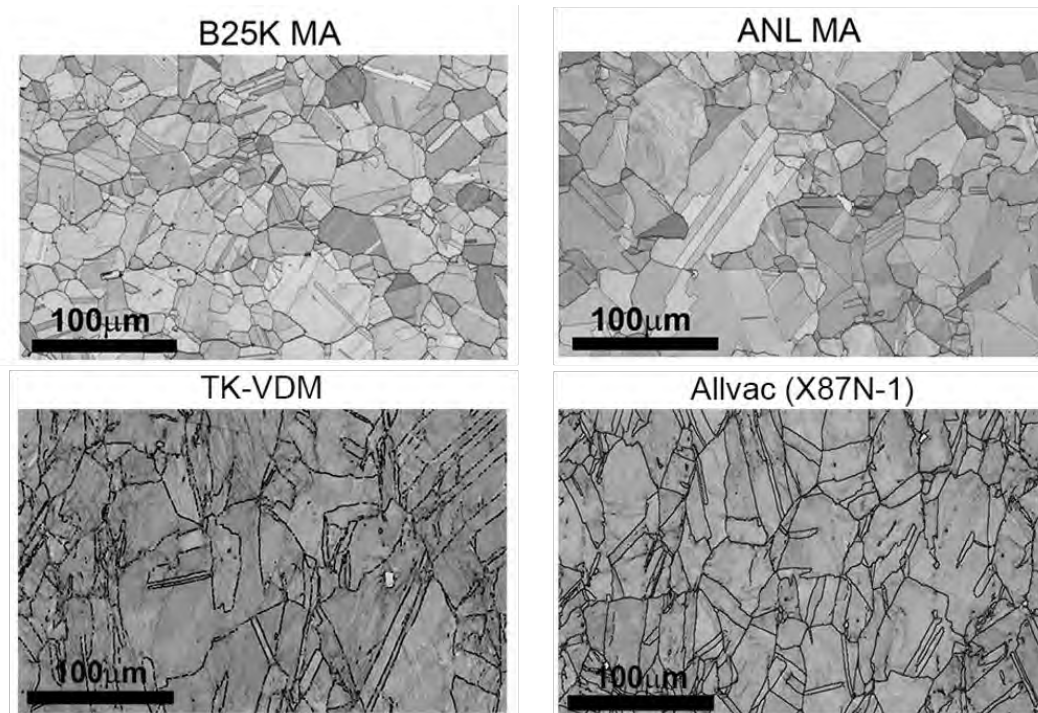
Figure 5. EBSD pattern quality maps showing the general microstructure and grain size for the seven Alloy 690TT/MA materials in the as-received condition.

Table 3. Summary of grain size and carbide distributions for materials selected for SCC initiation testing.

Material	Grain Size (µm)	Carbide Location, Size	GB Carbide Density
CRDM Materials			
Valinox RE243 TT	~90	IG, 50–200 nm	Semi-continuous, spacing ~100 nm
Doosan 133454 TT	~90	IG, 1–5 µm	Semi-continuous, spacing ~0.5–2 µm
Sumitomo E67074C TT	~35-40	IG, 50–300 nm	Semi-continuous, spacing ~100 nm
Plate/Bar Materials			
GEG B25K MA	~10-15	TG and isolated IG, 1–3 µm	Low
ANL HK3297HK12 MA	~20-25	IG, 0.5–3 µm	Semi-continuous, spacing ~0.2–2 µm
TK-VDM 114092 TT	~35-40	IG, 50-200 nm	Semi-continuous, spacing ~0.1–0.5 µm
Allvac X87N-1 TT	~20-25	IG, 50-200 nm	Semi-continuous, spacing ~200 nm

2.2.1.2   *Permanent Damage in CW Alloy 690 Materials*

It is important to note that the pre-test cold work introduced permanent damage in all CW materials. This damage was present at GBs in the form of cavities and cracked precipitates, of which the size and density strongly depend on the GB carbide distribution. An example is shown in Figure 6, where the permanent damage induced by cold work in four 31%CF Alloy 690TT materials is highlighted. The images are shown at the same scale, directly comparing the size and distribution of cavities and cracks between these heats. The materials exhibiting fine carbides at GBs often feature small voids at a higher density on certain boundaries. In comparison, the damage in the materials having larger and more widely spaced carbides is also larger and more spaced out. In addition, an obvious increase was noted in the density of these pre-existing defects as the cold work level increased. In Figure 7, representative pre-existing defect distribution produced by cold forging the Valinox CRDM Alloy 690TT material to different cold work levels are presented at the same scale to facilitate comparison. The images are shown at locations in each specimen where multiple IG voids and cracked carbides were identified. Such locations became increasingly more difficult to find as the cold work level decreased, where the number and size of the IG defects also dopped with decreasing cold work. All the other Alloy 690 TT/MA materials showed a similar trend. The degree of cold work-induced damage is qualitatively summarized for the CRDM materials in Table 4 and for plate/bar materials in Table 5, respectively.
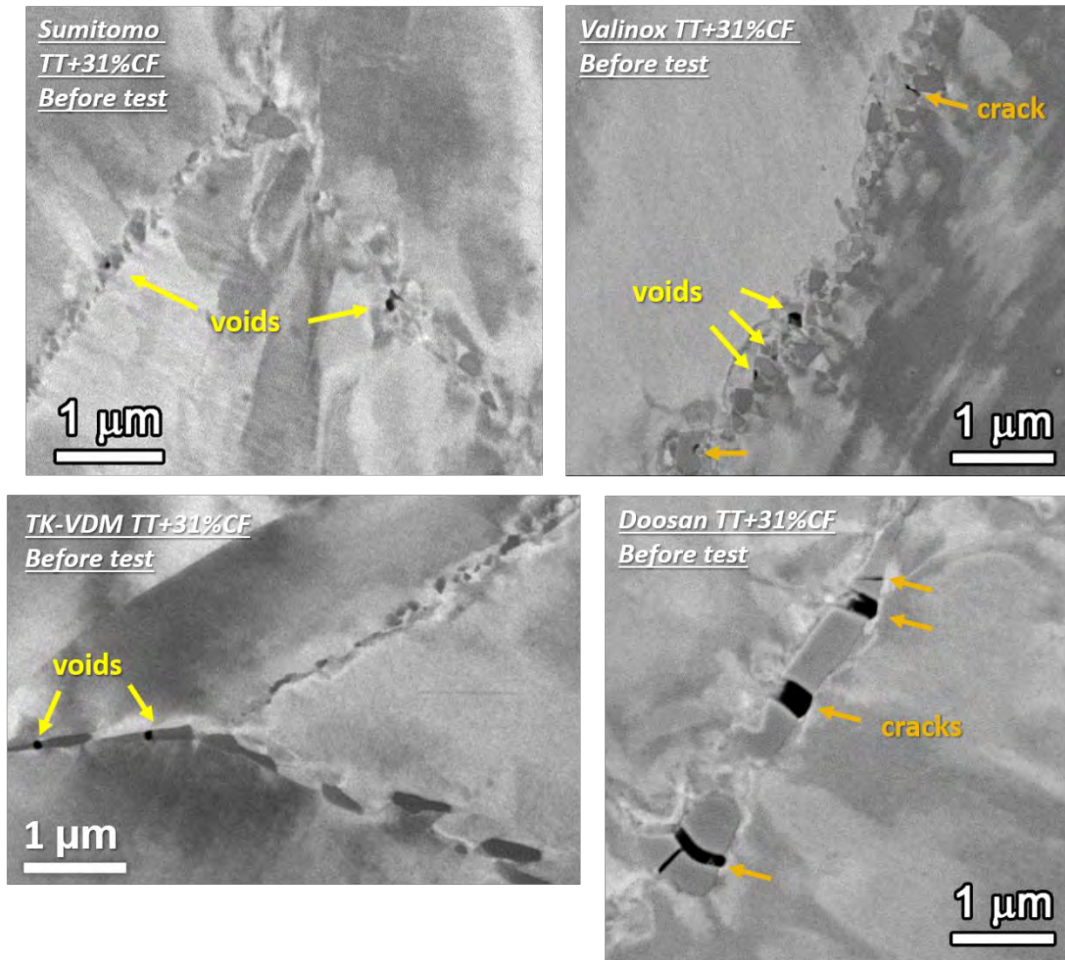
Figure 6.   SEM-BSE images illustrating the permanent damage (highlighted by arrows) induced by cold work in four 31%CF Alloy 690TT materials. All images are shown at the same scale.
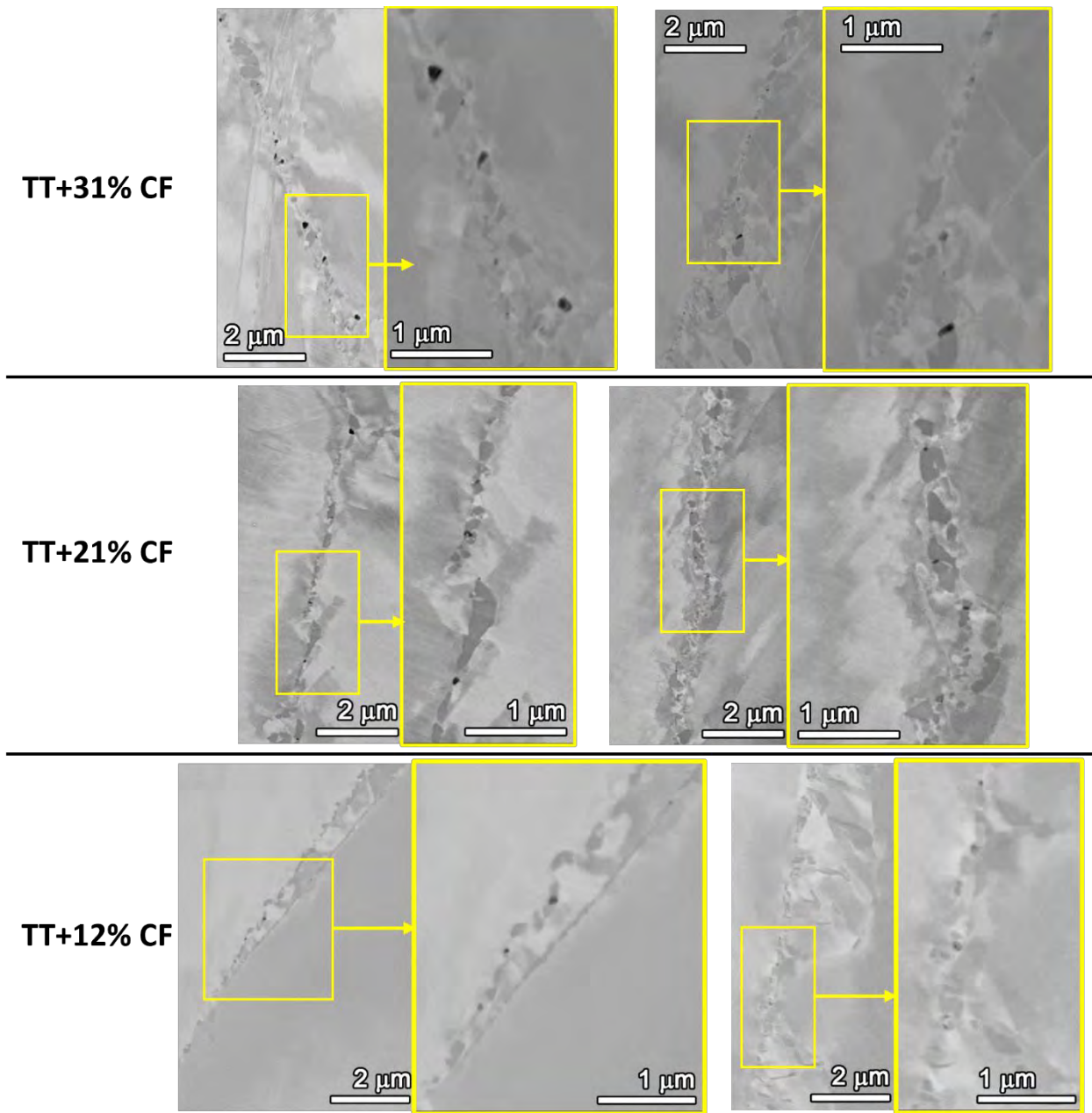
Figure 7.   Representative pre-existing defect distribution in the thermally treated Valinox CRDM material cold forged to 12, 21, and 31% reduction in thickness.

Table 4. Summary of carbide microstructure and damage morphology in Alloy 690TT CRDM materials in different cold work levels evaluated in the SCC initiation test.

Material	AR GB Carbide Microstructure		Cold Work Induced GB Damage	
	Location, Size	Density, Spacing	Density of Cracked GB Precipitates	IG Void Density
Valinox RE243 12% CF	IG, 50–200 nm	Semi-continuous, spacing ~100 nm	None–Low	Low
Valinox RE243 21% CF			Low	Low–Moderate
Valinox RE243 31% CF			Low	Moderate
Sumitomo E67074C 21% CF	IG, 50–200 nm	Semi-continuous, spacing ~100 nm	Low	Low–Moderate
Sumitomo E67074C 31% CF			Low	Moderate
Doosan 133454 21% CF	IG, 1–5 µm	Semi-continuous, spacing ~0.5–2 µm	Low	Low–Moderate
Doosan 133454 31% CF			Low	Moderate

Table 5. Summary of carbide microstructure and damage morphology in Alloy 690 plate and bar materials in different cold work levels evaluated in the SCC initiation test.

Material	AR GB Carbide Microstructure		Cold Work Induced GB Damage	
	Location, Size	Density, Spacing	Density of Cracked GB Precipitates	IG Void Density
ANL MA 26% CR	IG, 0.5–3 µm	Semi-continuous, spacing ~0.2–2 µm	Moderate	Moderate–High
GEG MA 18% CR	Primarily TG, 1–3 µm	Low density, unevenly distributed	None–Low	None–Low
TK-VDM 114092 22% CF	IG, 50–200 nm	Semi-continuous, spacing ~0.2–0.5 µm	Low	Low–Moderate
TK-VDM 114092 31.9% CF			Low	Moderate
Allvac X87N-1 31% CF	IG, 50-200 nm	Semi-continuous, spacing ~0.2–0.5 µm	Low-Moderate	Moderate

2.2.2 Test Method

The SCC initiation testing is performed in state-of-the-art multi-specimen autoclave systems equipped with an active loading unit, a flow loop for water chemistry control, and in-situ direct current potential drop (DCPD) monitoring for crack initiation.

30.4 mm (1.2-inch) tall uniaxial tensile specimens are used for the tests (Figure 8). All specimens have an identical gauge length of 4 mm. A precision servo-electric load control system applies the load on the loading string(s) using a target load of 4670 N (~1050 lbs). Different stress levels can be achieved by varying the gauge diameter in the specimens loaded in the same string, allowing multiple specimens to be tested at their yield stress (YS) or any other target stress. For most specimens, a 1 µm surface finish was prepared to facilitate the examination of precursor damage and cracks on the surface.
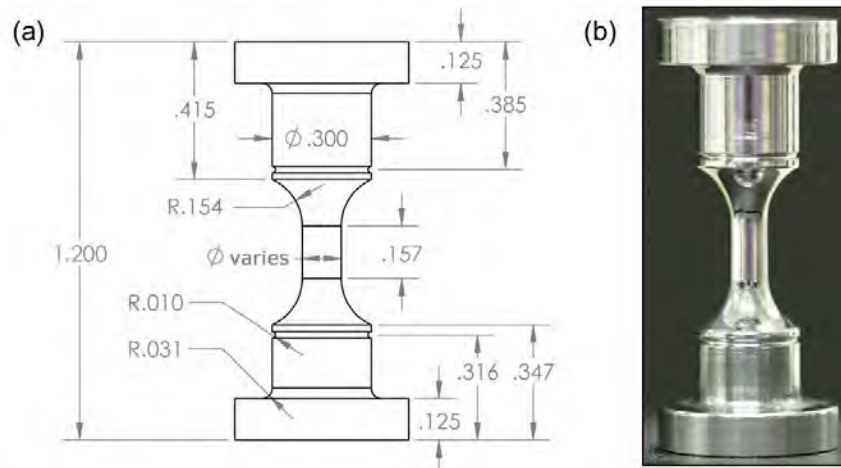
Figure 8.   PNNL initiation specimen design. The gauge diameter is selected based on material strength and can vary from 2.75-4.5 mm (0.11-0.18 inches). The gauge length is set at 4.0 mm (0.157 inches). Overall height is 30.5 mm (1.2 inches). Illustrated dimensions are in inch units.

Figure 9 shows the load train and DCPD instrumentation for the serially loaded SCC initiation specimens set up at PNNL. Currently, one large SCC initiation system (denoted as LWRS1 hereafter) and two medium-size SCC initiation systems (denoted as LWRS2 and LWRS3 hereafter) are being used under the scope of LWRS. LWRS1 allows 36 specimens to be tested simultaneously with up to 12 specimens instrumented. LWRS2 and LWRS3 each can test up to 6 fully instrumented specimens. A reversing DCPD technique developed by General Electric [16] was adapted for online monitoring of SCC initiation behavior based on original work by NNL [17]. Details of the PNNL approach were provided in previous publications [1, 18].

The CW Alloy 690 specimens are tested at either 100% or 90% of the material's yield strength. The load-up is usually completed within one week after the test system reaches the test temperature and pressure. At the start of a test, the target load (the load at ~0.2% plastic strain) was achieved over 1–2 hours at a constant strain rate of ~1×10^{-5} s^{-1}. This displacement rate allows monitoring of the strain evolution by DCPD with a sufficiently low noise level. For example, in Figure 10, some specimens may yield slightly earlier than others in a multi-specimen load train system due to intrinsic differences in yield strength and/or gauge diameter. In such a case, small amounts of plastic strain up to ~1.5% are allowed in these specimens to achieve a minimum of 0.15% plastic strain in the others. The specimens are then held at an actively controlled constant load until DCPD detects crack initiation. All relevant environmental parameters and DCPD data are monitored and periodically saved to a file. If a test is interrupted for specimen examinations or to remove an initiated specimen, the remaining specimens will be returned to their original load after the test restarts following the same steps described above. Figure 11 shows the evolution of both the non-referenced and the referenced strains throughout the exposure of an Alloy 600 specimen. As mentioned above, by subtracting the reference voltage from the gauge voltage, the contributions of resistivity drift and creep are largely eliminated in the referenced strain response. While cracking and some amount of creep contribute to the observed DCPD response simultaneously, the crack initiation time is determined when an apparent increase occurs in the strain rate above the noise level. This is thought to be the onset of stable crack growth at engineering-relevant rates.

**(a) 6-Specimen
SCC Initiation System**
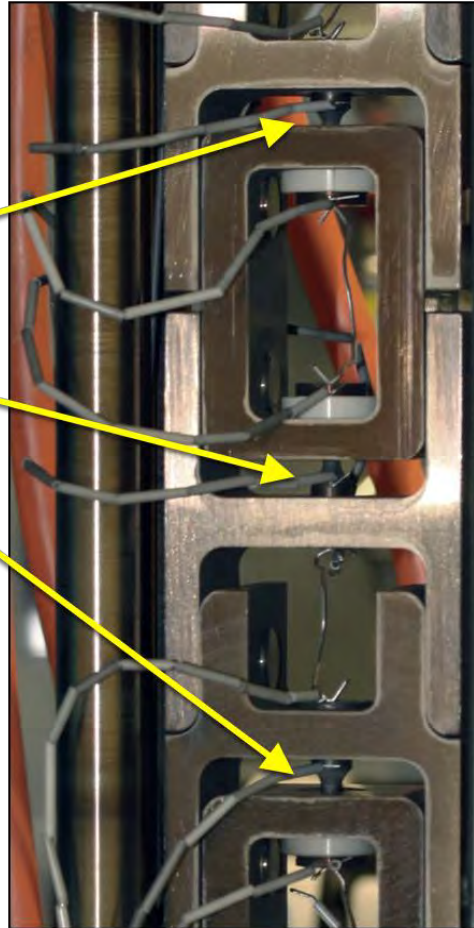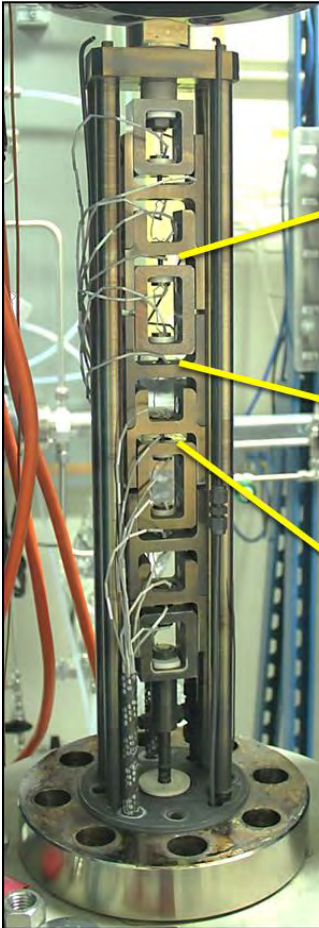
**(b) 36-Specimen
SCC Initiation System**

Figure 9. The load trains used at PNNL in the (a) medium-size SCC initiation test system with a capacity of testing up to 6 fully instrumented specimens and the (b) large-size SCC initiation test system, i.e., LWRS1, with a capacity of testing up to 12 instrumented specimens and up to 36 specimens in total.

LWRS - IN273-78 - 15% CF A600SA+TT NX6106XK-11, 1 μm Finish
360°C, 1000 ppm B, 2.0 ppm Li, 26 cc/kg H$_2$

actuator extension (in)
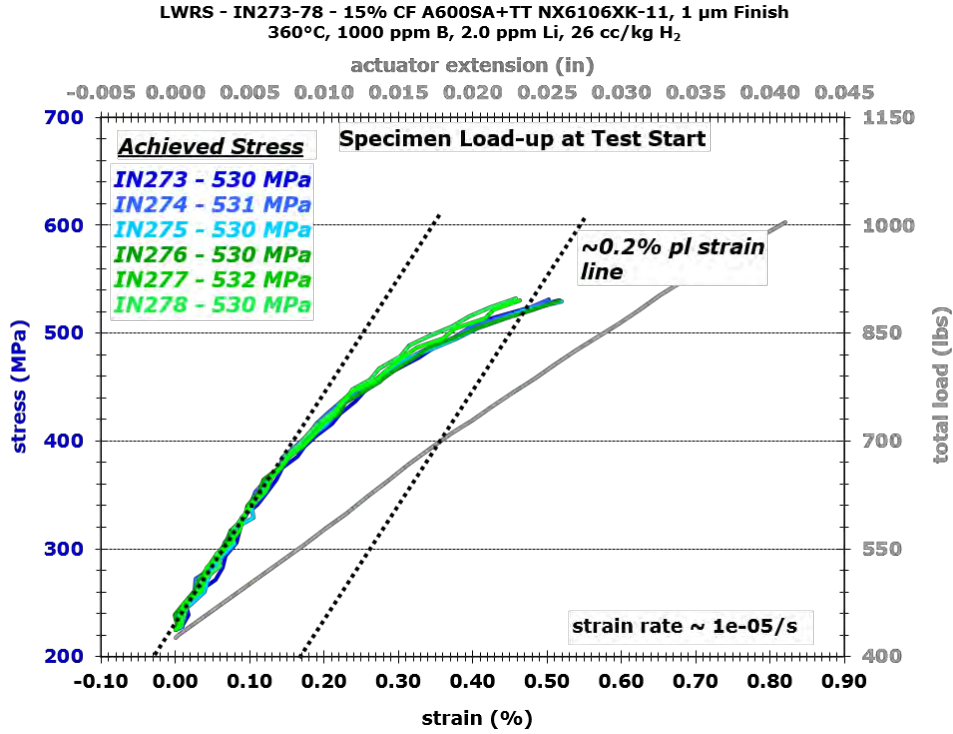
Figure 10. Example of stress versus strain plot during the initial loading of tensile specimens for SCC initiation testing. The displacement in the actuator and the total load are plotted in the secondary x (upper) and y (right) axes, respectively.

IN052- A600MA plate NX6106XK-11, 8% CTS, 1 μm finish
360°C, 1000 ppm B, 2.0 ppm Li, 25 cc/kg H$_2$
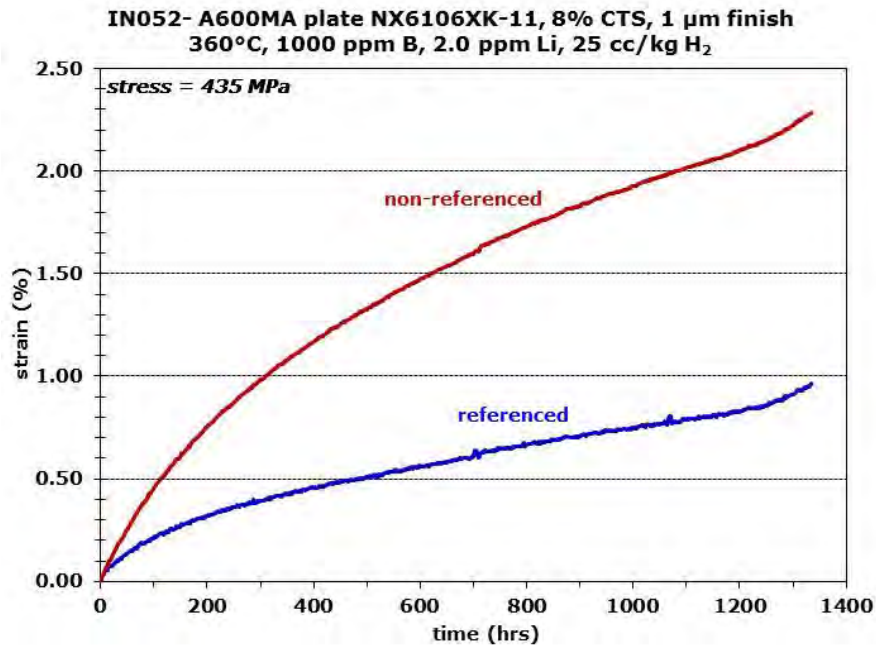
Figure 11. Non-referenced and referenced DCPD strain response for IN052, an 8% CW specimen from Alloy 600MA plate heat NX6106XK-11.

14

2.3   Results

2.3.1   Status Update of the Constant Load SCC Initiation Testing

Figure 12 provides an overview of the test progress specifying the heat and material conditions evaluated in each phase with their up-to-date exposure times. A more detailed status summary of all the tested and in-test specimens is provided in Table 6.

To date, the test consists of five phases. The exposure during the first three phases each lasted ~1.1 years. The original test materials were selected based on their SCC crack growth rate (CGR) response obtained in the NRC SCC crack growth program [14, 15] as summarized in Figure 2. The research started with three Alloy 690TT CRDM heats and three TT/MA plate/bar heats exhibiting high SCC crack growth rates at CW levels from 20–30%. These materials are being tested for SCC initiation in low (<15% deformation), moderate (15 to 25% deformation), and/or high (>25% deformation) cold work levels. Since surface-breaking short IG cracks were observed on the gauge surface of several highly CW Alloy 690TT specimens after Phase I exposure and were all found to be associated with GB cavity formation at crack tips, thirteen specimens were removed after Phase I exposure for destructive examination to document cavity distribution in bulk. Another thirteen new replacement specimens were added to the test at the start of Phase II exposure, expanding the test matrix to include more variations in GB carbide distribution (TT vs. SA), applied stress (100% vs. 90% YS), and heat IGSCC susceptibility (moderate-high CGR vs. low CGR in moderately-highly CW condition). Phase I and II exposures were conducted on thirty-six specimens in LWRS1. Seven specimens were removed after Phase II exposure, with another ten new specimens added at Phase III exposure. Beginning at Phase III, the specimens exposed for a longer time and considered more susceptible to GB cavity formation were moved to LWRS2, increasing the total specimens in the test to 39 for Phase III and 42 for Phase IV later. This gave more flexibility in stopping the test to remove specimens once crack initiation is detected, while exposure can continue in LWRS1 without disturbance. It also allows referenced DCPD response to be monitored on these specimens, thus providing a more accurate determination of crack initiation. Because most specimens tested in Phase IV were in conditions less susceptible to GB cavity formation and growth than the specimens that were already removed from the test, the Phase IV exposure lasted for two years in LWRS1. However, Phase IV exposure was stopped for the six specimens tested in LWRS2 after reaching one year of exposure. This is because to complete another task under this project, LWS2 was used in FY21 and FY22 to evaluate the effect of LiOH vs. KOH-containing PWR primary water on the SCC initiation response of Ni-base alloys [19, 20]. In the late summer of 2022, LWRS1 was stopped after Phase IV testing reached a total exposure of two years, not long after DCPD detected crack initiation in a Sumitomo CRDM TT+31%CF specimen IN179 tested at 0.9 YS. All the specimens were removed from the test for detailed surface examinations to document precursor damage evolution, and the result was reported in detail in last year's milestone report [21]. Phase V exposure began in January 2023 after the completion of the examinations. 35 specimens were tested in LWRS1, among which 12 were monitored in-situ by DCPD. Another 6 specimens were tested in LWRS2. At the time of this report, the specimens in LWRS1 accumulated another 7,907 hours (~0.9 year) of exposure and the specimens in LWRS2 accumulated another 10,261 hours (~1.2 years) of exposure at target stress. The DCPD non-referenced strain response in these two test systems are shown in Figures 13 and 14, respectively. The LWRS1 test time was shorter than LWRS2 because the test was stopped twice to remove two more specimens after macroscopic crack initiation was confirmed in them by DCPD (Figure 13). The latest test stop took place in March 2024 to remove the initiated specimen IN173. As part of the collaboration with EPRI, several other specimens were also temporarily removed from LWRS1 and LWRS2 for non-destructive sample preparation for SXRD measurements at Brookhaven National Laboratory. More details on the SXRD analysis on these specimens will be provided later in Section 2.3.2. In the meantime, to make test system available for the stainless steel SCC initiation testing proposed in the fiscal year (FY) 2024 plan, it was decided to only use LWRS1 for continued testing of Alloy 690 from this moment onward. As a result, three more specimens (IN175, IN177, and IN263) were removed from the test for destructive examinations. They were selected

because of their relatively long exposure time (~5 years for IN175 and IN177, and ~4 years for IN263) and materials conditions (Alloy 690 SA+31%CF, Alloy 690 TT+21%CF, and model binary alloy Ni-30Cr SA+20%CF, respectively), which have never been examined destructively before. The removal of these specimens allowed the six specimens (IN024, IN027, IN039, IN059, IN060, and IN180) previously tested in LWRS2 to be added to LWRS1. This activity was completed in May 2024 and the test has restarted in early June 2024.

As of the writing of this report, SEM surface examinations have been completed on all four removed specimens. Obvious cracks were only found on the gauge surface (Figure 15) and in the cross-section (Figure 16) of the initiated specimen IN173. Higher resolution characterizations of GB characteristics in the cross-section of all specimens have been halted by unexpected instrument maintenance and will be resumed once the SEM is back in operation.
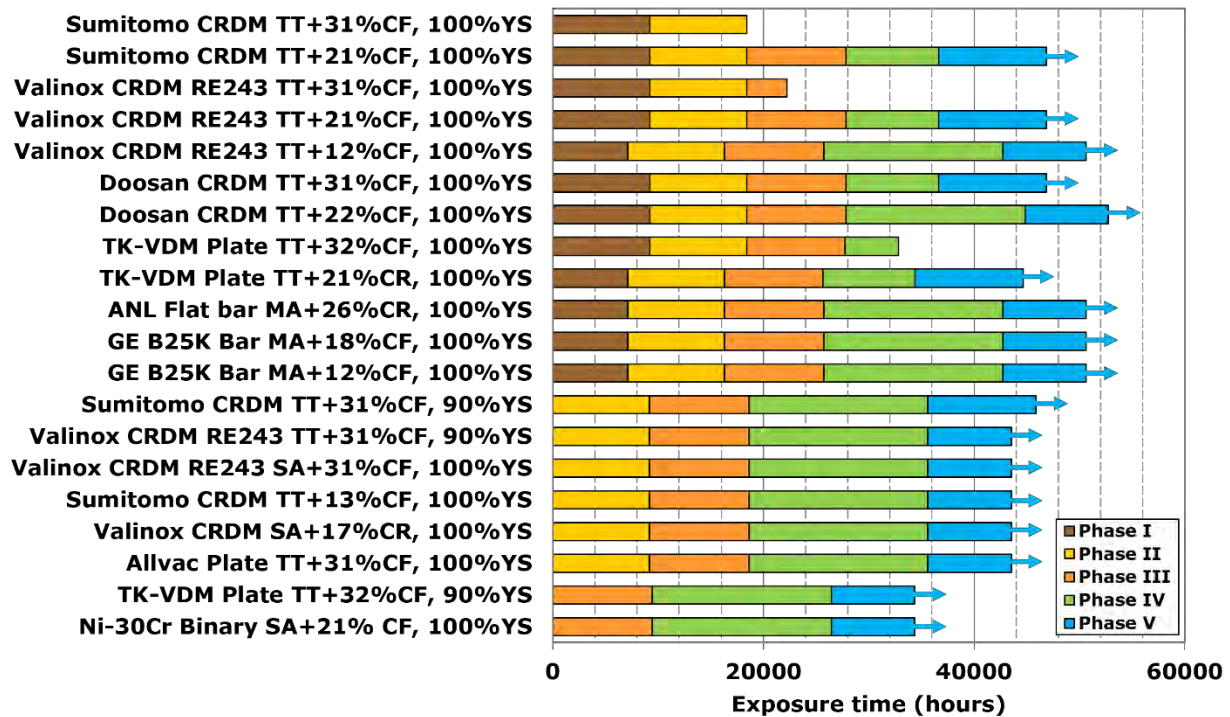
Figure 12. Up-to-date exposure time of the CW Alloy 690 materials evaluated in the long-term SCC initiation testing under LWRS. The arrows suggest that the test is ongoing as of June 2024 for the specified material and cold work conditions.

16

Table 6. Summary of material condition and SCC initiation testing status of all the tested Alloy 690 specimens as of June 2024.

Specimen	Material	Material Condition	Surface Condition	Applied Stress† (MPa)	Exposure time per phase (h)				
					I	II	III	IV	V*
IN024	Sumitomo CRDM	TT + 21% CF	1 μm	584	9220	9180	9440	8780	10261
IN025■	Sumitomo CRDM	TT + 21% CF	Ground	590	9220	9180	/	/	/
IN026■	Sumitomo CRDM	TT + 21% CF	Ground	590	9220	/	/	/	/
IN027	Valinox CRDM	TT + 21% CF	1 μm	523	9220	9180	9440	8780	10261
IN028■	Valinox CRDM	TT + 21% CF	Ground	525	9220	9180	/	/	/
IN029■	Valinox CRDM	TT + 21% CF	Ground	525	9220	/	/	/	/
IN030	Doosan CRDM	TT + 21.6% CF	1 μm	536	9220	9180	9440	17000	7907
IN031■	Doosan CRDM	TT + 21.6% CF	Ground	555	9220	9180	/	/	/
IN032■	Doosan CRDM	TT + 21.6% CF	Ground	555	9220	/	/	/	/
IN033■	Sumitomo CRDM	TT + 31% CF	1 μm	710	9220	/	/	/	/
IN034■	Sumitomo CRDM	TT + 31 % CF	Ground	710	9220	/	/	/	/
IN035■	Sumitomo CRDM	TT + 31% CF	Ground	710	9220	9180	/	/	/
IN036■	Valinox CRDM	TT + 31% CF	1 μm	720	9220	9180	3845	/	/
IN037■	Valinox CRDM	TT + 31% CF	Ground	720	9220	9180	/	/	/
IN038■	Valinox CRDM	TT + 31% CF	Ground	720	9220	/	/	/	/
IN039	Doosan CRDM	TT + 31% CF	1 μm	662	9220	9180	9440	8780	10261
IN040■	Doosan CRDM	TT + 31% CF	Ground	685	9220	9180	/	/	/
IN041■	Doosan CRDM	TT + 31% CF	Ground	685	9220	/	/	/	/
IN042■	TK-VDM Plate	TT + 31.9% CF	1 μm	676	9220	9180	9332	5066	/
IN043■	TK-VDM Plate	TT + 31.9% CF	Ground	676	9220	9180	/	/	/
IN044■	TK-VDM Plate	TT + 31.9% CF	Ground	676	9220	/	/	/	/
IN053	ANL Flat Bar	MA + 26% CR	1 μm	775	7110	9180	9440	17000	7907
IN054	ANL Flat Bar	MA + 26% CR	1 μm	769	7110	9180	9440	17000	7907
IN055■	ANL Flat Bar	MA + 26% CR	Ground	775	7110	/	/	/	/
IN056	GE B25K Bar	MA + 18.3% CF	1 μm	550	7110	9180	9440	17000	7907
IN057	GE B25K Bar	MA + 18.3% CF	1 μm	550	7110	9180	9440	17000	7907
IN058■	GE B25K Bar	MA + 18.3% CF	Ground	550	7110	/	/	/	/
IN059	TK-VDM Plate	TT + 21% CR	1 μm	653	7110	9180	9332	17000	10261
IN060	TK-VDM Plate	TT + 21% CR	1 μm	639	7110	9180	9440	17000	10261
IN061■	TK-VDM Plate	TT + 21% CR	Ground	675	7110	/	/	/	/
IN062	GE B25K Bar	MA + 12.4% CF	1 μm	510	7110	9180	9440	17000	7907
IN063	GE B25K Bar	MA + 12.4% CF	1 μm	510	7110	9180	9440	17000	7907

ID	Material	Treatment	Finish	Applied stress†					
IN064■	GE B25K Bar	MA + 12.4% CF	Ground	510	7110	/	/	/	/
IN065	Valinox CRDM	TT + 11.7% CF	1 μm	365	7110	/	/	/	/
IN066	Valinox CRDM	TT + 11.7% CF	1 μm	379	7110	9180	9440	17000	7907
IN067■	Valinox CRDM	TT + 11.7% CF	Ground	365	7110	/	/	/	/
IN172	Allvac Plate	TT + 31%CF	1 μm	623	/	9180	9440	17000	7907
IN173■	Allvac Plate	TT + 31%CF	1 μm	623	/	9180	9440	17000	7907
IN174	Valinox CRDM	SA + 31%CR	1 μm	632	/	9180	9440	17000	7907
IN175■	Valinox CRDM	SA + 31%CR	1 μm	632	/	9180	9440	17000	7907
IN176	Sumitomo CRDM	TT + 21%CF	1 μm	575	/	9180	9440	17000	7907
IN177■	Valinox CRDM	TT + 21.9%CF	1 μm	510	/	9180	9440	17000	7907
IN178	Valinox CRDM	TT + 21.9%CF	1 μm	465	/	9180	9440	17000	7907
IN179■	Sumitomo CRDM	TT + 30.6%CF	1 μm	588 (90%YS)	/	9180	9440	17000	/
IN180	Sumitomo CRDM	TT + 30.6%CF	1 μm	575 (90%YS)	/	9180	9440	17000	10261
IN181	Valinox CRDM	TT + 31%CF	1 μm	580 (90%YS)	/	9180	9440	17000	7907
IN182	Valinox CRDM	TT + 31%CF	1 μm	575 (90%YS)	/	9180	9440	17000	7907
IN183	Sumitomo CRDM	TT + 12.7%CF	1 μm	405	/	9180	9440	17000	7907
IN184	Valinox CRDM	SA + 17%CR	1 μm	335	/	9180	9440	17000	7907
IN263■	Ni-30Cr	SA + 21%CF	1 μm	488	/	/	9440	17000	7907
IN264	Ni-30Cr	SA + 21%CF	1 μm	502	/	/	9440	17000	7907
IN265	Ni-30Cr	SA + 21%CF	1 μm	488	/	/	9440	17000	7907
IN266	TK-VDM CRDM	TT + 32%CF	1 μm	603 (90%YS)	/	/	9440	17000	7907
IN267■	TK-VDM CRDM	TT + 32%CF	1 μm	668	/	/	9440	17000	3850
IN268	TK-VDM CRDM	TT + 32%CF	1 μm	603 (90%YS)	/	/	9440	17000	7907
IN269	Valinox RE243	SA + 31%CR	1 μm	655	/	/	9440	17000	7907
IN270	Valinox RE243	SA + 31%CR	1 μm	655	/	/	9440	17000	7907
IN271	Doosan CRDM	TT + 21%CF	1 μm	530	/	/	9440	17000	7907
IN272	Sumitomo CRDM	TT + 21%CF	1 μm	546	/	/	9440	17000	7907
IN294	Valinox CRDM	TT + 21.9%CF	1 μm	510	/	/	/	17000	7907
IN295	Valinox CRDM	TT + 21.9%CF	1 μm	505	/	/	/	17000	7907
IN296	Valinox CRDM	TT + 11.7%CF	1 μm	364	/	/	/	17000	7907
IN297	Sumitomo CRDM	TT + 12.7%CF	1 μm	380	/	/	/	17000	7907

† The applied stress is the yield stress of the specimens at the tested temperature (360°C) unless otherwise specified.

■ Specimens removed for cross-section examination. *Ongoing test as of June 2024.
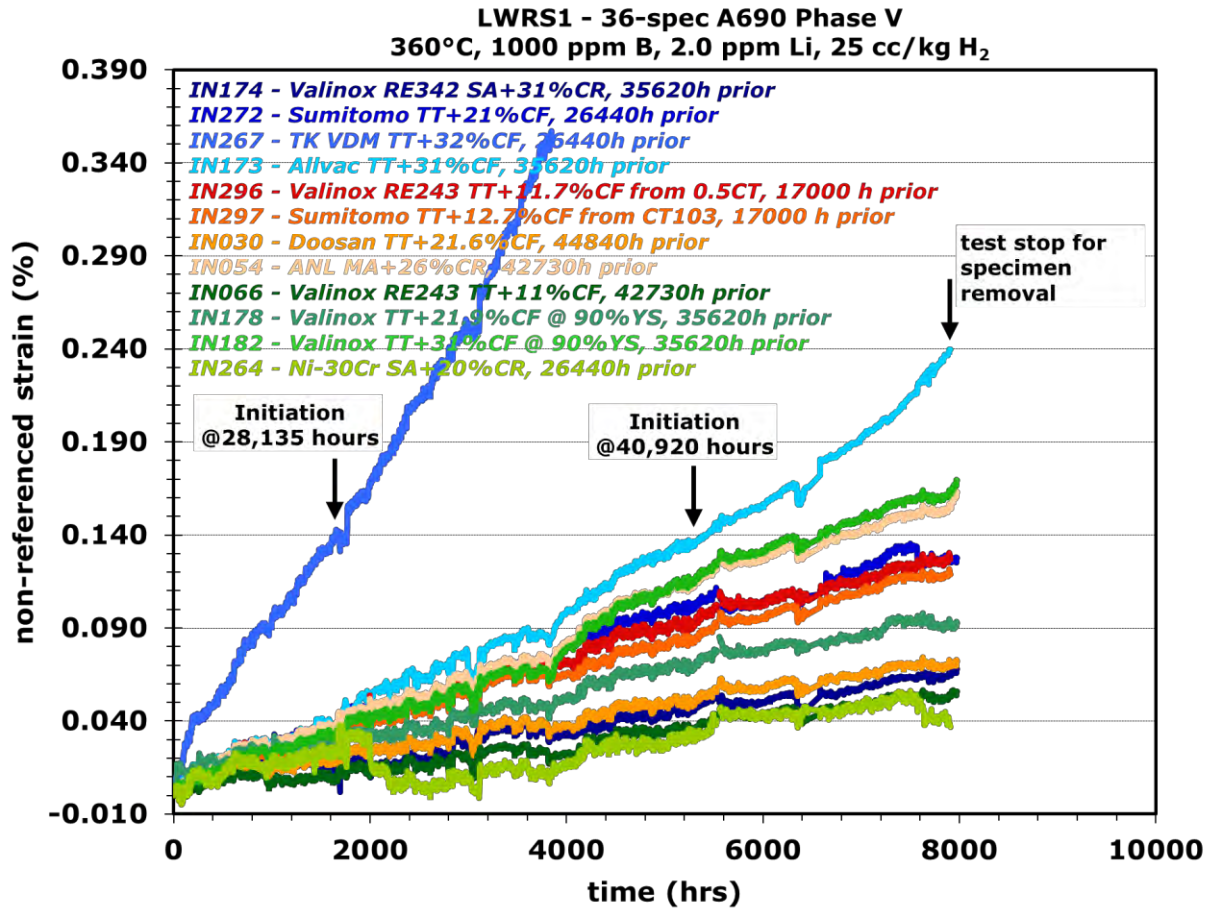
Figure 13. Overall non-referenced DCPD strain response during the Phase V exposure for all the specimens monitored in the LWRS1 SCC initiation test system in 360 °C PWR primary water by the time the test was stopped in April 2024. Specimens were all tested at materials yield stress unless otherwise specified.
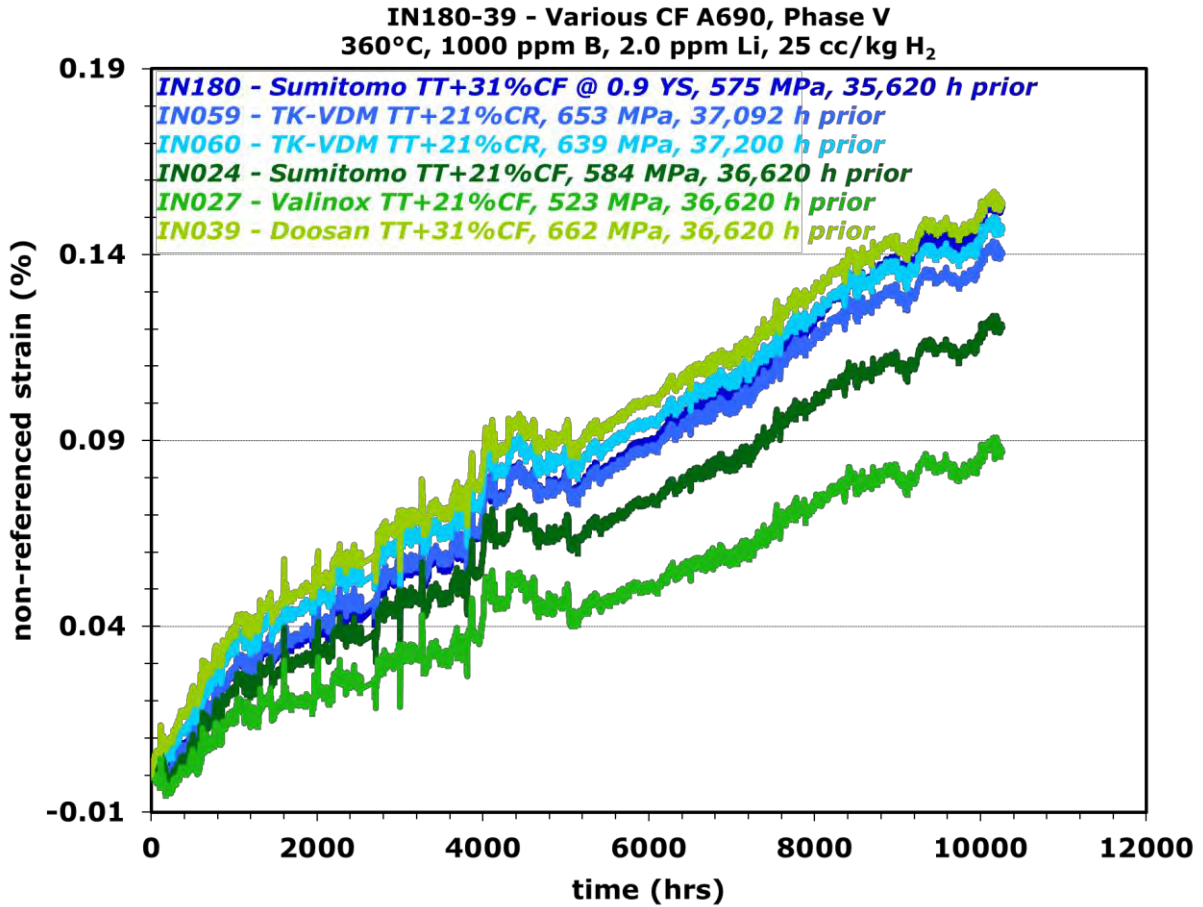
Figure 14. Overall non-referenced DCPD strain response during the Phase V exposure for all the specimens monitored in the LWRS2 (6-specimen) SCC initiation test system in 360 °C PWR primary water by the time the test was stopped in April 2024. Specimens were all tested at materials yield stress unless otherwise specified.
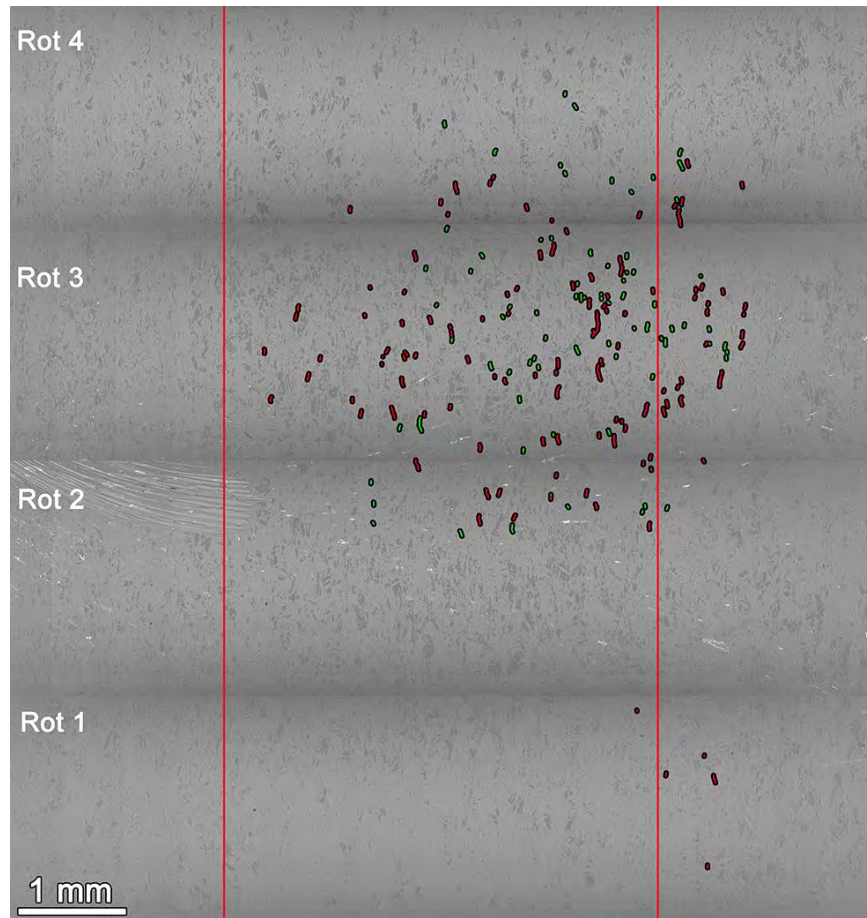
Figure 15. SEM-BSE montage image of the Allvac TT+31%CF specimen IN173 removed after 43,527 hours of exposure in 360°C simulated PWR primary water upon DCPD detection of crack initiation. The gauge section of the specimen is between the two red lines marked in the image. Obvious cracks and possible cracks are highlighted in red and green, respectively.
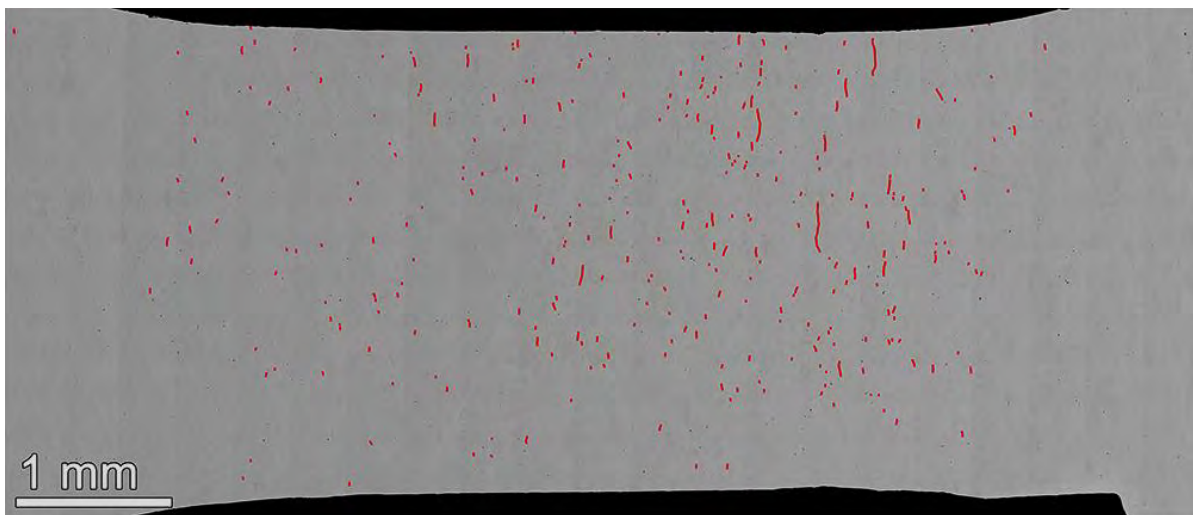
Figure 16. SEM-BSE montage image of the cross-section of the Allvac TT+31%CF specimen IN173. Continuous and semi-continuous IG damage are highlighted in red.

2.3.2 Synchrotron X-Ray Diffraction Measurements on Selected Specimens

2.3.2.1 Materials and Specimens

Two commercial Alloy 690 heats, Doosan 133454 and Valinox RE243, and one Ni-30Cr binary model alloy were chosen for this study. The composition of the two commercial Alloy 690 heats is listed in Table 1, where the Doosan 133454 has the lowest Fe content (8.9 wt%) while the Valinox RE243 has the highest (10.4 wt%) among all tested commercial heats. Fe content in the material is believed to play a key role in the kinetics of ordering reactions in Ni-base alloys, where the increase of Fe retards the kinetics of ordering but does not impede its formation [22-24]. As a result, Doosan 133454 was chosen for this study because of its lowest Fe content among all heats (Table 1). This heat has been tested in moderately and highly cold worked conditions, and both conditions are included in this study. Valinox RE243 contains the highest Fe content, but hardness measurements performed on this heat revealed obvious hardening at high cold work levels after aging in 360°C PWR primary water [25]. In addition, Valinox RE243 has the most variations in thermal-mechanical histories and cold work levels among all tested heats. Therefore, it was decided to also investigate this heat using SXRD to not only measure long range ordering (LRO), but also other changes that could be induced by long-term aging, such as precipitate coarsening and strain evolution. Finally, a SA+31%CF cold worked Ni-30Cr binary model alloy is included to serve as a reference since the model alloy is known to be more prone to LRO formation than commercial Alloy 690 alloy [26]. Table 7 lists all the heats and their material conditions being investigated in the SXRD study. Almost all material conditions listed in the table contain specimens with different exposure times, allowing the effect of time evolution to be studied on the material's aging behavior.

To preserve the highly valuable gauge section in the initiation specimens and to allow the specimens to be reusable, a wedge-shaped sample was extracted from one button end of each selected specimen for SXRD analysis (Figure 17). No obvious difference in hardening degree was observed during previous hardness measurements on the high-stress gauge region vs. low-stress reference region in each specimen [25], suggesting the sample cut from the button end is valid to use. One wedge-shaped sample was prepared from each specimen listed in Table 7. It was extracted using a low-speed precision saw while the specimen was secured in a fixture specifically designed for this application, allowing a thin slice to be cut off at an angle to the end plane of the specimen. The thickness of the wedge sample is usually around 0.5 mm. The extracted wedge sample was then manually polished on both sides to a 1 μm surface finish.
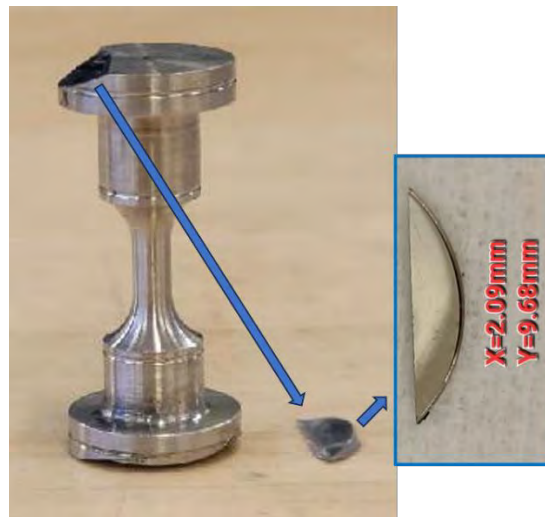
Figure 17. Photos showing the wedge samples cut off from initiation specimens for SXRD analysis.

Table 7.   Summary of material condition and exposure time of the samples selected for SXRD analysis and their current measurement status.

SAMPLE ID	Material condition	Exposure time (year)	SXRD completed?	LRO?
IN039	Doosan TT+31%CF	5.3	Y	N
IN040	Doosan TT+31%CF	2.1	Y	N
IN041	Doosan TT+31%CF	1.1	Y	N
IN030	Doosan TT+21%CF	6.0	N	
IN271	Doosan TT+21%CF	3.9	Y	N
IN031	Doosan TT+21%CF	2.1	Y	N
IN032	Doosan TT+21%CF	1.1	Y	N
D-TT21-AR	Doosan TT+21%CF	0	N	
IN181	Valinox TT+31%CF	5.0	N	
IN037	Valinox TT+31%CF	2.5	Y	N
IN036	Valinox TT+31%CF	2.1	Y	N
IN038	Valinox TT+31%CF	1.1	N	
V-TT31-AR	Valinox TT+31%CF	0	N	
IN027	Valinox TT+21%CF	5.3	Y	N
IN294	Valinox TT+21%CF	2.8	N	
IN028	Valinox TT+21%CF	2.1	N	
IN029	Valinox TT+21%CF	1.1	N	
V-TT21-AR	Valinox TT+21%CF	0	N	
IN065	Valinox TT+12%CF	5.8	N	
IN296	Valinox TT+12%CF	2.8	Y	N
IN067	Valinox TT+12%CF	0.8	N	
V-TT12-AR	Valinox TT+12%CF	0	N	
IN175	Valinox SA+31%CR	5.0	N	
IN269	Valinox SA+31%CR	3.9	N	
V-SA31-AR	Valinox SA+31%CF	0	N	
IN184	Valinox SA+17%CR	3.9	N	
IN263	Ni-30Cr SA+20%CF	3.9	N	
IN265	Ni-30Cr SA+20%CF	3.9	Y	Y

2.3.2.2   *Experimental Method*

SXRD measurements were performed at the National Synchrotron Light Source-II (NSLS-II) using the high-energy X-rays available at the Pair Distribution Function beamline. All measurements were performed in transmission mode with an amorphous silicon-based flat panel detector (Perken-Elmer) mounted orthogonal to and centered on the beam path. The sample-to-detector distances and tilts of the detector relative to the beam were refined using a LaB6 powder standard (NIST standard reference material 660c). The wavelength of the incident X-rays was 0.1665 Å (74.46 keV). The sample-to-detector distance was calculated to be 1052.65 mm. 600 XRD patterns were collected with detector exposures of 0.1s. Specimens were vertically scanned to improve averaging and to sample a large fraction of the individual specimens. All raw two-dimensional patterns were background corrected by subtracting a dark current image, and the air and Kapton scattering background within IgorPro (Wavemetrics). Noticeable artifact regions of the detector (e.g., beam stop, dead pixels) were masked. The corrected and masked two-dimensional detector images were then radially integrated to obtain one-dimensional powder diffraction patterns.

The background-subtracted XRD patterns were Rietveld refined within the TOPAS software package. The peak profiles were modeled by a Thompson-Cox-Hasting peak function. The instrument contribution

to the broadening of the measured profiles was quantified by fitting the LaB$_6$ NIST powder standard, with a known coherent grain size and negligible microstrain contribution. The Gaussian and Lorentzian-based broadening parameters were subsequently fixed during the analysis of the alloys under investigation to quantify the microstructure (XRD microstrain, phase quantification, and lattice parameters). The phase fraction and lattice parameter were allowed to vary for the minor crystal phases present. The Coherent grain sizes for the TiN and M$_{23}$C$_6$ precipitates were fixed to large values. The microstrain components for the minor phases (M$_{23}$C$_6$ and TiN) were not included in the refinements. Therefore, the refined coherent grain size parameters have lower limits. A polynomial background (Chebyshev Polynomial) was included in the refinements to capture the diffuse background.

2.3.2.3   Results

To date, eleven specimens were measured during a single session. These specimens are noted in Table 7. Figure 18 shows the 2D XRD patterns for all three representative specimens. All 690 specimens show mostly uniform Debye rings, consistent with a powder-like microstructure. Very minor diffraction anisotropy was observable in these specimens. Even with the minor apparent anisotropy/preferred orientation, the XRD patterns and data are sufficient to analyze with quantitative XRD Rietveld methods (minor texture was utilized when needed, and has a negligible effect on the weight fractions, and improves the fit quality).
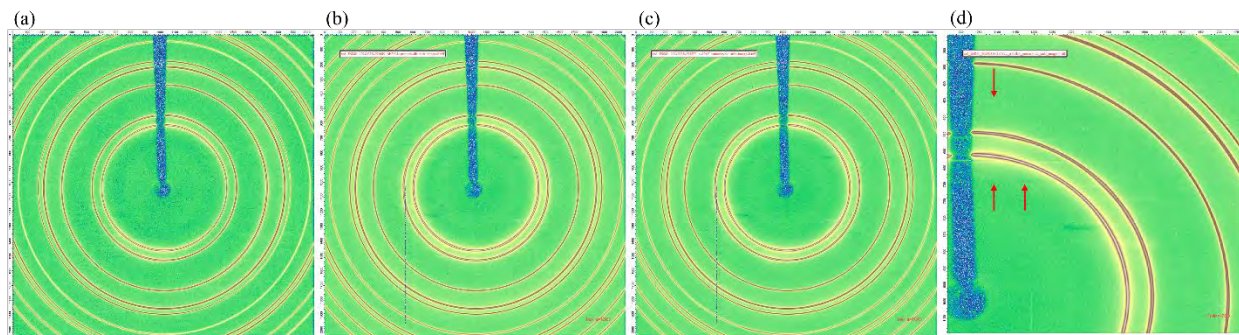
Figure 18. 2D XRD patterns for Doosan TT+31%CF specimens (a) IN039, (b) IN040, and (c) IN041 exposed for 5.3, 2.1, and 1.1 years in 360°C simulated PWR primary water. Panel (d) shows a magnified view of the region with "spotty" peaks for the MX and M$_{23}$C$_6$ particles.

Figure 19 shows the background corrected, integrated XRD patterns for the eleven specimens, grouped by heat and cold forging level. The intensity is plotted on a logarithmic scale to highlight microstructural features of interest. Minor reflections from M$_{23}$C$_6$ and MX (M: metal, X: nitride/oxide) are evident in all Alloy 690 specimens (highlighted by red and black arrows in Figure 19a). These M$_{23}$C$_6$ and MX precipitates appear to be quite large, with evidence of coarse grain structures apparent in the 2D XRD patterns (spotty Debye rings as shown in Figure 18d). No strong LRO peaks are observable above background for any of the Alloy 690 specimens except indications of short range ordering, while the Ni-30Cr SA+31%CR binary alloy showed subtle peaks consistent with the Immm Ni$_2$Cr phase as marked by the blue arrows in Figure 19d. The quantified lattice parameters agree with bulk FCC Cr$_{23}$C$_6$ for the M$_{23}$C$_6$ phase and agree with TiN for the MX phase, which are consistent with pre-test microstructure characterization results. The fractions from the quantitative XRD appear to be similar in magnitude (within error) and self-consistent with previous Alloy 690 quantifications performed on NRC-EPRI initiation specimens.
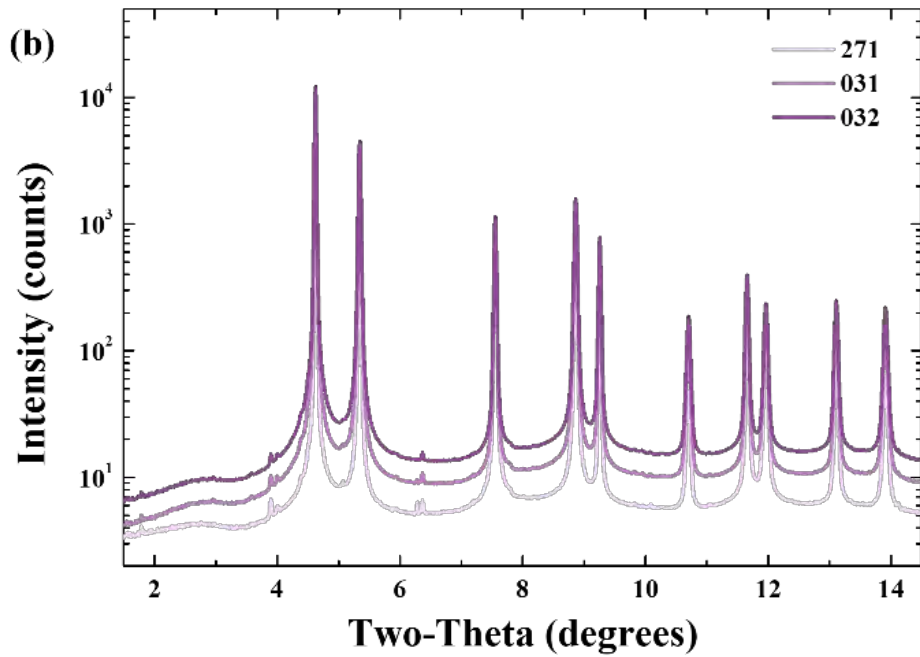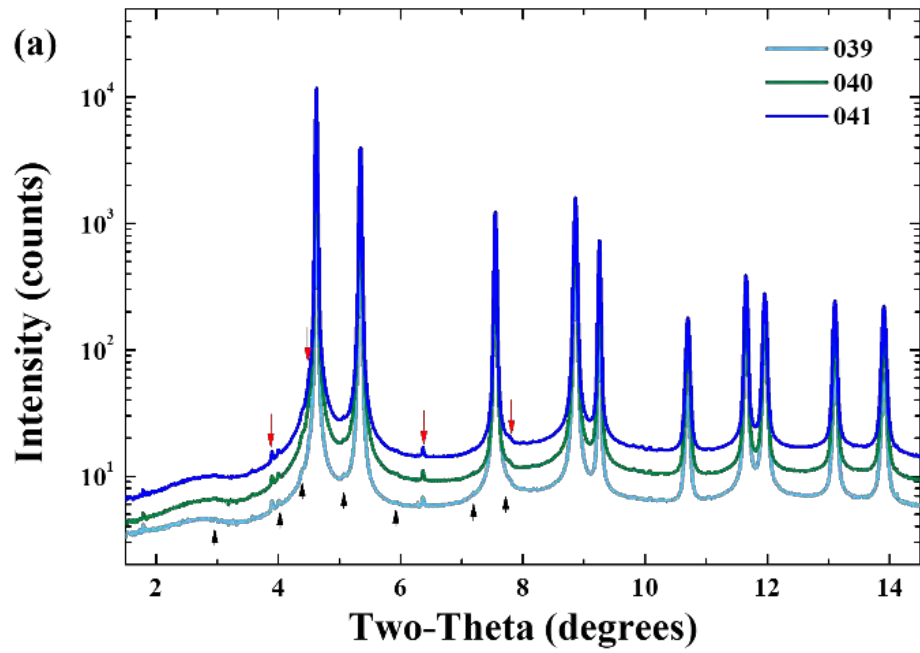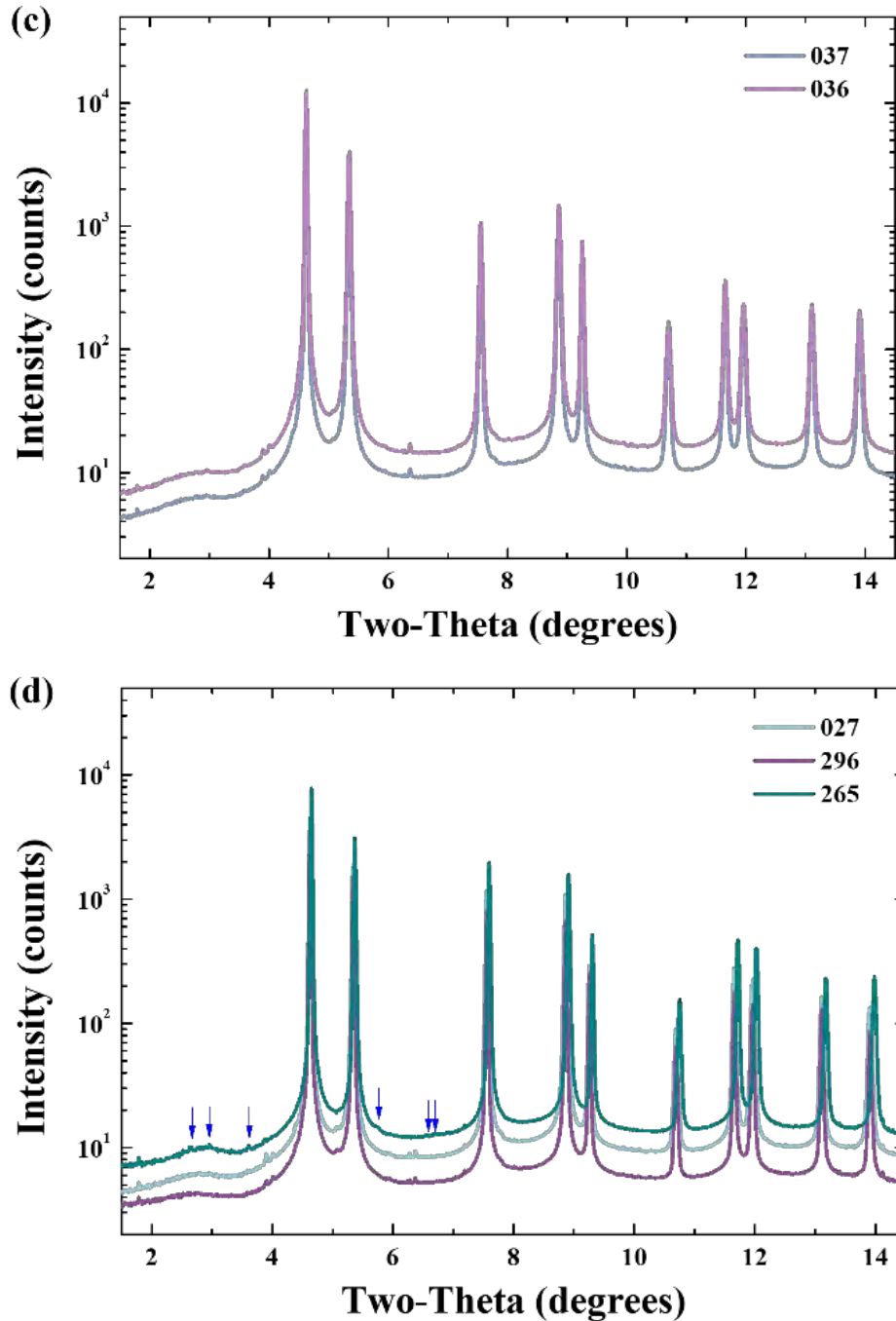
Figure 19. Reduced XRD patterns for all measured specimens previously exposed in 360°C simulated PWR primary water: (a) Doosan TT+31%CF specimens exposed for 5.3 (IN039), 2.1 (IN040), and 1.1 (IN041) years, (b) Doosan TT+21%CF specimens exposed for 3.9 (IN271), 2.1 (IN031), and 1.1 (IN032) years, (c) Valinox TT+31%CF specimens exposure for 2.5 (IN037) and 2.1 (IN036) years, (d) Valinox TT+21% specimens IN027 exposed for 5.3 years, Valinox TT+12%CF IN296 exposed for 2.8 years, and Ni-30Cr SA+20%CF specimen IN265 exposed for 3.9 years. Black and red arrows indicate the minor $Cr_{23}C_6$ and TiN phases. Note the 265 specimen has subtle features close to the peaks expected for Immm Ni_2Cr phase, as indicated by blue arrows.

Lattice parameters were also measured for the eleven specimens and their time evolution per heat and material condition is plotted in Figure 20. An interesting phenomenon is observed in the Doosan TT+21%CF and Doosan TT+31%CF data sets: instead of a monotonous trend, both sets showed a subtle peak in lattice constant after ~2 years of exposure. While this may indicate microstructural evolution in Alloy 690 is non-linear with time, further investigation is needed to evaluate whether this trend applies to other heats and material conditions, and to clarify the root cause of this observation. As listed in Table 7, additional specimens including a few in as-received condition for different material + cold work combinations have been added to the test matrix, and all specimens will be measured in the same next session scheduled in the summer of 2024 including those that have already been measured to avoid potential error introduced by beamline conditions. Preliminary quantification data on Lorentzian and Gaussian broadening parameters, microstructural parameters reflecting two-dimensional defects evolution, were also obtained but no obvious trend could be determined yet. It is expected a better understanding will be obtained after the next session of measurements on all specimens with more thorough post-test analyses.
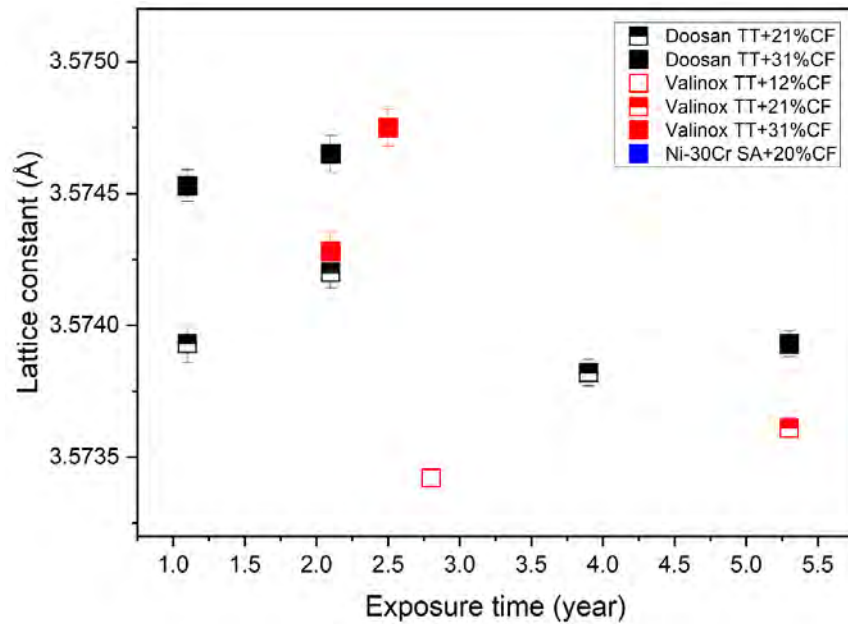
Figure 20. Lattice constants measured in all specimens grouped by heat and material condition and as a function of exposure time. The Ni-30Cr SA+20%CF specimen has a very different lattice constant so is not shown in this figure to better visualize the difference among the other specimens.

3. Creep Testing of Cold Worked Alloy 690

3.1 Chapter Overview

The long-term SCC initiation testing of Alloy 690 in PWR primary water revealed that, different from the classical understanding of SCC where the crack grows from the surface exposed to high-temperature water by rupturing protective oxide layer, the crack initiation occurred so far in cold-worked Alloy 690 was dominated by creep cavity formation and coalescence throughout the specimen, leading to the formation of IG creep cracks both on the surface and inside the specimen. To date, such macroscopic crack initiation has only been observed in TT+highly CW Alloy 690 featuring nanometer-sized carbides at GBs loaded at high stress levels, which usually occurred between 2 and 4 years of exposure depending on materials microstructure and applied stress. However, evidence of increasing GB cavities was also confirmed in Alloy 690TT materials with lower cold work levels, but only after longer exposure times and to a much lesser extent [21]. To better understand the mechanism of creep-induced cavity formation in Alloy 690 and to accelerate data collection for predicting the long-term behavior of Alloy 690 in service, a new testing effort started in FY 2023 to evaluate the effect of cold work method, cold work level, temperature, environment, and exposure time on creep induced cavity evolution and crack initiation in thermally treated Alloy 690. Quantitative data on cavity distribution will be collected as a function of these variables. In FY 2024, we completed 1-year exposure at all temperatures and the testing and characterization results will be summarized in this chapter.

3.2 Experimental

3.2.1 Test Objective, Scope, and Materials

The creep test in air complements the ongoing SCC initiation testing of CW Alloy 690 in 360°C PWR primary water. It is a cost-effective way to include more parameters that are needed for predicting creep-induced cavity evolution in Alloy 690 in service-relevant conditions, which include:

- Temperature: to determine the thermal activation energy for crack initiation.

- Exposure media: to evaluate whether creep cavity formation is accelerated in water.

- Exposure time: to establish the time dependence of creep cavity evolution.

- Cold work method: to investigate the effect of cold work methods on cavity evolution.

Two Alloy 690 CRDM heats, Valinox WP142 and Valinox RE243, in TT condition were chosen for this study because they exhibit a semi-continuous distribution of nanometer-sized IG carbides that has shown to be the most susceptible to GB cavity formation [9]. The basic information of these two heats is provided in Table 8. The test scope for these two materials is detailed in Table 9. The Valinox WP142 Alloy 690TT heat was cold forged into three different levels. Three specimens were prepared for each cold forge level at each temperature and are planned to be removed for detailed destructive analysis after reaching 1, 2, and 3 years of exposure, respectively. The Valinox RE243 Alloy 690TT heat was cold tensile strained (CTS) to 29% elongation beyond the yield point. Due to restrictions in material availability and test system space, only two specimens were prepared at each temperature, with planned exposure of 1 and 2 years. An identical set of specimens was prepared for a companion crack initiation test in simulated PWR primary water at 360°C at Ni/NiO stability line for the same planned durations of exposure. For both heats, one specimen is planned to be removed after each year of exposure, cross-sectioned, and detailed examination and quantification will be performed on them to document GB cavity evolution.

Before the test started, all materials were documented in SEM for their as-received microstructure, focusing on the damage induced by cold work at HAGBs. Figure 21 shows the representative morphology at HAGBs in the Valinox WP142 Alloy 690TT materials cold forged to 11, 21, and 31% reduction in

thickness, respectively. Similar to what was observed for the CF Valinox RE243 (Figure 7), cold forging-induced damage manifests itself in the forms of cracked carbides and voids between carbides, of which the size and density increased with increasing cold forge level.

Table 8. Composition, heat treatment, and as-received mechanical properties for Alloy 690 heats chosen for the air creep testing.

Source/Manufacturer and Heat #	Dimension (mm)	Composition, wt%	Heat Treatments	Room-temp YS (MPa)
Valinox/ Valinox WP142 Tube 2541	116 OD x 30 wall	Ni-29.0Cr-10.5Fe-0.02C-0.3Mn-0.35Si-0.47Ti-0.01Nb-0.001S-0.003P	1096°C/~1 min, WQ + 716-722°C/10.2 h, AC	269
Valinox/ Valinox RE243 Tube 2360	112 OD x 34 wall	Ni-28.9Cr-10.4Fe-0.02C-0.3Mn-0.35Si-0.14Al-0.23Ti-0.024N-0.008P-0.0005S	1122°C/~1 min, WQ + 716-725°C/10.5 h, AC	255
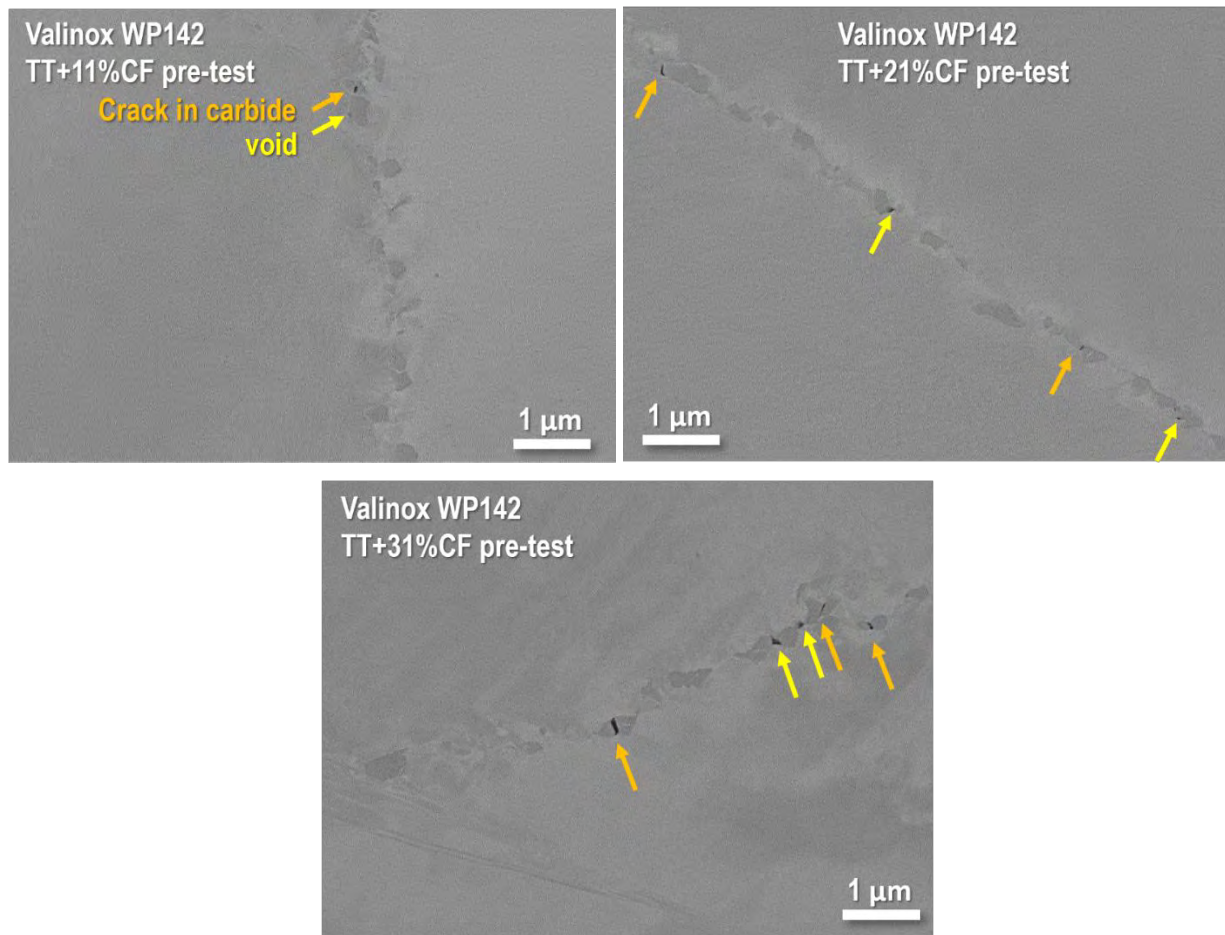
Figure 21. Cold forging-induced defects at GBs in the 11%, 21%, and 31% CF Valinox WP142 Alloy 690TT materials.

Table 9.   Air creep test scope for CW Alloy 690.

Alloy 690 Heat #	CW condition	Test temp (°C)	Planned test duration
Valinox WP142	12, 21, and 31% CF	Creep test at 330, 360, 400 Primary water test at 360	1, 2, and 3 years
Valinox RE243	29% CTS	Creep test at 330, 360, 400 Primary water test at 360	1 and 2 years

3.2.2   Test Method

Unlike common creep tests where a single specimen is evaluated with creep rates measured by displacement transducers, this study evaluates multiple specimens in each test system to maximize testing capacity. The specimen geometry and dimensions for this test are presented in Figure 22, which is based on our cylindrical SCC initiation specimens but with threaded top and button ends. A loading train was designed with tensile specimens linked by couplers through these threaded ends. The creep rates are measured in-situ using the DCPD technique described in Section 2.2.2. Before the actual test, a shakedown test was performed at 400°C under step loading at PNNL, and the resolution was confirmed to be sufficient for the intended creep rate measurements. The setup of this shakedown test is provided in Figure 23.
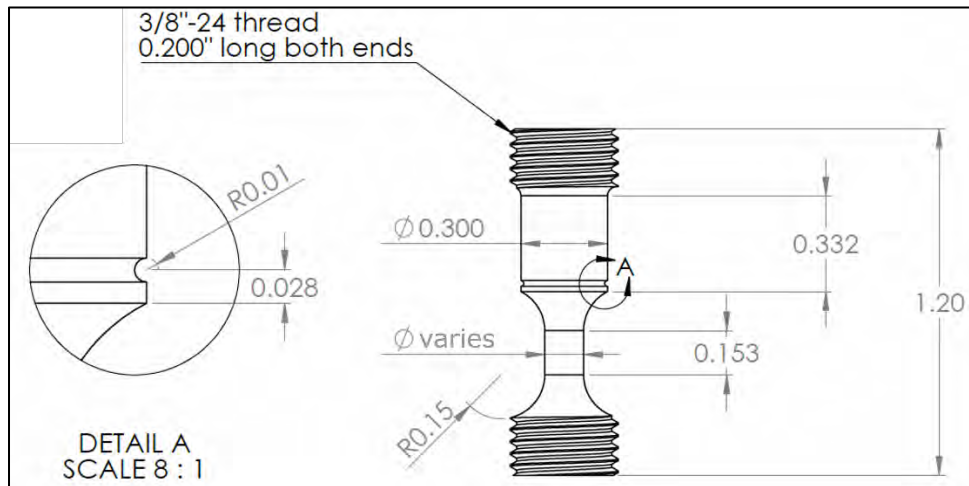
Figure 22. Threaded initiation specimen design for the creep test in air. All dimensions are in inches.
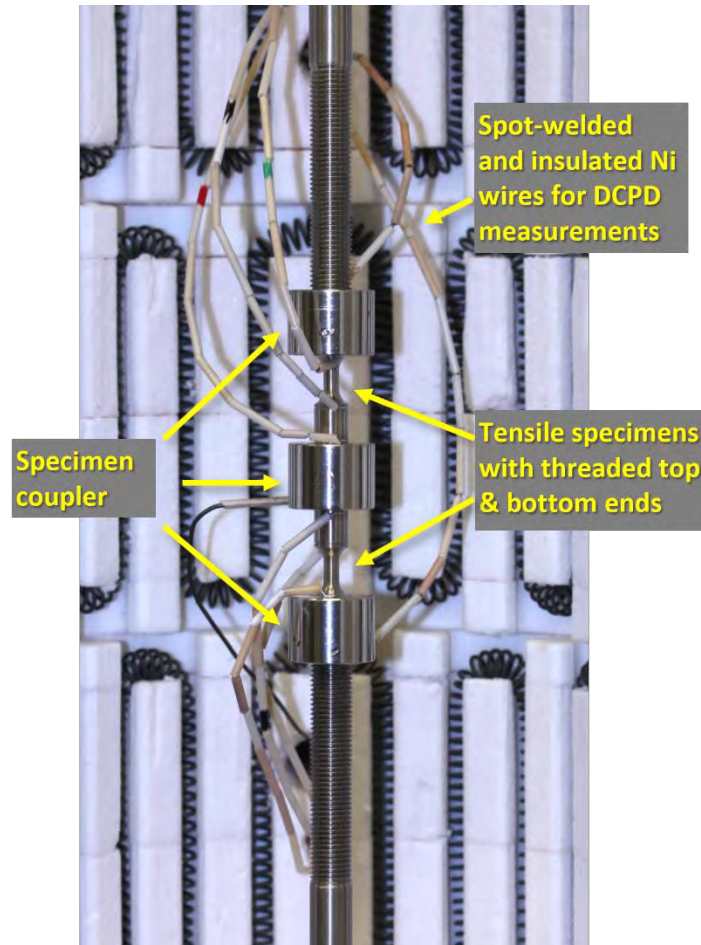
Figure 23. Setup of the PNNL threaded tensile specimen DCPD shakedown test.

Before the start of the tests, all specimens were polished to a fine 1 µm finish on their gauge section. This is the same surface finish applied to most Alloy 690 SCC initiation specimens in the high-temperature water test. It facilitates examination of precursor damage and cracks, and creates a surface with consistent microstructure and mechanical properties similar to the bulk material. In addition, as shown in Figure 24, plasma focused ion beam (PFIB) milling was employed to create narrow trenches in the gauge section of each specimen to serve as fiducial marks for post-test GB sliding assessment. The total length of the trenches in each specimen is ~1.5–2 mm and intersects 20 HAGB boundaries on average. The width of the trenches is ~5 µm and the depth is ~1 µm.

The actual creep tests are performed at Lucideon M+P Lab (denoted as Lucideon thereafter), where three deadweight loading systems are used for the 330, 360, and 400°C tests, respectively. All creep tests are performed in air. Figure 25 shows one of the deadweight creep test systems at Lucideon and the load train configuration used for the actual creep tests. The 330°C and 360°C test systems have a 5:1 lever arm and the 400°C test system has a 20:1 lever arm. The load train is installed inside the furnace, where the temperatures were measured from three sections (top, middle, and bottom) of the furnace to make sure the heating is uniform and stable throughout the test. During each test phase, seven specimens are tested at material YS in a single load train in each test system. The tests at different temperatures all started with two specimens from the Valinox CRDM WP142 heat at each cold forge level and one specimen from the RE243 heat in the 29%CTS condition. After completion of the first year exposure, one specimen is removed from each condition, and a corresponding replacement specimen will be added to the load train for another continued exposure of two years, unless the test needs to be temporarily stopped to remove

initiated specimens before the target completion date. This will allow us to have one Valinox WP142 TT + 11, 21, and 31% CF specimen each exposed for 1, 2, and 3 years and one RE243 TT+29%CTS specimens each exposed for 1 and 2 years at each test temperature once the creep tests are completed. To allow easy tracking of all specimens, a six-character specimen ID format was determined for the creep test as such:

- The 1st character denotes the heat: W = WP142, R = RE243.

- The 2nd and 3rd characters denote the cold work level: 11 = 11%CF, 21 = 21%CF, 31 = 31%CF, 29 = 29%CTS.

- The 4th character denotes the test temperature: A = 330°C, B = 360°C, and C = 400°C.

- The last (i.e., 6th) character following a dash denotes the planned exposure time for the specimen: 1 = 1 year, 2 = 2 years, and 3 = 3 years.

For example, "W11A-1" means this is a WP142 TT+11%CF specimen planned to be tested at 330°C for one year. The same ID format will be used for all creep test specimens thereafter without further explanations.

Similar to the SCC initiation testing in simulated PWR primary water, the specimen load-up process is monitored in-situ by DCPD during the start and every restart of all creep tests. The weights used during loading range from 0.25 lbs to 20 lbs. Heavier weights were used during the early stage of the load up, while the lightest ones were used in the end to fine tune the applied stress and assess the degree of yielding in each specimen. An example of the specimen stress vs. strain curves during the initial load-up of the 360°C test is provided in Figure 26. It is noted that the RE243 TT+29%CTS specimen usually yielded faster than the other specimens during the load-up at all test temperatures. To achieve yielding in the other specimens, the RE243 TT+29%CTS specimens were allowed to be loaded further beyond the yield point, resulting in 4% and 9% plastic strain in the specimen in the 330 and 360°C tests, respectively. The RE243 TT+29%CTS specimen failed during the load-up in 400°C air. Therefore, this test was carried out without a RE243 TT+29%CTS specimen during the first year.
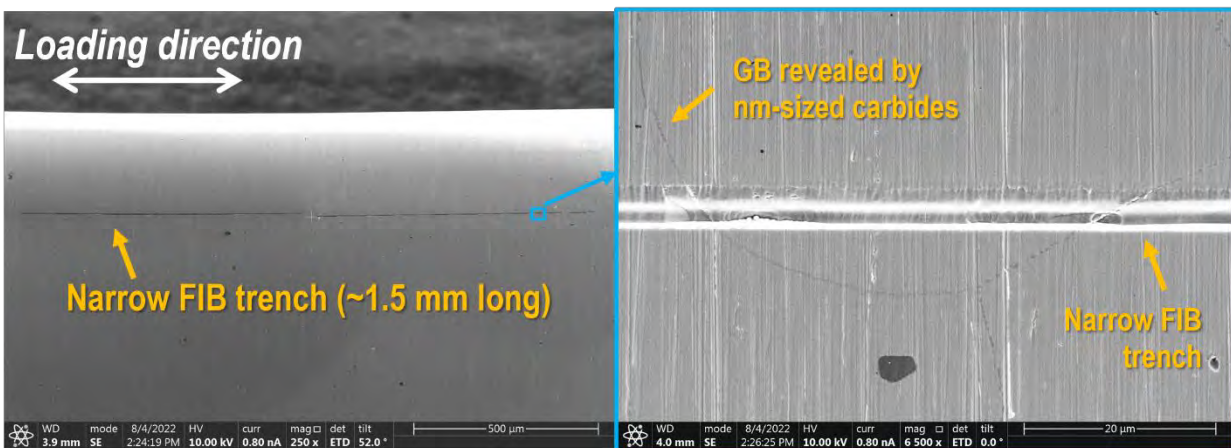
Figure 24. Example of the narrow FIB trench made in the gauge section of the creep specimens prior to the test to serve as a fiducial mark for post-test GB sliding measurement. The trench is around 1.5 – 2 mm long and less than 5 μm wide.
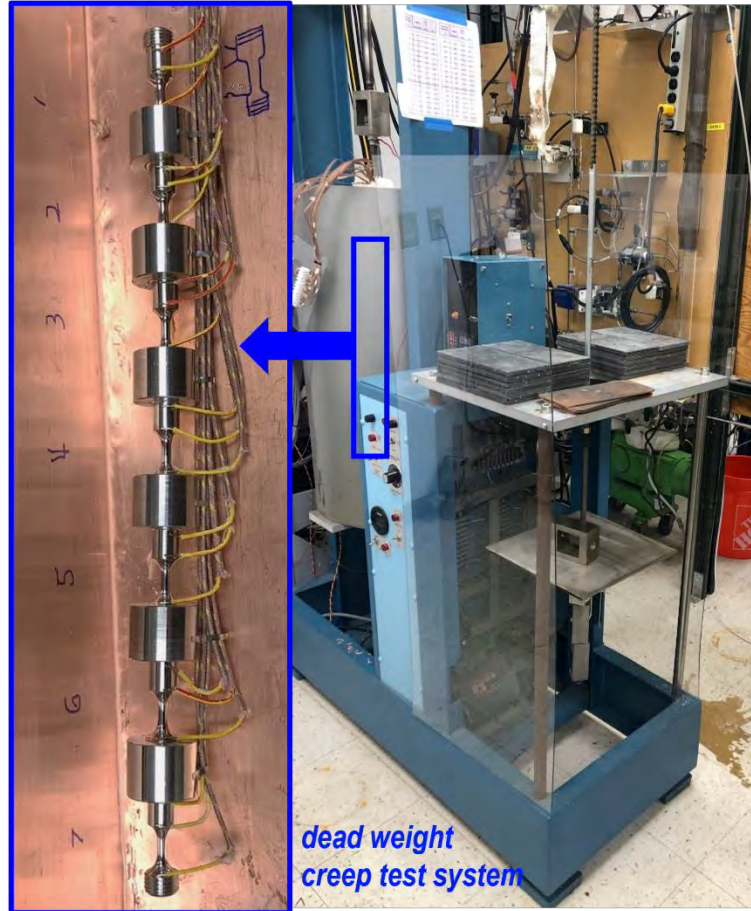
Figure 25. Deadweight creep test system at Lucideon M+P showing the furnace and the lever arm (partial view) with dead weights (right), and the load train inside the furnace containing seven specimens with instrumentation wires spot welded to each specimen for in-situ DCPD monitoring of creep rates and crack initiation (left).
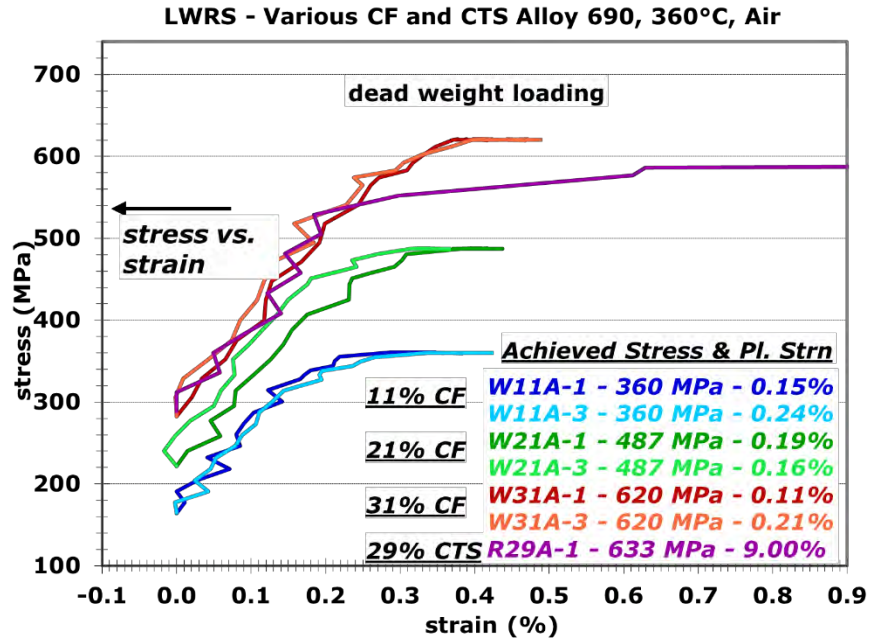
Figure 26. Example of stress versus strain plot during the initial loading of seven specimens in the 360°C creep test in air.

3.3   Results

3.3.1   Test Overview
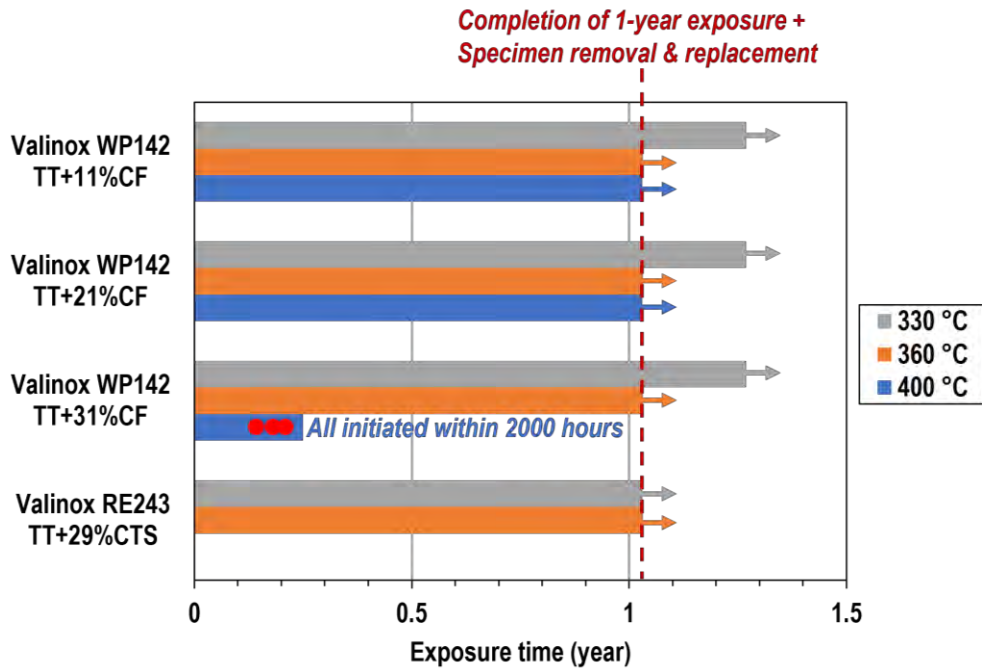
Figure 27. Test progress on specimens with the longest exposure at each temperature.

A status overview of the creep tests is provided in Figure 27. As of June 2024, the 1st-year exposure has been completed for all three temperatures. All specimens were removed from test systems for detailed surface examination using SEM, while the specimens scheduled for 1-year only exposure were replaced by new specimens that are planned to be exposed for 2 years in subsequent testing. Phase II exposure has already begun for the 330°C test, and is under preparation at Lucideon for the 360 and 400°C tests with a scheduled start in July 2024. It should be noted that all three Valinox WP142 TT+31%CF specimens tested at YS in 400°C air have all initiated within the first 2000 hours of exposure, which will be detailed in Section 3.3.4 later. In addition, as mentioned in Section 3.2.2, the Valinox RE243 TT+29%CTS specimen in the 400°C test failed during loading, so there was no CTS specimen evaluated for the first one-year test at 400°C. The details of all the specimens tested or being tested in the creep tests are summarized in Table 10. In the following sections, the creep behavior as documented by DCPD on these specimens will be given, along with highlights of the results obtained from SEM microscopy performed after the completion of 1-year exposure.

Table 10.   Specimen status of the creep test grouped by testing temperature as of June 2024.

Test temp (°C)	Spec ID	Heat	Material Condition	Applied Stress (MPa)	Initiation Time (h)	Exposure time (h)
330	W11A-1	WP142	TT+11%CF	374	N/A	9022
330	W11A-2	WP142	TT+11%CF	352	N/A	2090
330	W11A-3	WP142	TT+11%CF	374	N/A	11112
330	W21A-1	WP142	TT+21%CF	510	N/A	9022
330	W21A-2	WP142	TT+21%CF	480	N/A	2090
330	W21A-3	WP142	TT+21%CF	522	N/A	11112
330	W31A-1	WP142	TT+31%CF	646	N/A	9022
330	W31A-2	WP142	TT+31%CF	621	N/A	2090
330	W31A-3	WP142	TT+31%CF	647	N/A	11112
330	R29A-1	RE243	TT+29%CTS	667	N/A	9022
330	R29A-2	RE243	TT+29%CTS	626	N/A	2090
360	W11B-1	WP142	TT+11%CF	360	N/A	9038
360	W11B-3	WP142	TT+11%CF	360	N/A	9038
360	W21B-1	WP142	TT+21%CF	487	N/A	9038
360	W21B-3	WP142	TT+21%CF	487	N/A	9038
360	W31B-1	WP142	TT+31%CF	620	N/A	9038
360	W31B-3	WP142	TT+31%CF	620	N/A	9038
360	R29B-1	RE243	TT+29%CTS	633	N/A	9038
400	W11C-1	WP142	TT+11%CF	375	N/A	9021
400	W11C-3	WP142	TT+11%CF	376	N/A	9021
400	W21C-1	WP142	TT+21%CF	500	N/A	9021
400	W21C-3	WP142	TT+21%CF	502	N/A	9021
400	W31C-1	WP142	TT+31%CF	636	1750	2058
400	W31C-3	WP142	TT+31%CF	634	1300	1506
400	W31C-2	WP142	TT+31%CF	647	1915	2188

3.3.2   Creep test in 330°C air

The overall non-referenced DCPD strain response of the seven Alloy 690TT specimens tested in 330°C air during the 1st year exposure is provided in Figure 28. For the cold forged WP142 materials, the non-referenced strain rates roughly scale with specimen cold work level and applied stress. Interestingly, the highly CTS RE243 specimen exhibited a much lower strain rate than the highly CF WP142 specimens, suggesting cold work method has affected material creep response and possibly resistivity evolution over time. Three specimens (W11A-3, W21B-3, and W31A-3) continued into the Phase II testing, and their DCPD strain responses are being continuously documented in the same figure. It is obvious that the strain evolution followed the same trend after the restart of the test in these three specimens, suggesting the reloading of the test specimens was adequate. The non-referenced DCPD strain response of the four new specimens added to the Phase II testing is also provided in Figure 29, suggesting the strain rate of the speicmens are settling down after the initial rapid decrease in resistivity drift and the passing of the primary creep stage.

SEM examinations performed at the test interruption after the completion of the first year exposure did not find any obvious cracks on the gauge surface of any specimens. Representative images of GB morphology of the four material conditions evaluated are shown in Figure 30. HAGBs are revealed by the semi-continuous distribution of carbides with little indication of significant oxidation. These images were taken in the area where the FIB trench was made for GB sliding evaluation, and no evidence of measurable GB sliding was found in any tested specimens.

Figure 28. Overall non-referenced DCPD strain response of the seven Alloy 690TT specimens tested in 330°C air during the 1st year exposure, and the three specimens stayed in test for Phase II testing. This test is ongoing as of June 2024.
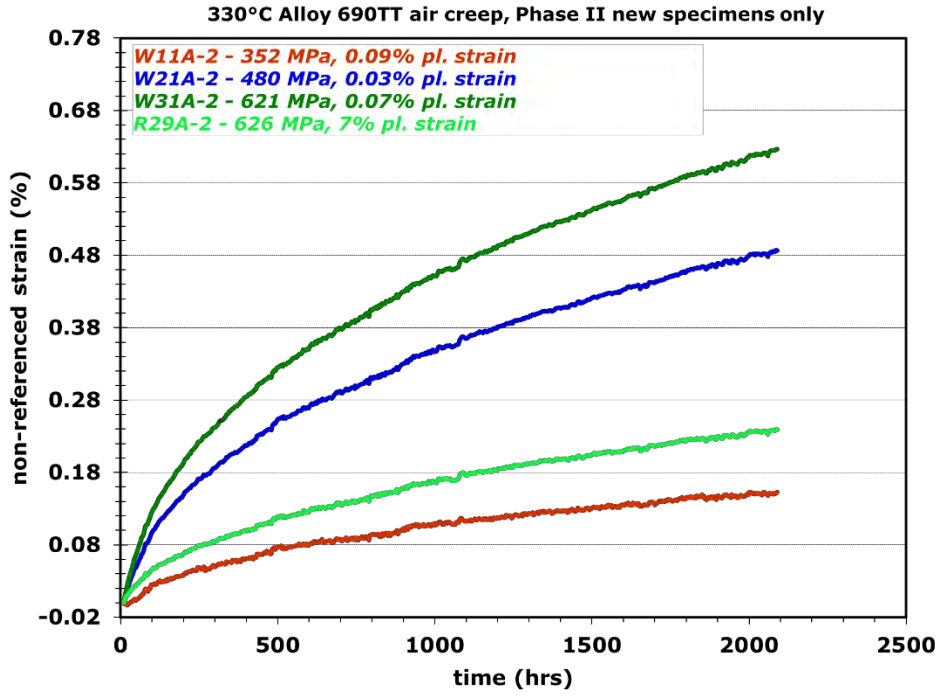
Figure 29. Overall non-referenced DCPD strain response of the four new Alloy 690TT specimens added to the Phase II testing in 330°C air. This test is ongoing as of June 2024.
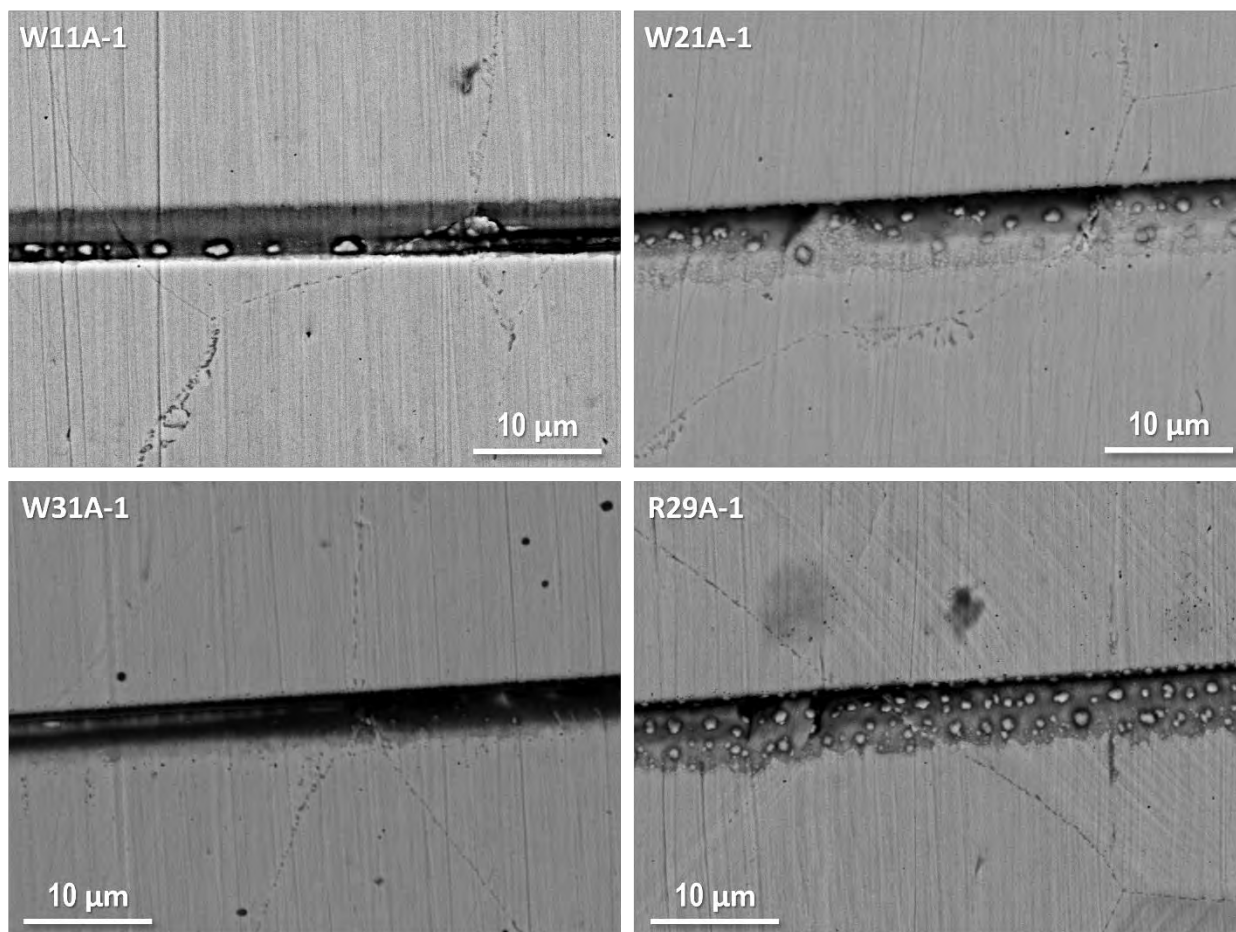
Figure 30. Representative grain boundary morphology crossing the FIB trenches in the creep specimens tested in 330°C air after 9022 hours of exposure.

3.3.3 Creep test in 360°C air

Figure 31 shows the non-referenced DCPD strain response of the seven Alloy 690TT specimens tested in 360°C air during the 1st year exposure. The steady-state creep strain rates of the specimens showed a similar trend to what was observed on the specimens tested at 330°C. The creep strain rates in the cold forged WP142 materials generally decreased with decreasing cold work level and applied stress, while the Valinox RE243 TT+29%CTS specimen R29B-1 exhibited a similar strain rate as those observed in the low to moderately cold forged Valinox WP142 Alloy 690TT specimens.

The Phase I exposure stopped after a total exposure time of 9038 hours on all specimens. No macroscopic crack initiation was detected by DCPD in any specimens. SEM surface examinations performed on all specimens after Phase I exposure only found a handful of short cracks in the specimens with the highest cold work levels. SEM-BSE montage images of the surface of the gauge section and part of the fillet region of the Valinox WP142 TT+31%CF specimens W31B-1 and W31B-3 are shown in Figures 32 and 33, respectively, where obvious IG cracks are marked in red. Higher magnification SEM-BSE images on examples of these cracks in each specimen are presented in Figure 34. These cracks are generally ~10–20 μm long on the surface and appear to have been formed by the coalescence of submicrometer-sized voids packed on the GBs. The density of the observed voids is much higher than the pre-existing defects produced by cold forging, indicating they are creep-induced cavities instead of GB damage produced during cold forging. Currently the W31B-1 specimen has been cross-sectioned and

38

SEM examinations will be performed on one cross-section after it is polished to characterize the cavity morphology and quantify their density.

A few IG cracks were also observed in the Valinox RE243 TT+29%CTS specimen R29B-1 after Phase I exposure. In Figure 35, the location of these obvious IG cracks are both shown in the low-magnification montage image of the entire specimen gauge surface (Figure 35a) and high-magnification images for more detailed morphology documentation (Figure 35b and c). It is interesting to note that near the obvious crack shown in Figure 35b, another GB showed segments of semi-continuous voids indicative of a possible crack. Similar features were observed on one end of the obvious cracks shown in Figure 35c. serial milling was performed using focused ion beam (FIB) on these two GBs to document the damage profile in depth. The result of the GB marked in Figure 35b is summarized in Figure 36. While some damage appears to be similar to the ones produced by pre-test cold work, enlarged voids around GB carbides were observed in multiple FIB slices. However, FIB serial trenching on the other GB did not reveal solid evidence of GB cavity formation (Figure 37). This specimen has also been cross-sectioned. Polish is underway in preparation for cross-section examinations to quantify the extent of IG damage inside.
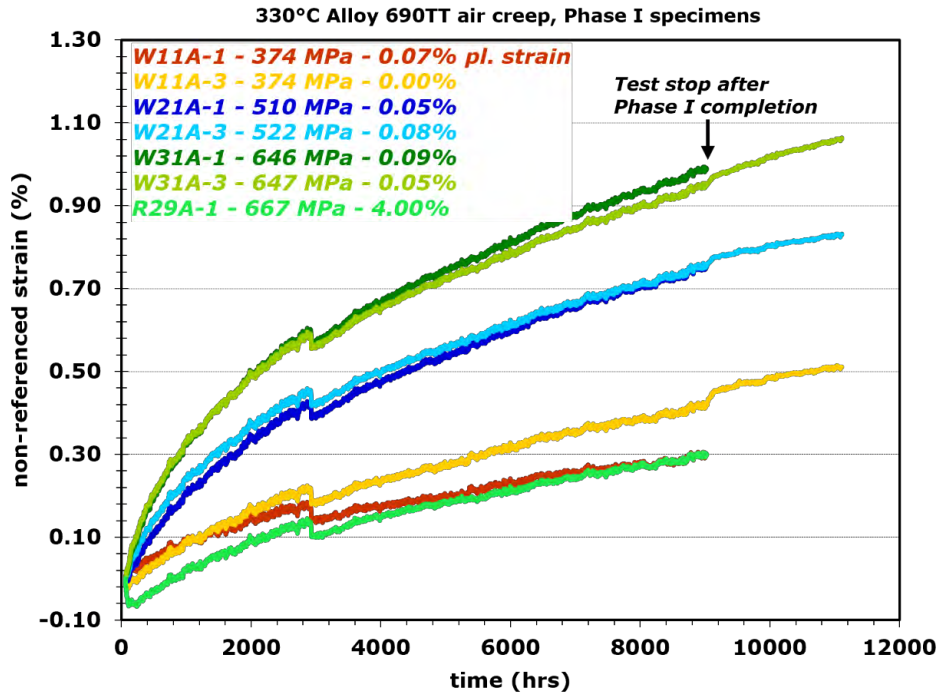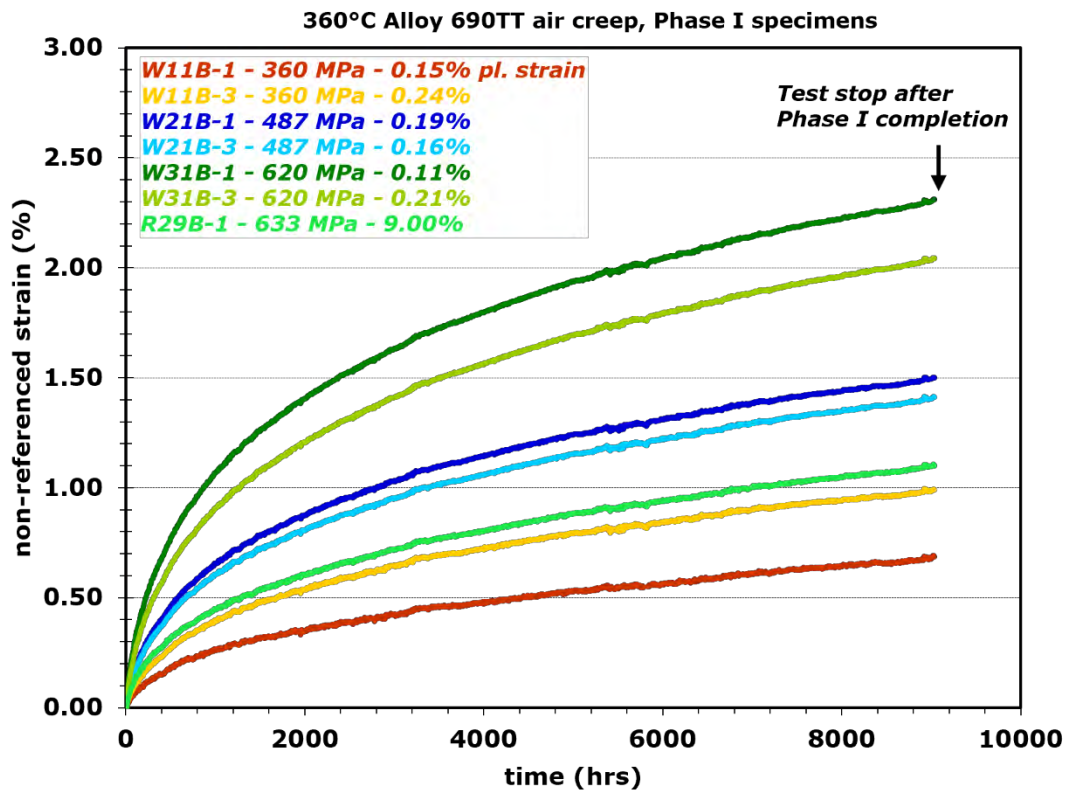

Figure 31. Overall non-referenced DCPD strain response of the seven Alloy 690TT specimens tested in 360°C air during Phase I exposure.
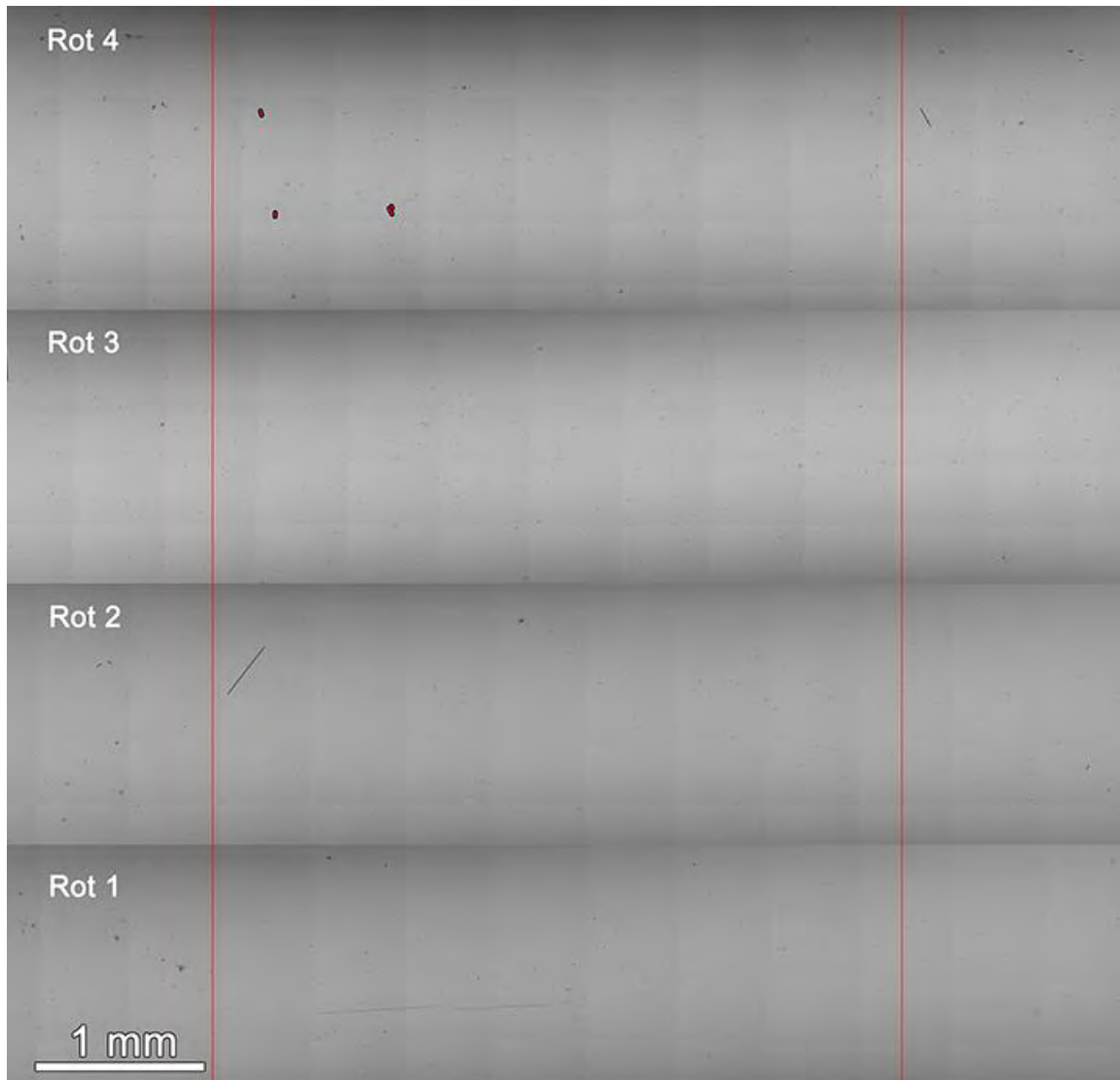
Figure 32. SEM-BSE montage image of the Valinox WP142 TT+31%CF specimen W31B-1 tested in 360°C air after 9038 hours. The gauge section of the specimen is between the two red lines marked in the image. Obvious cracks are highlighted in red.
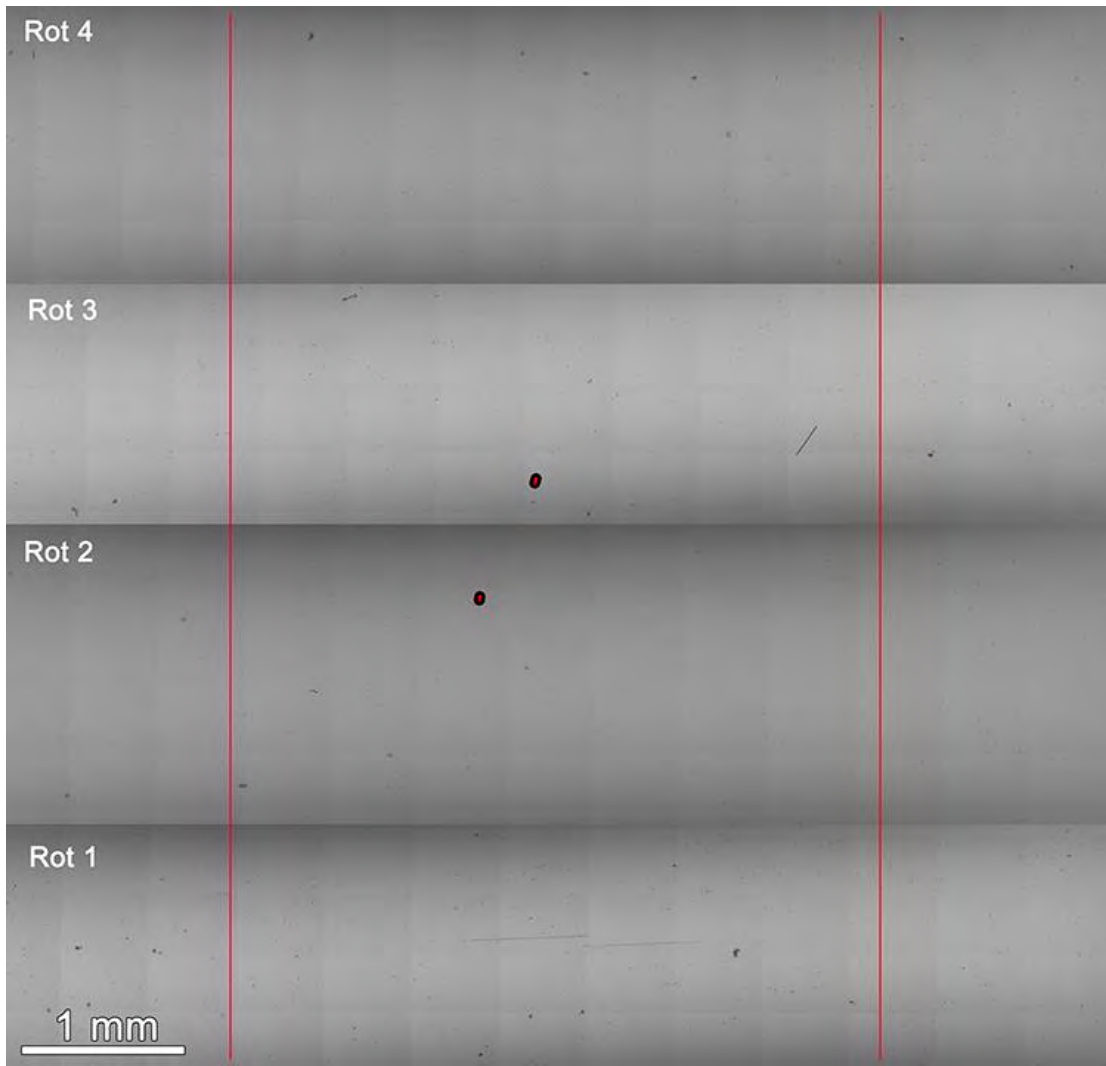
Figure 33. SEM-BSE montage image of the Valinox WP142 TT+31%CF specimen W31B-3 tested in 360°C air after 9038 hours. The gauge section of the specimen is between the two red lines marked in the image. Obvious cracks are highlighted in red.
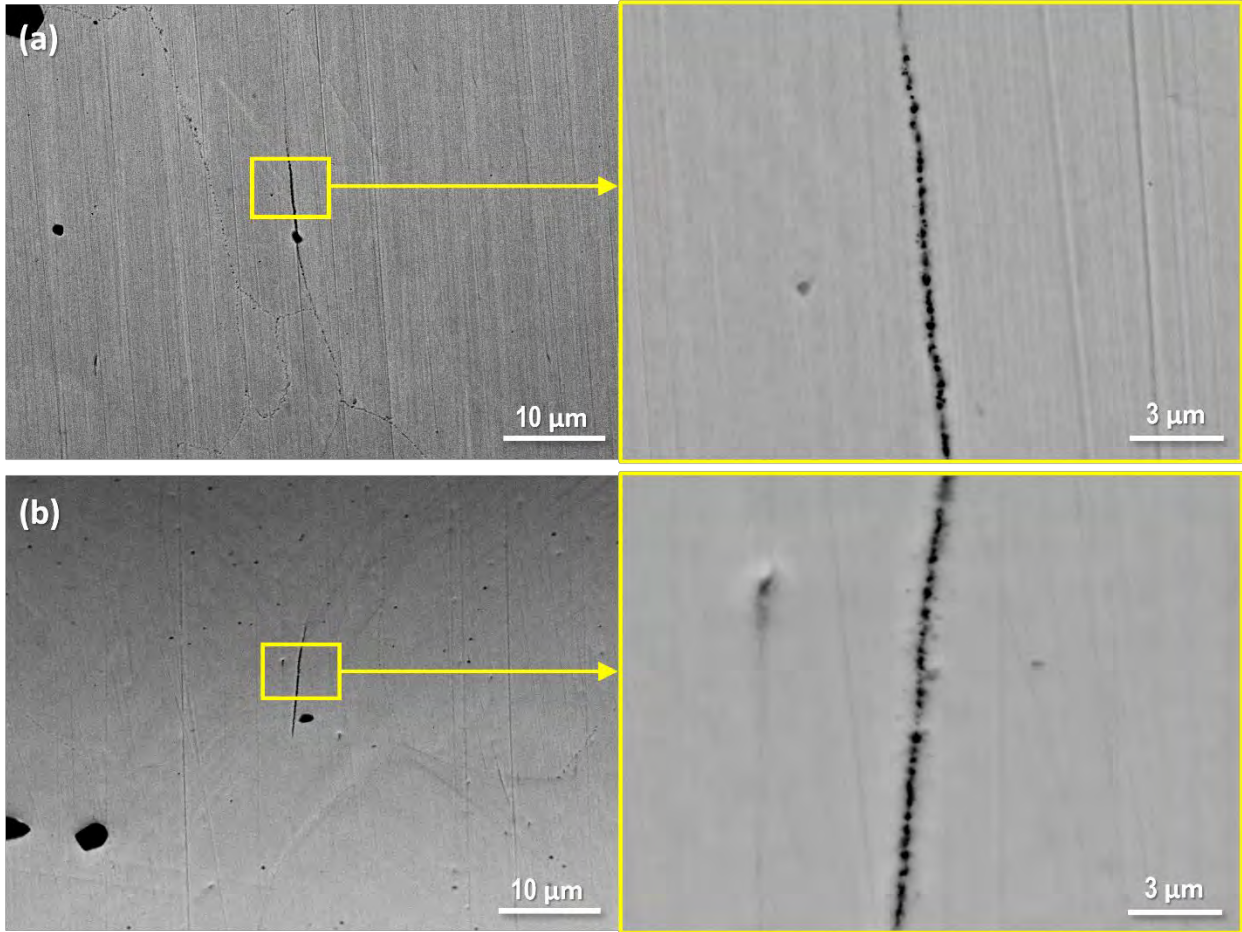
Figure 34. SEM-BSE images on representative IG cracks found on the surface of the two Valinox WP142 TT+31%CF specimens (a) W31B-1 and (b) W31B-3 tested in 360°C air after 9038 hours.
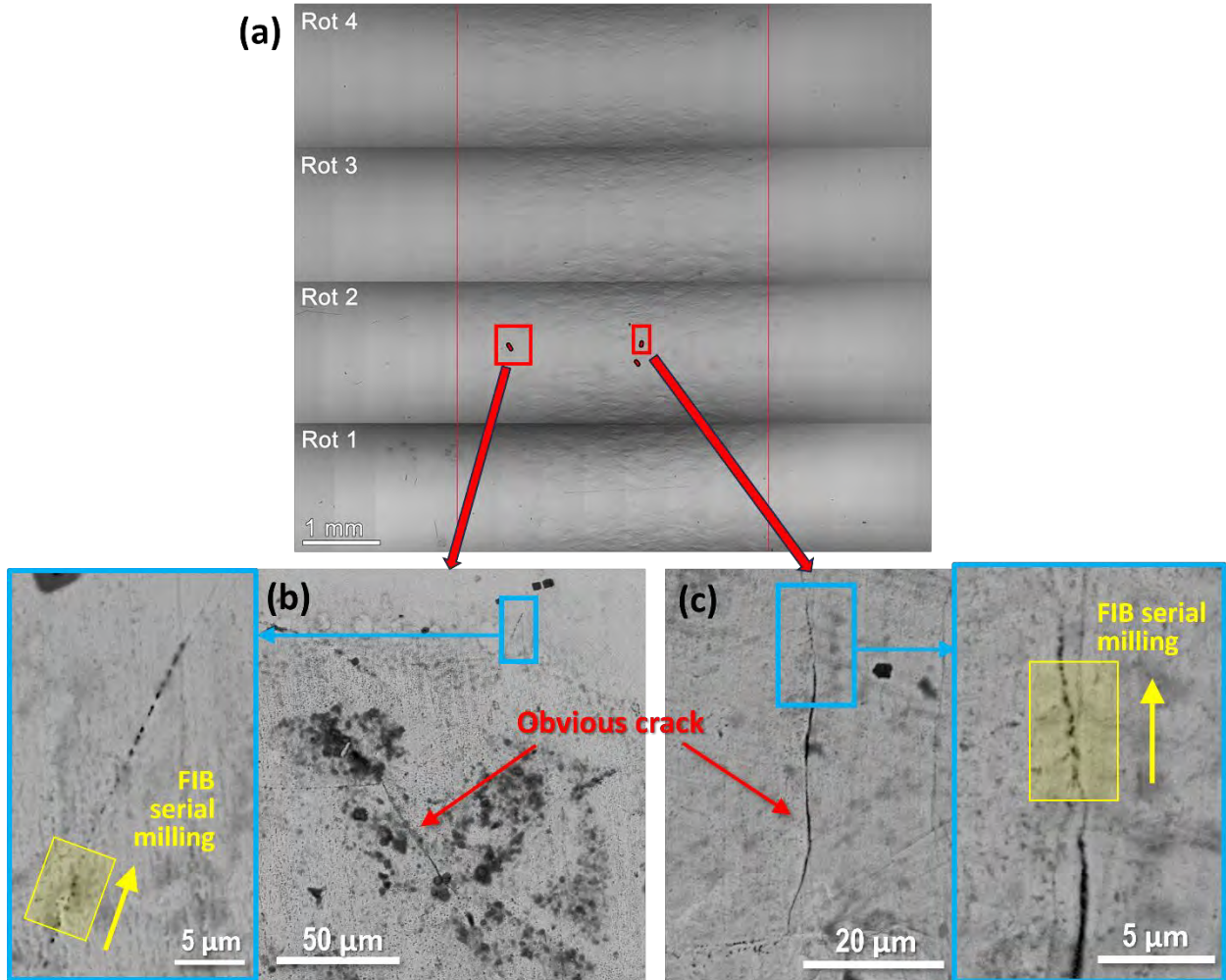
Figure 35. (a) SEM-BSE montage image of the surface morphology of the Valinox RE243 TT+29%CTS specimen R29B-1 tested in 360°C air after 9038 hours. The gauge section of the specimen is between the two red lines marked in the image. IG cracks identified on the surface are highlighted in red. Zoom-in images of two cracks are presented in (b) and (c). The region where FIB serial milling was performed is marked.
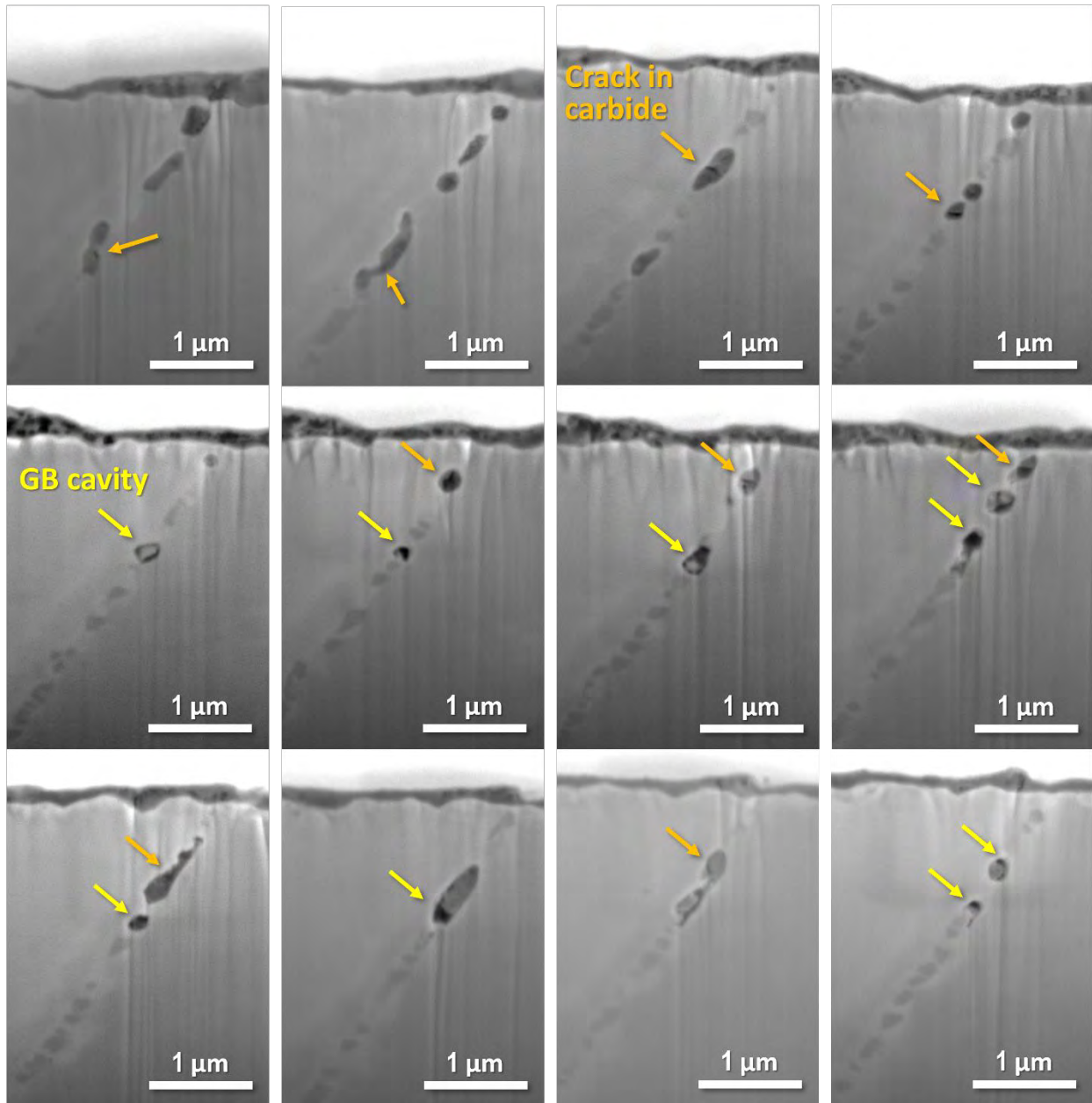
Figure 36. Examples of IG oxide morphology in cross-sections revealed during FIB serial milling on the possible crack marked in Figure 35(b).
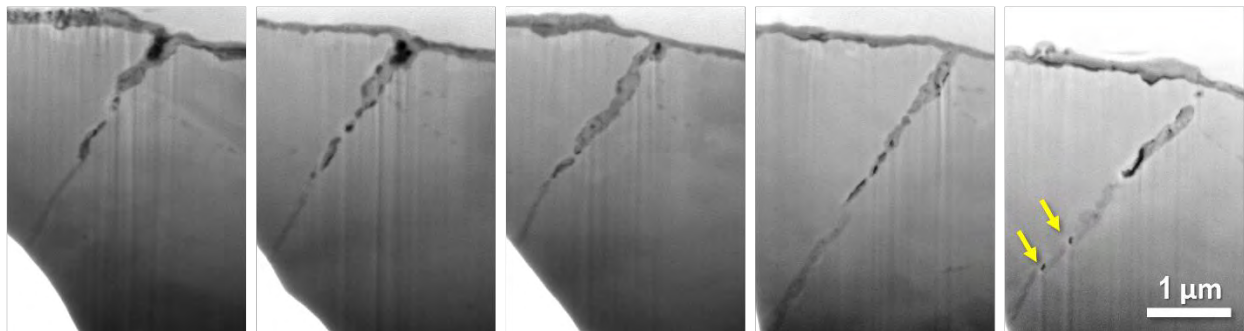
Figure 37. Examples of IG oxide morphology in cross-sections revealed during FIB serial milling on the obvious crack marked in Figure 35(c).

3.3.4   Creep test in 400°C air

The overall non-referenced DCPD strain response of the Alloy 690TT specimens tested in 400°C air during Phase I exposure is shown in Figure 38. Unlike the tests performed at lower temperatures in which no DCPD detection of crack initiation has been confirmed in any specimen during the first year of exposure, the Valinox WP142 TT+31%CF W31C-3 specimen initiated after only ~1300 hours at 400°C. The test was stopped soon after and replaced W31C-3 with a new specimen W31C-2. As shown in Figure 39, DCPD detected crack initiation in W31C-1 at ~1750 hours and in W31C-2 at ~1915 hours, demonstrating consistent behavior among all three highly cold forged WP142 Alloy 690TT specimens.

Macroscopic crack initiation was not detected by DCPD in specimens tested at lower cold forge levels, but SEM examinations performed after Phase I exposure revealed possible (semi-continuous darker delineation along GBs in the surface montage images) and obvious (continuous darker delineation along GBs in the surface montage images) IG cracks in all of them, of which the density scales with cold work level and applied stress. The Valinox WP142 TT+11%CF W11C-1 and W11C-3 specimens mostly showed possible IG cracks featuring non-continuous but highly packed voids along GBs (Figures 40–42). The density of cracks in these specimens is low to moderate, usually between 1 – 40 in each of the four rotations of a specimen shown in these figures.

A dramatic increase in crack density was observed in the Valinox WP142 TT+21%CF specimens, where each rotation was covered by hundreds of identifiable cracks (Figures 44 and 45). Zoom-in images of a randomly chosen site in these specimens are shown in Figure 46. It is apparent that the cracks are higher in density per unit area and longer in surface length than those found in the low CF specimens. FIB serial milling was performed on cracks randomly selected in the TT+11%CF and TT+21%CF specimens with results summarized in Figure 43 for specimen W11C-3 and Figure 47 for specimen W21C-3. Consistent with what was observed on the surface, these cracks feature a high density of enlarged GB cavities beneath the surface that ran a few to tens of micrometers deep. In fact, they seem to have reached a similar extent to the GB cavities found in TT+31%CF Alloy 690 specimens tested for a year in simulated PWR primary water at 360°C, suggesting a much faster kinetics once the temperature is raised to 400°C. Cross-section examinations are under preparation for these specimens to quantify the GB cavity distribution.

The low-magnification surface montage of the three initiated Valinox WP142 TT+31%CF specimens are shown in Figures 48–50. Possible cracks are not marked in these images because their density was too high, but zoom-in images at a random site showcasing the typical morphology of both possible and obvious cracks are provided in Figure 51. W31C-2 has already been cross-sectioned along the line marked in Figure 49 and its cross-section morphology is summarized in Figure 52. Continuous (i.e., creep

cracks) and semi-continuous (i.e., aggregations of GB cavities) IG damage features are highlighted in yellow in Figure 52a. A random crack connected to the surface is presented in Figure 52b confirming that it is formed by coalescence of GB cavities, and the longest crack found in the cross-section is shown in Figure 52c with a total length reaching 215 μm. In addition, it is obvious that GB cavity aggregations have formed throughout the specimen in the highly stressed gauge section, and their density dropped quickly towards the fillet region where the applied stress decreased because of the increasing diameter in the direction perpendicular to the loading direction.
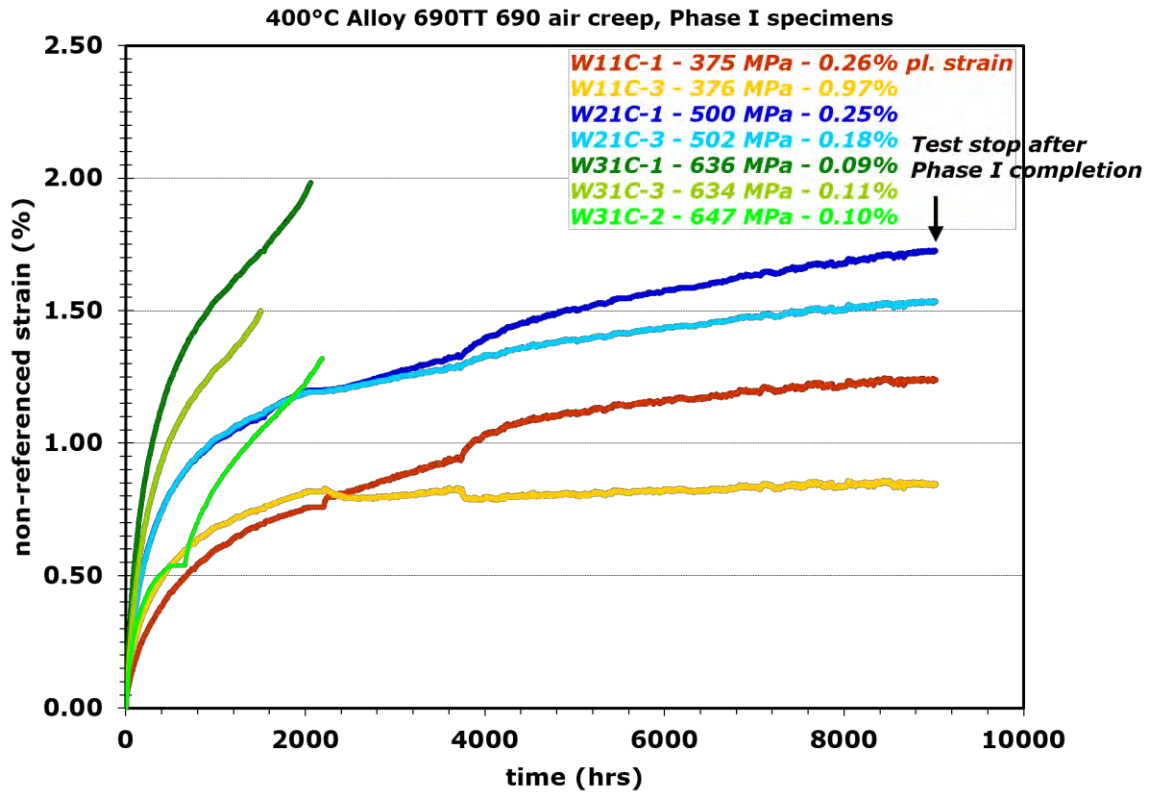
Figure 38. Overall non-referenced DCPD strain response of the seven Alloy 690TT specimens tested in 400°C air during Phase I exposure.
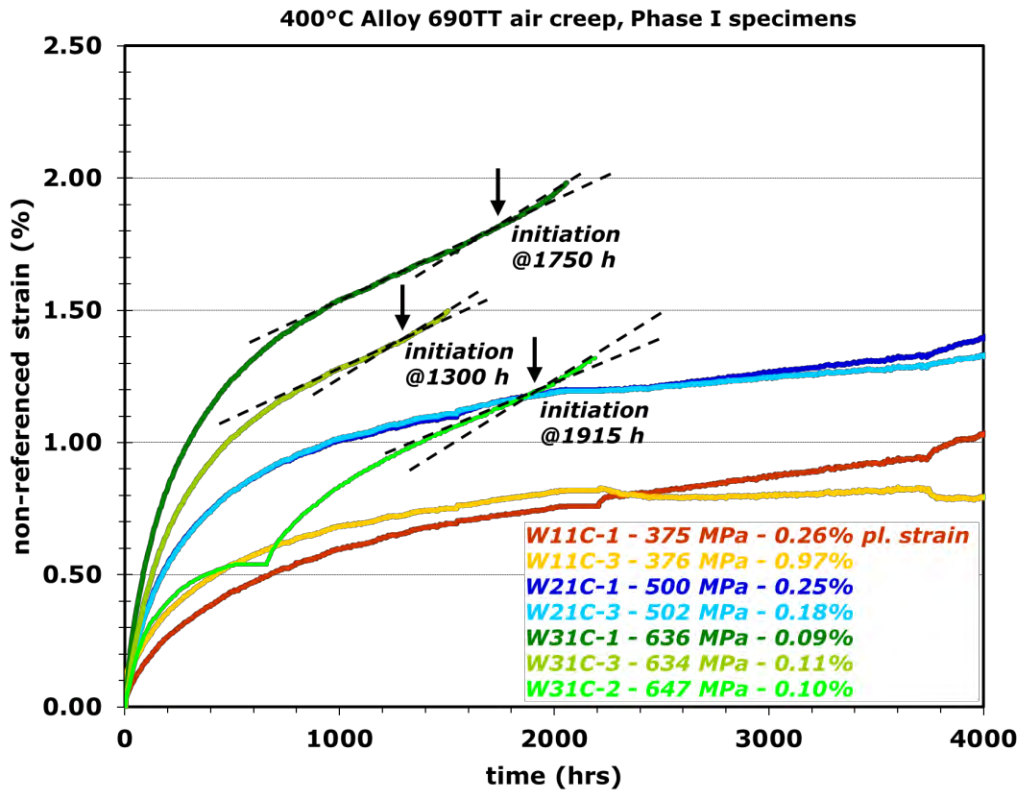
Figure 39. A closer look at the three Alloy 690 WP142 TT+31%CF specimens' non-referenced DCPD strain response among the seven Alloy 690TT specimens tested in 400°C air during Phase I exposure.
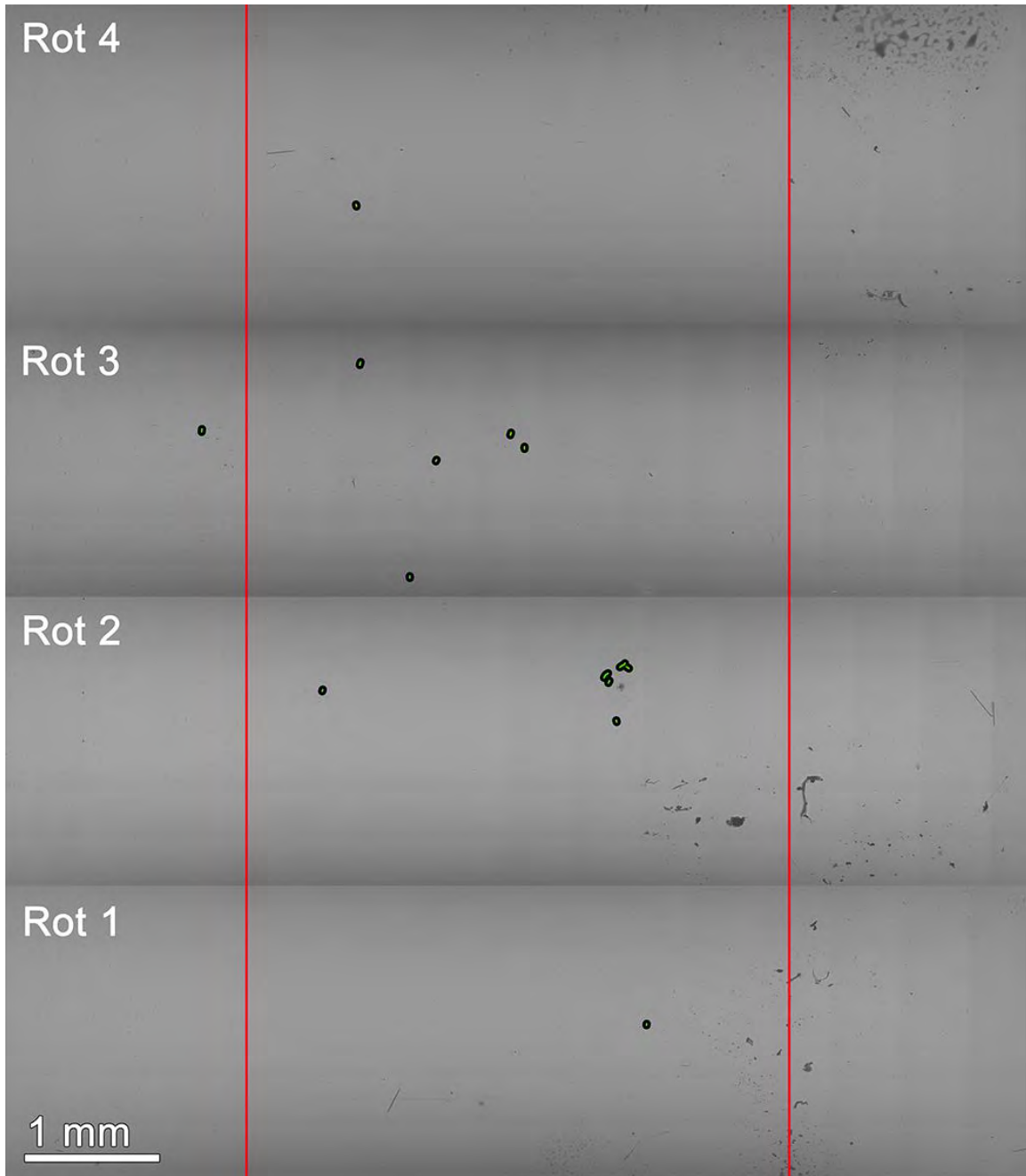
Figure 40. SEM-BSE montage image of the Valinox WP142 TT+11%CF specimen W11C-1 tested in 400°C air after 9021 hours. The gauge section of the specimen is between the two red lines marked in the image. Possible cracks are highlighted in green.
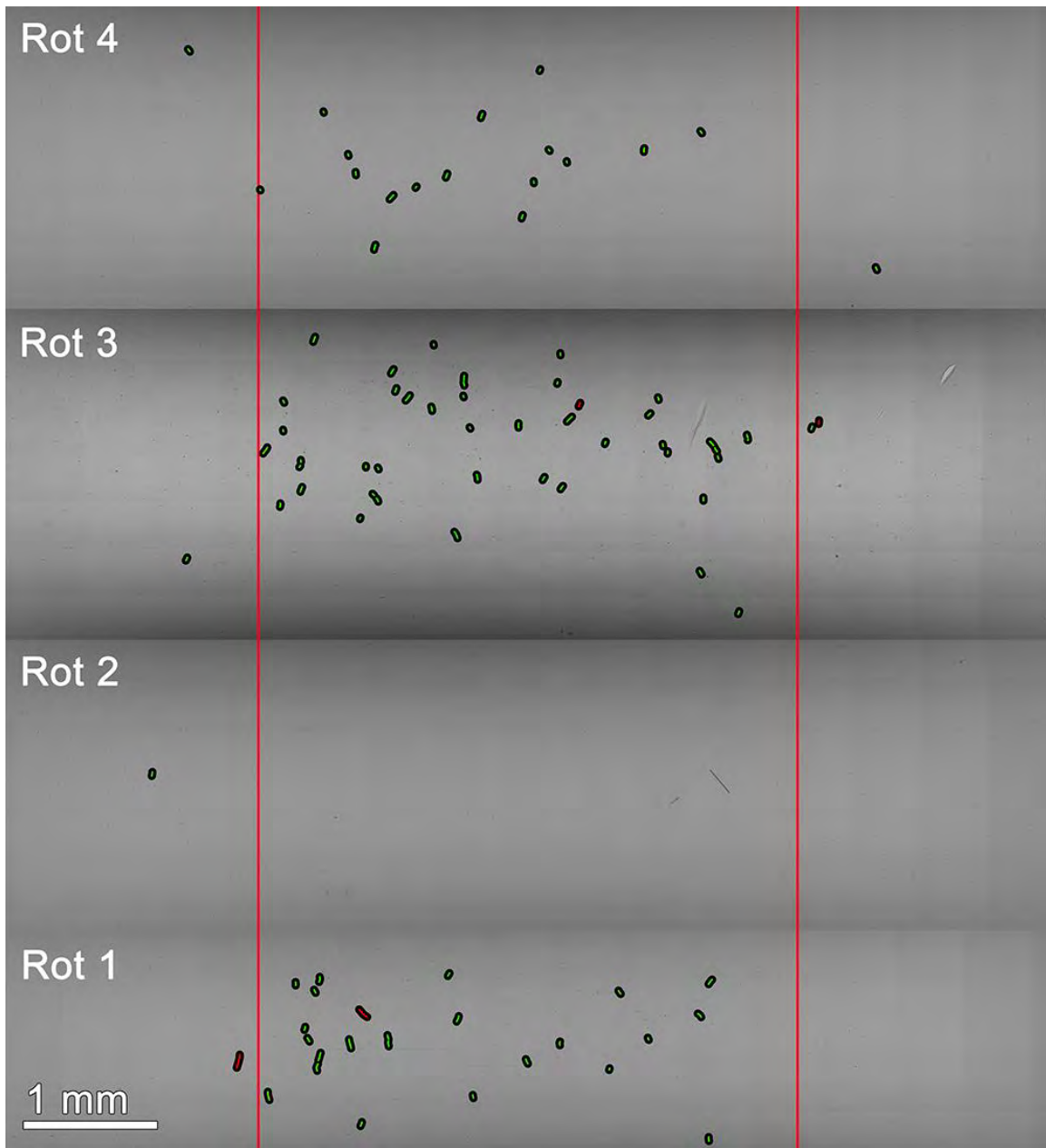
Figure 41. SEM-BSE montage image of the Valinox WP142 TT+11%CF specimen W11C-3 tested in 400°C air after 9021 hours. The gauge section of the specimen is between the two red lines marked in the image. Obvious cracks and possible cracks are highlighted in red and green, respectively.
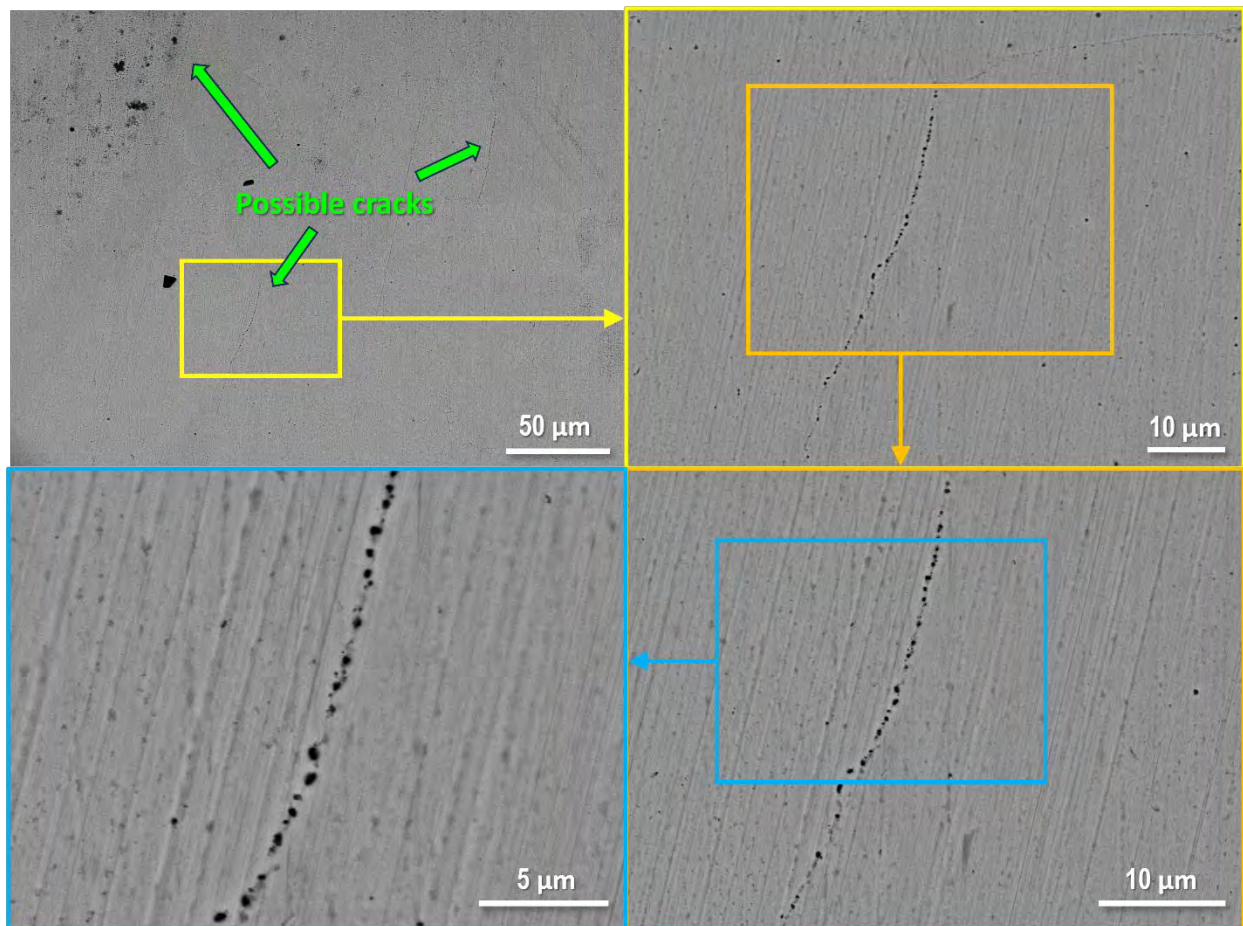
Figure 42. SEM-BSE images showing the morphology of typical possible cracks found in the Valinox WP142 TT+11%CF specimen W11C-3 tested in 400°C air after 9021 hours.
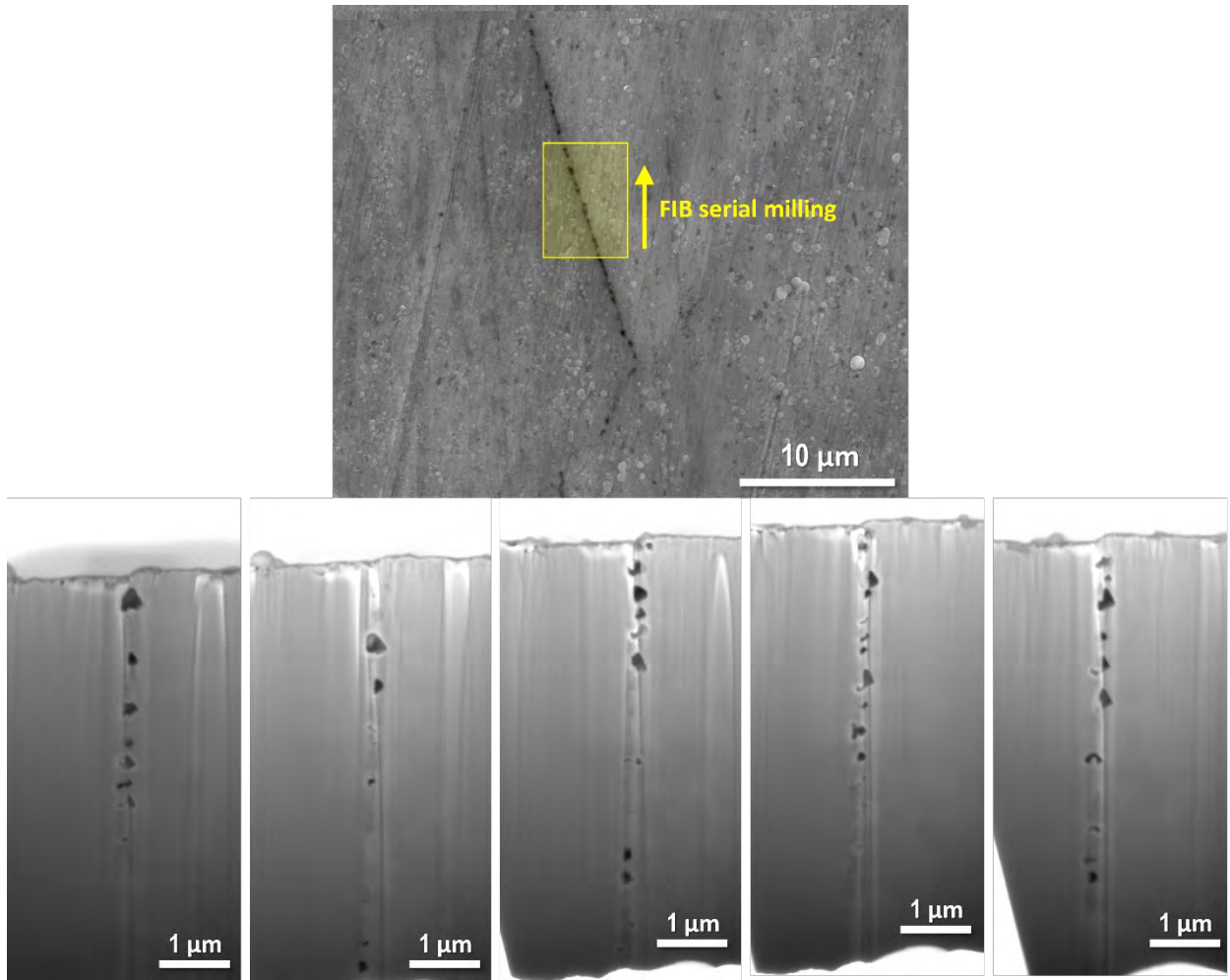
Figure 43. Examples of GB cavities in cross-sections revealed during FIB serial milling on a randomly chosen possible crack found on the surface of the Valinox WP142 TT+11%CF W11C-3 tested in 400°C air after 9021 hours.
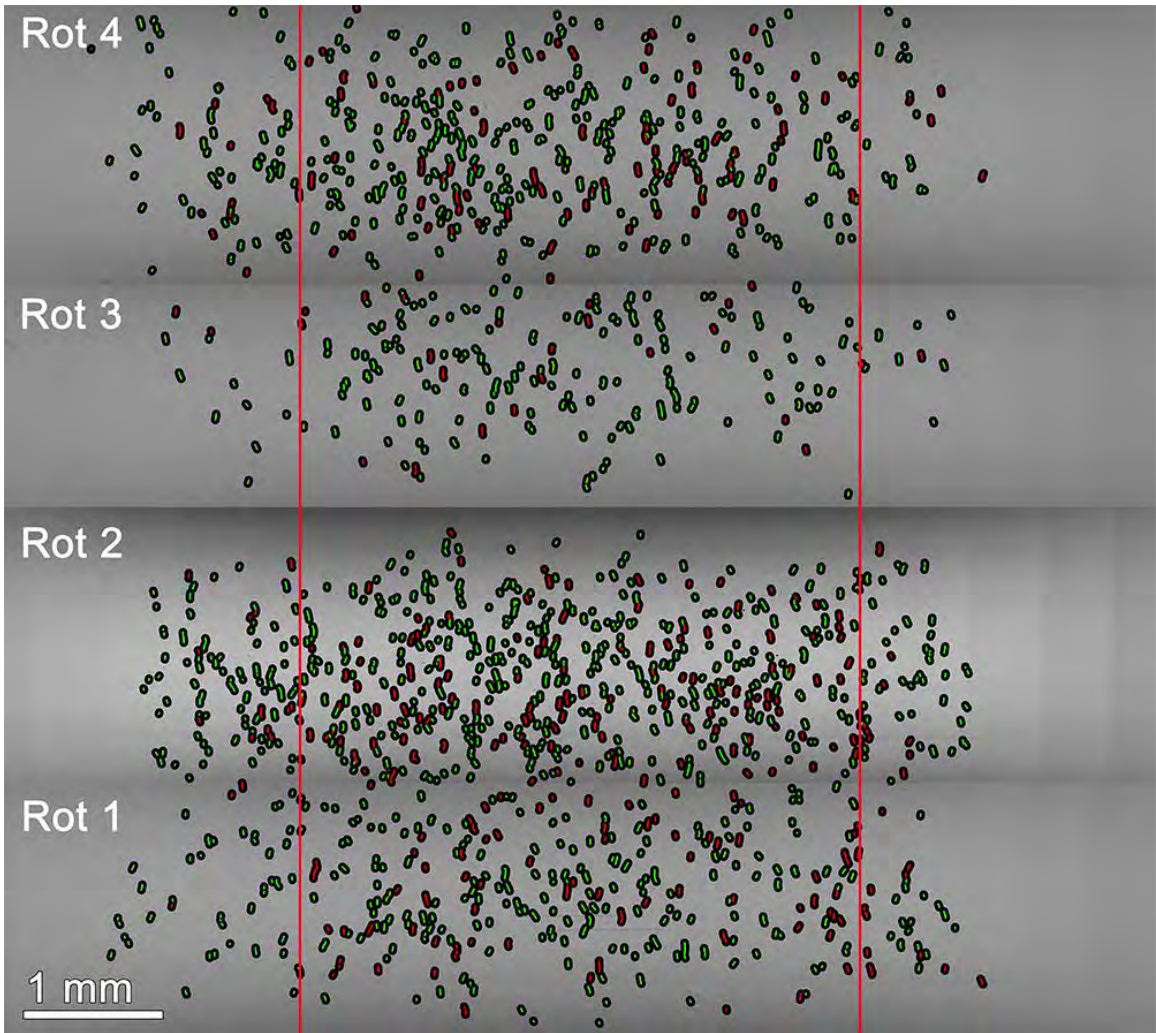
Figure 44. SEM-BSE montage image of the Valinox WP142 TT+21%CF specimen W21C-1 tested in 400°C air after 9021 hours. The gauge section of the specimen is between the two red lines marked in the image. Obvious cracks and possible cracks are highlighted in red and green, respectively.
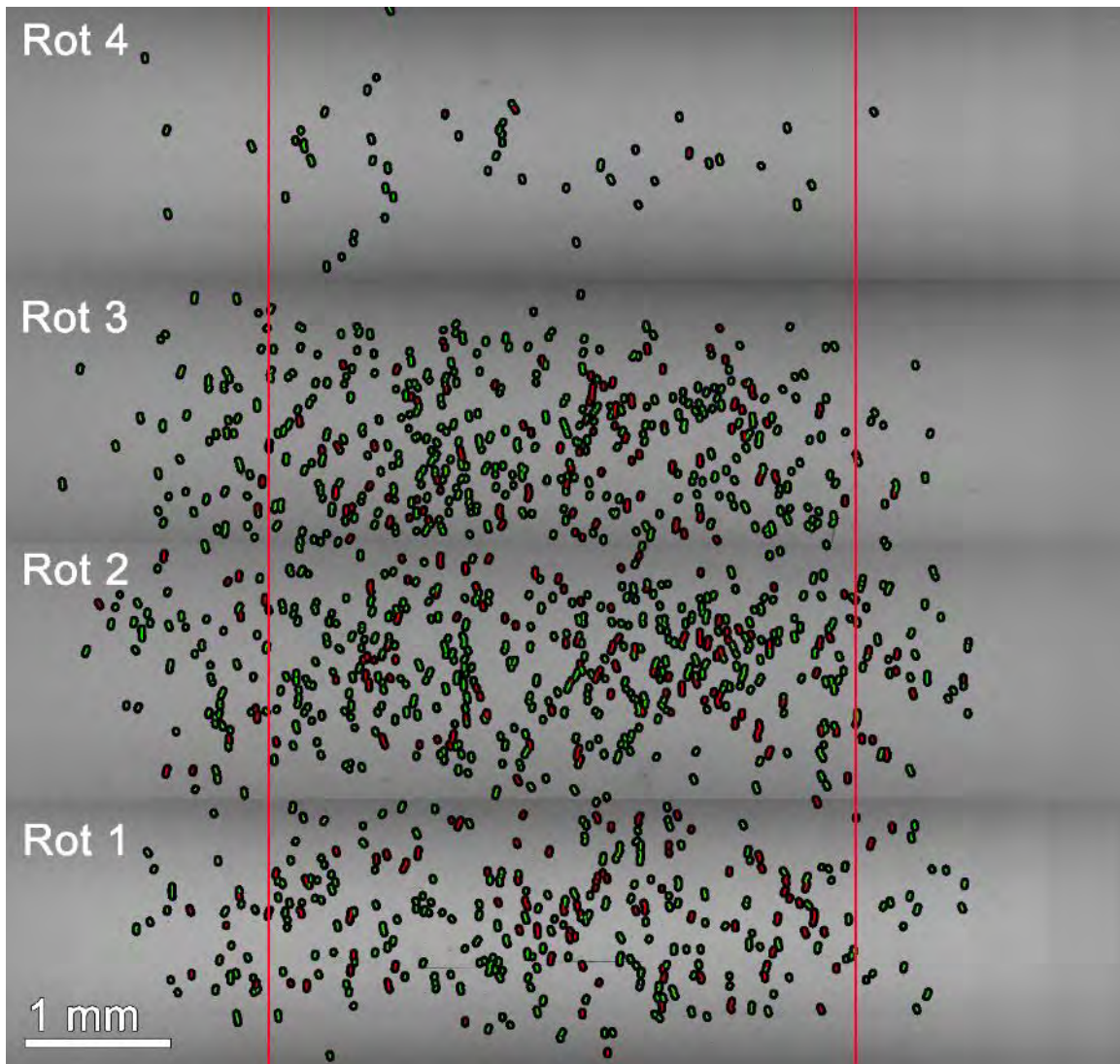
Figure 45. SEM-BSE montage image of the Valinox WP142 TT+21%CF specimen W21C-3 tested in 400°C air after 9021 hours. The gauge section of the specimen is between the two red lines marked in the image. Obvious cracks and possible cracks are highlighted in red and green, respectively.
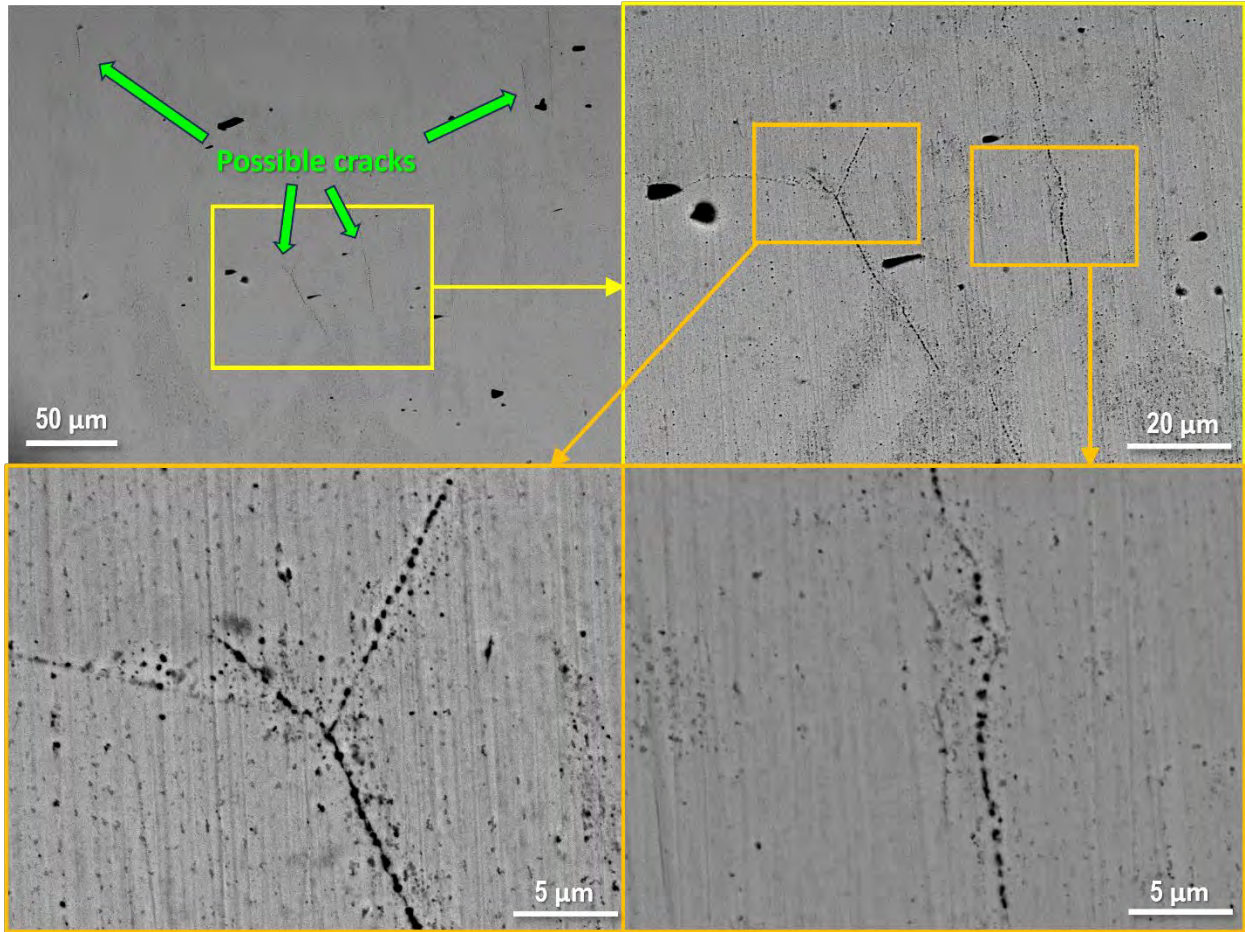
Figure 46. SEM-BSE images showing the morphology of typical possible cracks found in the Valinox WP142 TT+21%CF specimen W21C-3 tested in 400°C air after 9021 hours.
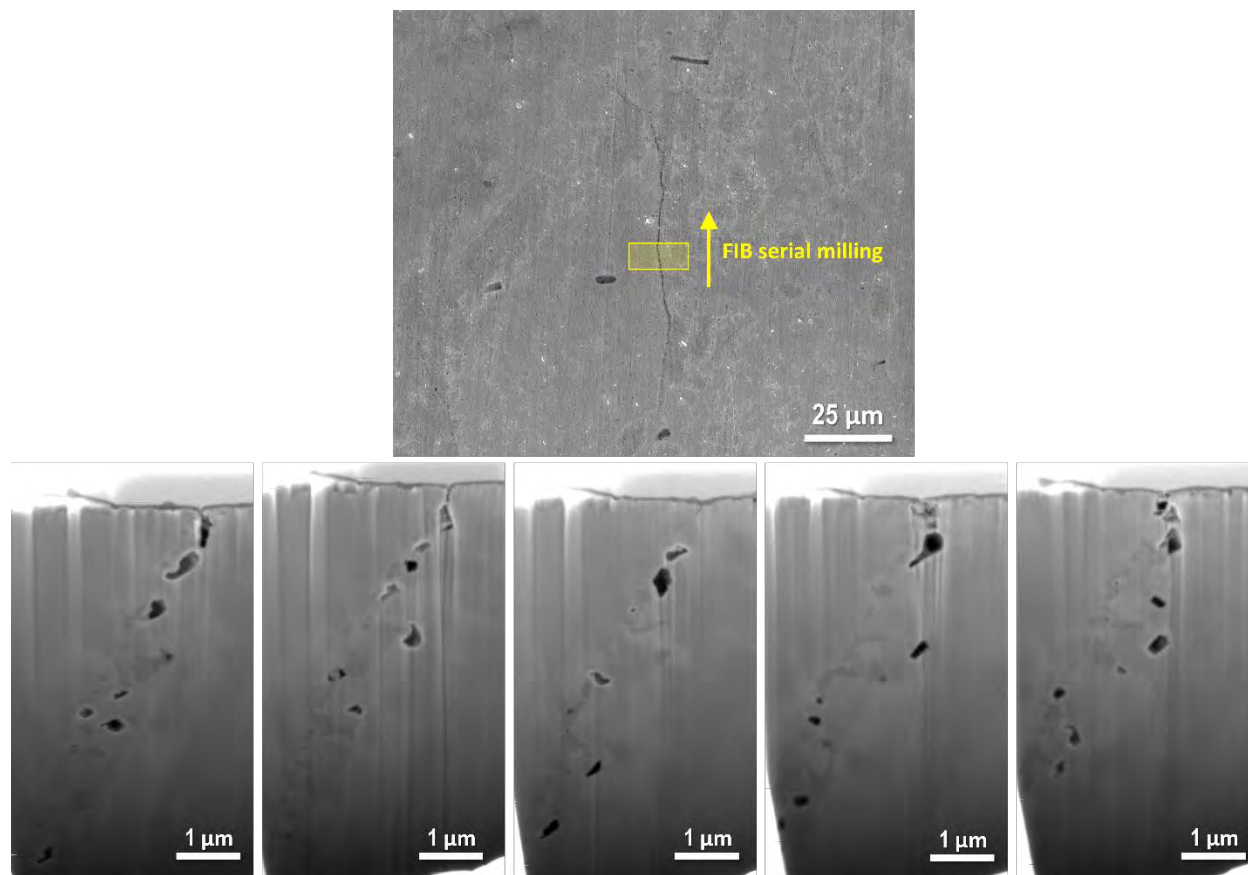
Figure 47. Examples of GB cavities revealed in cross-sections during FIB serial milling on a randomly chosen possible crack found on the surface of the Valinox WP142 TT+21%CF W21C-3 tested in 400°C air after 9021 hours.
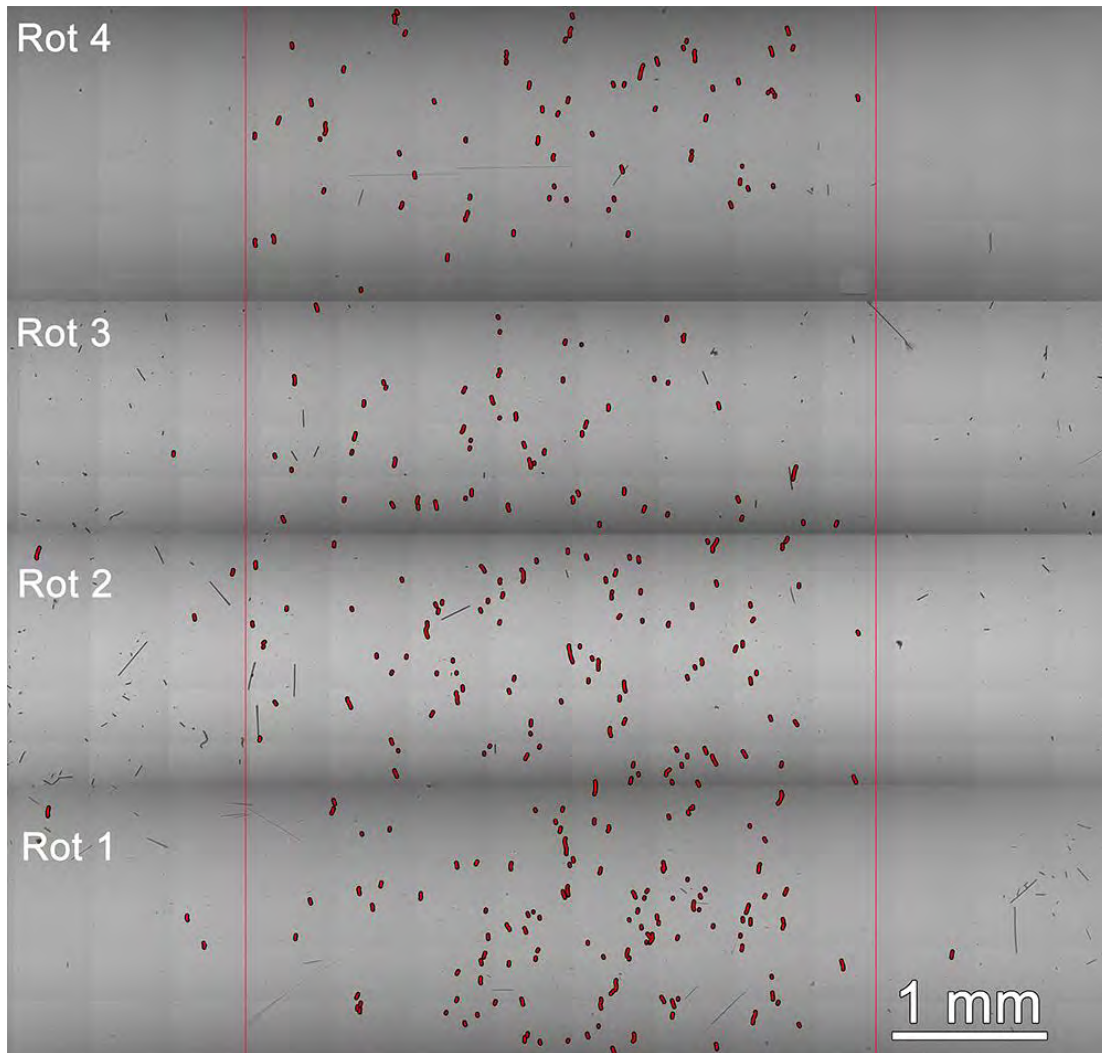
Figure 48. SEM-BSE montage image of the Valinox WP142 TT+31%CF specimen W31C-1 tested in 400°C air after 9021 hours. The gauge section of the specimen is between the two red lines marked in the image. Obvious cracks are highlighted in red. Possible cracks are not marked because the density is too high.
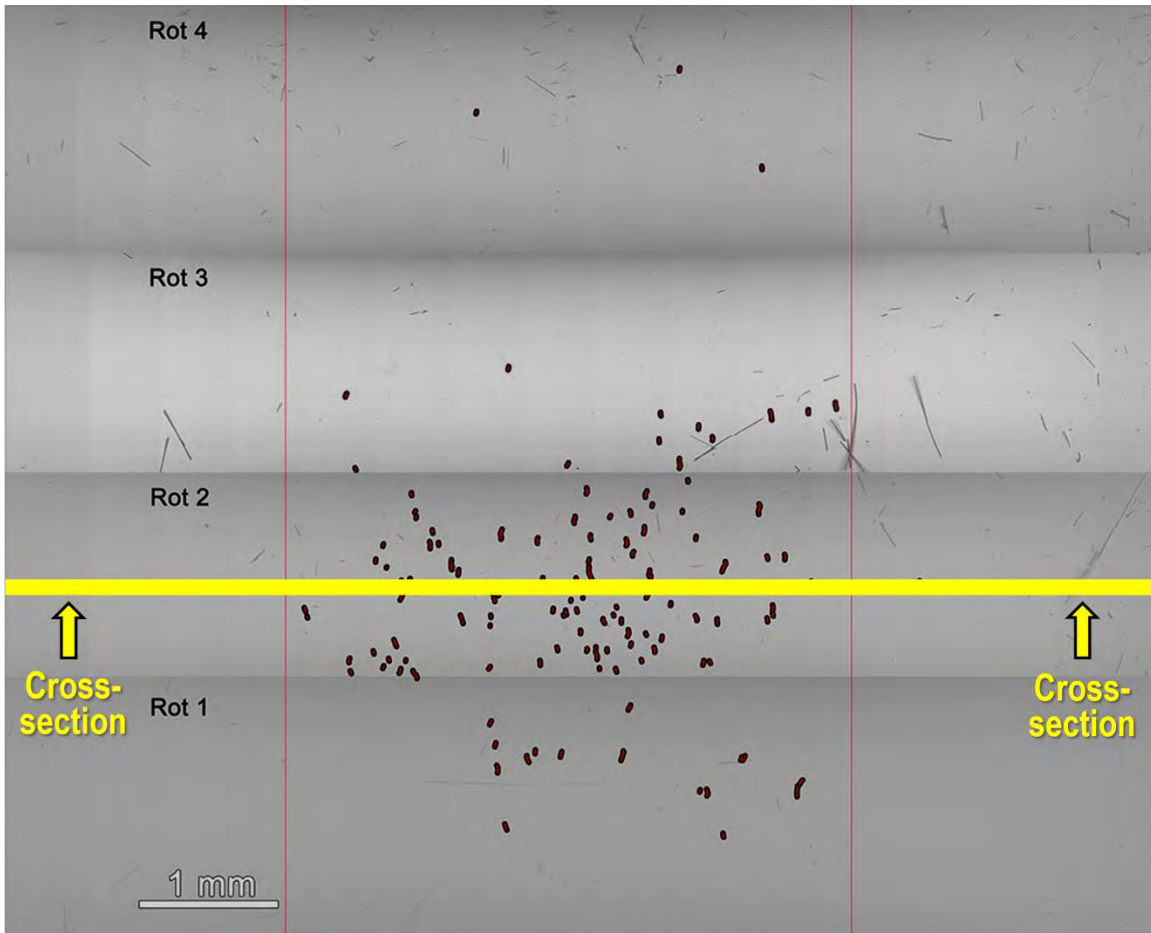
Figure 49. SEM-BSE montage image of the Valinox WP142 TT+31%CF specimen W31C-2 tested in 400°C air after 9021 hours. The gauge section of the specimen is between the two red lines marked in the image. Obvious cracks are highlighted in red. Possible cracks are not marked because the density is too high. The location where the specimen was cross-sectioned is also marked.
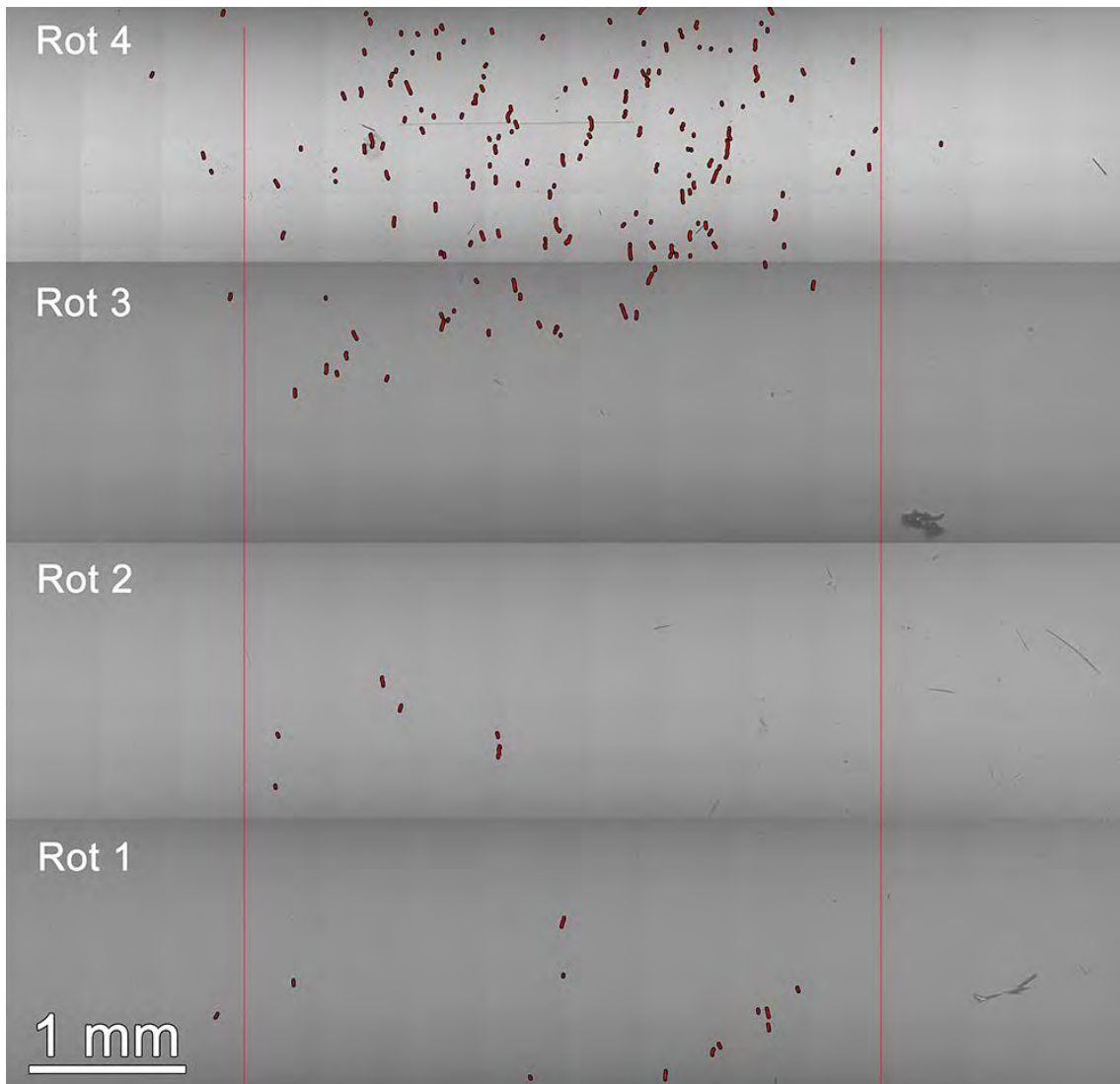
Figure 50. SEM-BSE montage image of the Valinox WP142 TT+31%CF specimen W31C-3 tested in 400°C air after 9021 hours. The gauge section of the specimen is between the two red lines marked in the image. Obvious cracks are highlighted in red. Possible cracks are not marked because the density is too high.
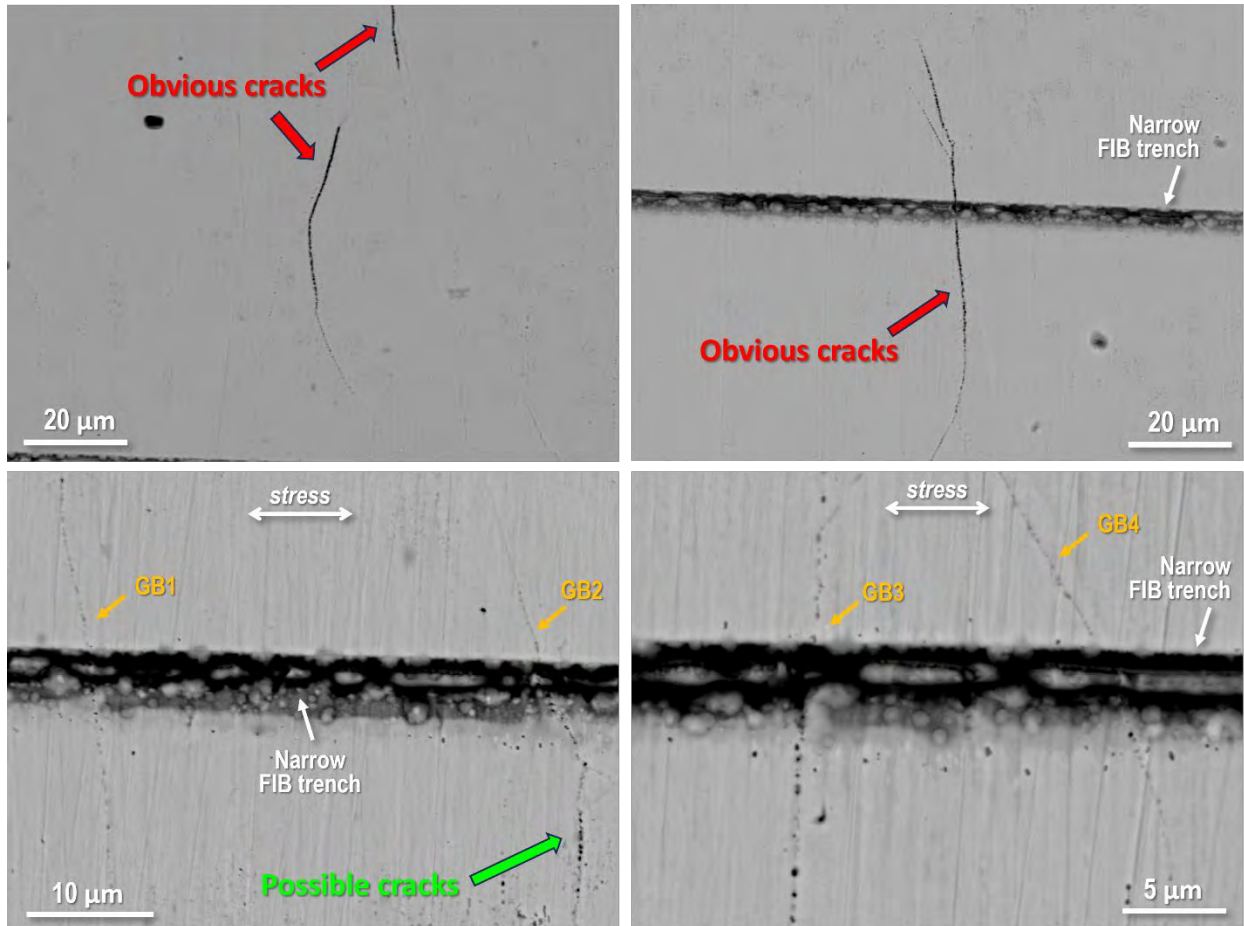
Figure 51. SEM-BSE images showing the morphology of typical obvious and possible cracks found in the Valinox WP142 TT+31%CF specimen W31C-3 tested in 400°C air after 9021 hours.
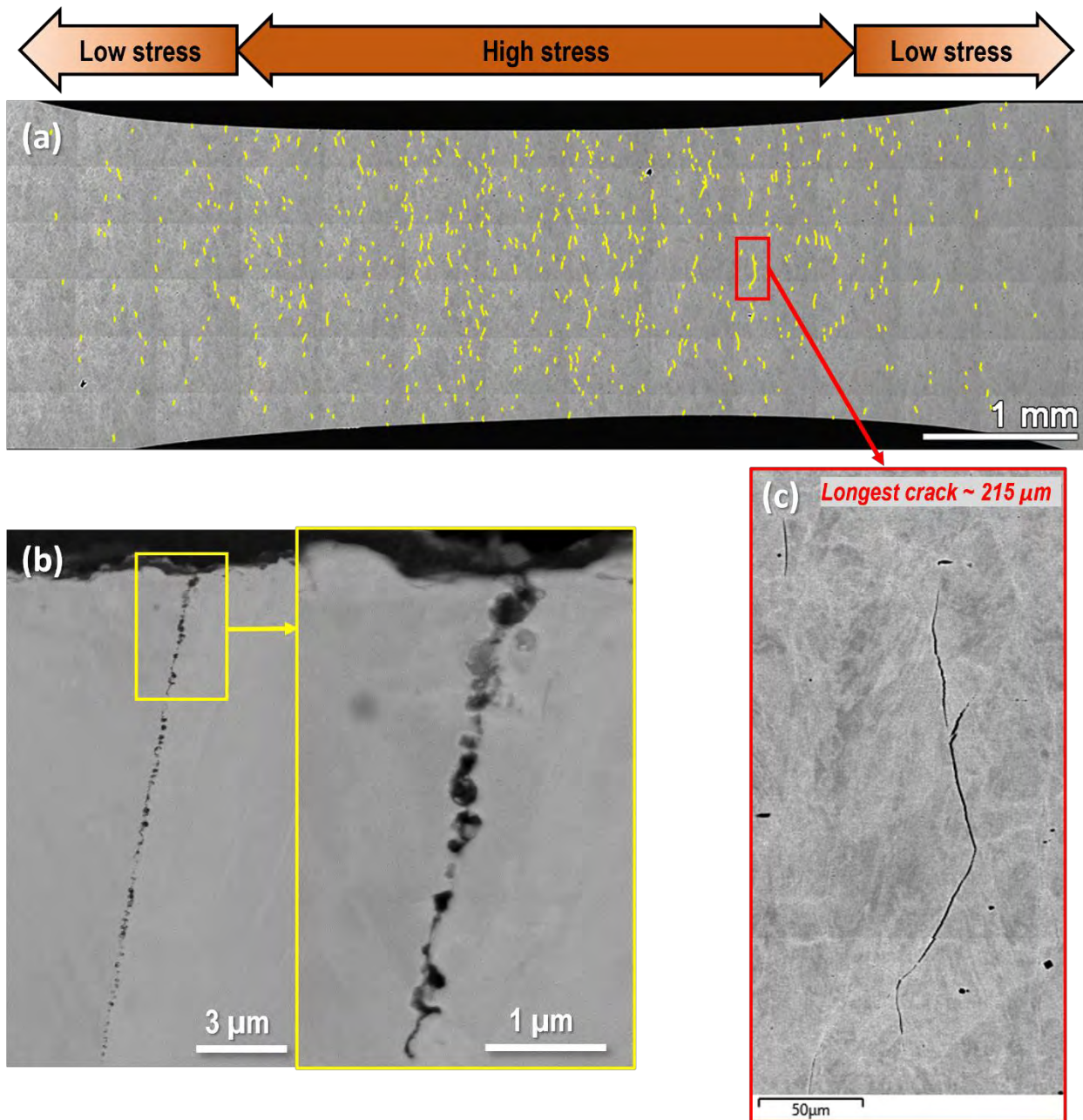
Figure 52. (a) SEM-BSE montage image of the cross-section of the Valinox WP142 TT+31%CF specimen W31C-2 tested in 400°C air after 9021 hours. Continuous and semi-continuous IG damage are highlighted in yellow. (b) Representative morphology of IG cracks intersected the specimen surface. (c) The longest IG crack found in this cross-section with a total length of ~215 μm.

4. SCC Initiation Testing of High-Cr Weld Metals

4.1 Chapter Overview

Ductility dip cracking (DDC) is recognized as a significant issue during the welding of high-Cr, Ni-based alloys. IG cracks are often produced in Ni-30Cr weld metals and may require weld repair. A critical question is whether the presence of pre-existing defects can promote SCC initiation and growth in service. To answer this question, LWRS has been collaborating with an NRC project at PNNL to perform SCC initiation test on selected weld materials. Two blunt notch compact tension (BNCT) specimens were machined from two EPRI mockups where DDC cracks were identified in Alloy 52M weld metal. The notch surfaces of these two specimens were specially prepared and highly polished to intersect pre-existing IG cracks in the weld metal. Long-term constant load SCC tests have been conducted at high load on these two specimens in 360°C simulated PWR primary water. The test was stopped every ~4,000 hours to document crack evolution on the notch surface until the last test interruption at 19,500 hours, followed by a long stretch of continued testing that reached 29,000 hours recently and is still ongoing. This chapter will provide a brief review of the test methodology and results review, followed by a status update on the current running phase.

4.2 Experimental

4.2.1 Specimen Preparation

While constant load test provides an efficient way to assess the effects of various influencing factors on SCC initiation by testing a large number of tensile specimens simultaneously, BNCT test was selected for this study as it enables specimens to be prepared in a site-specific fashion with the notch positioned in region(s) of interest. As shown in Figure 53, standard 0.5T CT specimen geometry is used, but the notch tip was wet ground to a ~0.75 mm radius using a diamond wheel. The notch surface was then manually polished to a 1 μm finish. This created a well-controlled surface closely matching the surface condition for the tensile initiation specimens. Crack initiation can be better resolved by SEM examinations of the notch for the polished surface and compared to in-situ DCPD measurements.
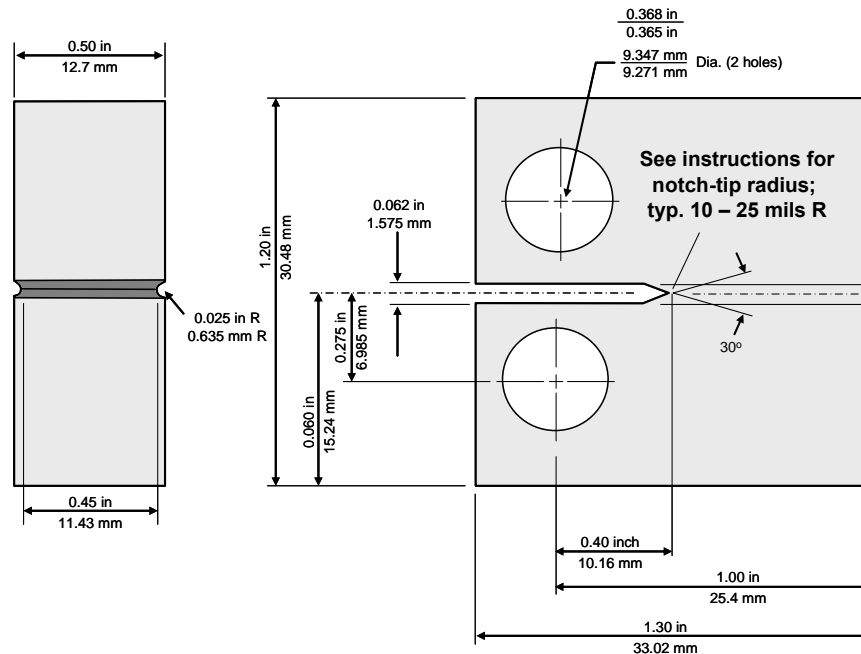
Figure 53. Dimensions of the 0.5T BNCT specimen. The notch radius is ~0.75 mm for all specimens.

Two BNCT specimens were prepared from two dissimilar metal weld mockups made by EPRI to specifically introduce DDC in Alloy 52M. CT148 is machined from an EPRI WRTC 316L/52M/152/low alloy steel (LAS) V-groove weld and CT149 is from an EPRI Alloy 52M mockup. Prior to the test, the distribution of DDC in both welds were carefully mapped in SEM to facilitate determination of the notch location. The EPRI WRTC Alloy 52M-316L weld exhibited a high density of IG cracks in the Alloy 52M weld metal near the Alloy 152 interface, where the notch of CT148 is located (Figure 54). As presented in Figure 54b, a number of DDC cracks greater than 1 mm in length within ~0.5 mm of the Alloy 152 interface were seen in this region and the notch bottom is positioned with the aim to intersect one of the longest cracks. After the specimen was machined, the side grooves were polished and etched for OM/SEM examinations to verify the notch position. As confirmed in Figure 55, the notch successfully intersected a long crack at its bottom along a solidification grain boundary that aligns well with the anticipated growth direction (i.e. perpendicular to the load direction). In addition, the blunt notch was polished to a 1 μm diamond finish and SEM-BSE imaging was employed to document the initial distribution of cracks on the surface that will be exposed to high-temperature PWR primary water during testing. The presence of IG cracks of ~50 μm in length can be seen in many regions on the CT148 blunt notch surface with several regions revealing cracks >100 μm in length (Figures 56 and 57). The hope is that these can be effectively located and characterized after long-term testing to determine whether any additional cracking would occur.
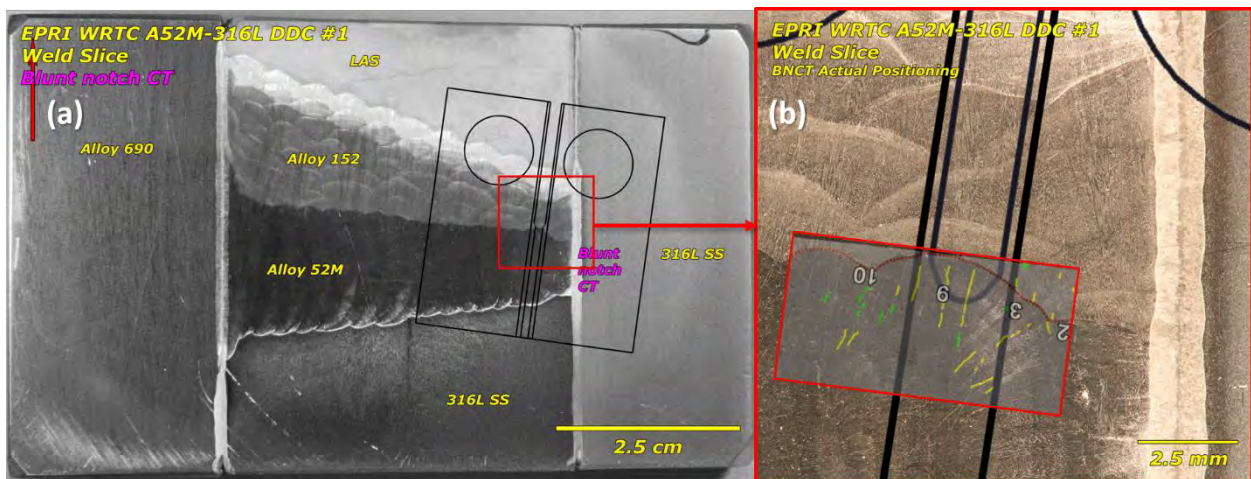
Figure 54. (a) Micrograph illustrating the blunt notch position for CT148, the EPRI WRTC 52M-316L V-groove weld with DDC specimen. (b) A zoom-in micrograph of the location of the notch with respect to pre-test SEM characterizations of DDC distributions (obvious cracks marked in yellow and possible cracks marked in green) in this weld.
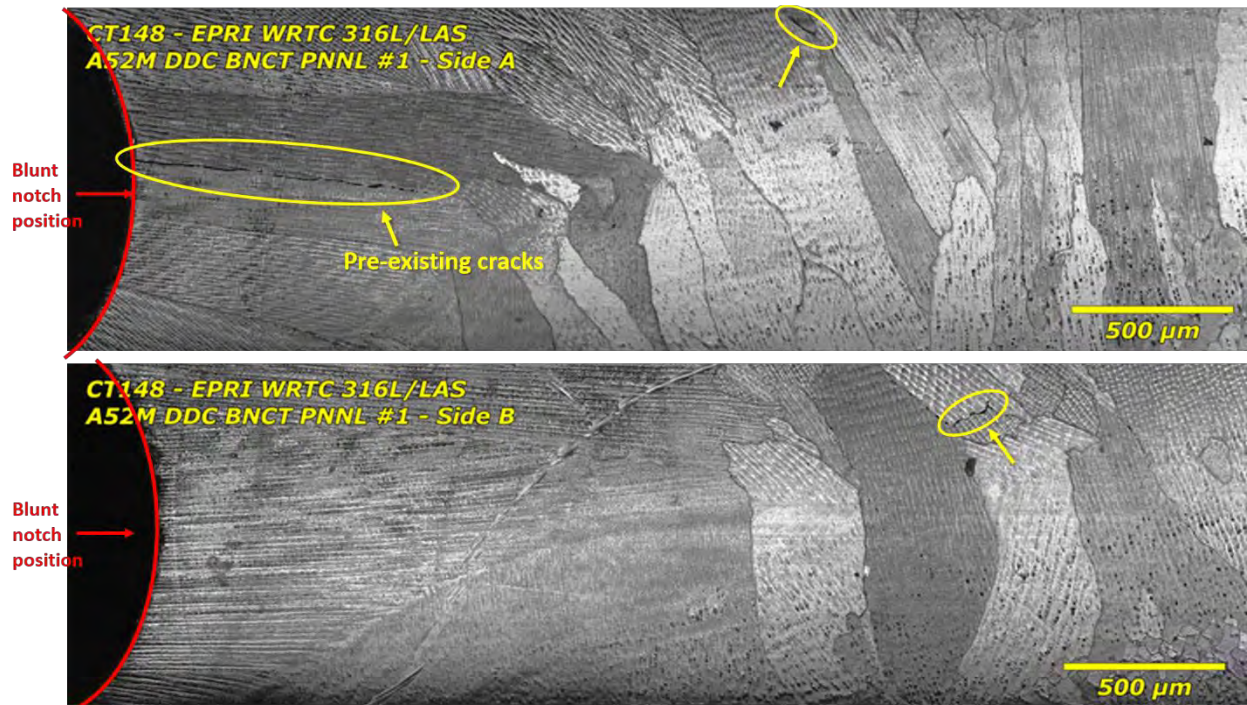
Figure 55. Micrographs revealing cracks identified in the side groove of CT148 just below the notch. The side groove surface was lightly etched for better visualization of solidification grain boundaries.
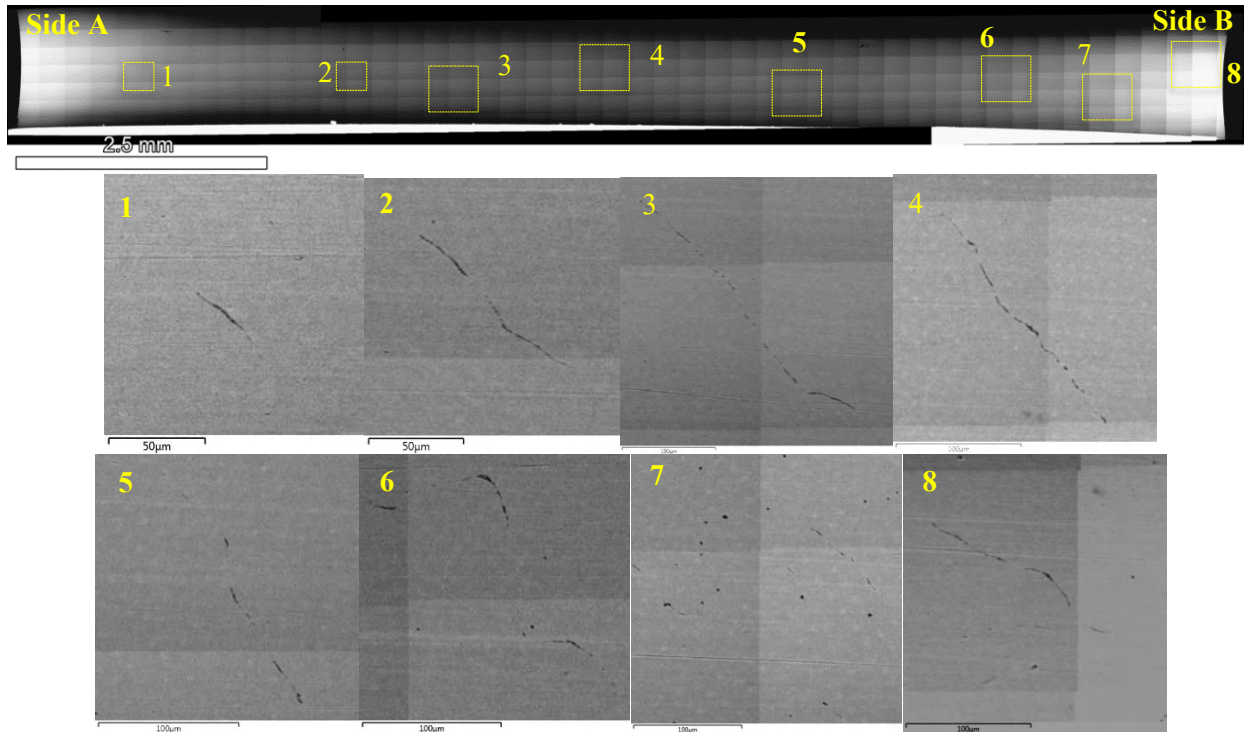
Figure 56. SEM-BSE low magnification montage image of the pre-test blunt notch surface of CT148 with examples of regions containing pre-existing DDC.
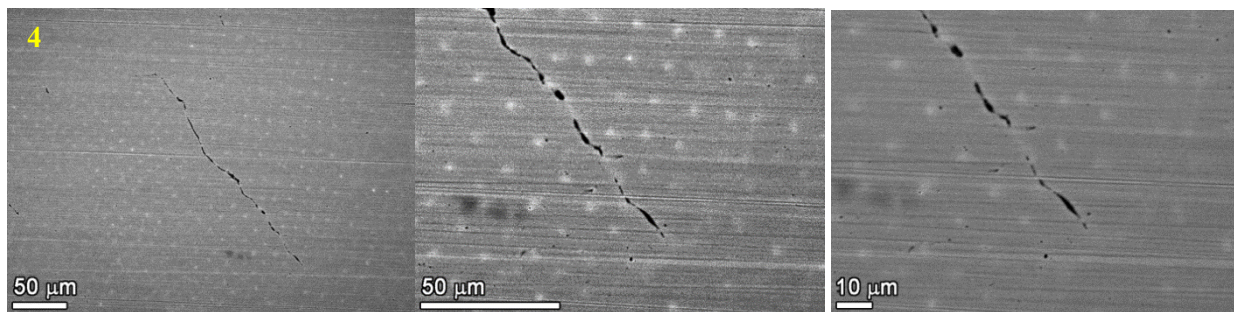
Figure 57. SEM-BSE high magnification micrographs of Region 4 in Figure 56 illustrating the DDC is along a solidification grain boundaries (SGBs). The bright intensity of the Nb signal segregation highlights two different grain orientations on either side of the crack.

The same approach was used to determine the notch position of the EPRI Alloy 52M DDC mockup specimen CT149. The WRTC 52M DDC mockup weld applied refuse passes in an attempt to create DDC cracks and this was partially successful. However, the density and size of these weld cracks were quite small. Several regions were mapped and the maximum number and size of DDC cracks was found within the areas identified by a yellow box overlaid in Figure 58b. As shown in Figure 58, the position of the notch is targeted to intersect the region with the most DDC, but SEM examination on the machined specimen only revealed sporadic and small DDC cracks in the side grooves (Figure 59) and some other possible defects represented by aggregations of dotted precipitates in the blunt notch surface (Figure 60). This illustrates the difficulty in intersecting a meaningful density of small pre-existing defects in this weld. However, since the solidification grain boundaries are properly aligned in the side grooves of the specimens, the decision was made to test this specimen together with CT148.
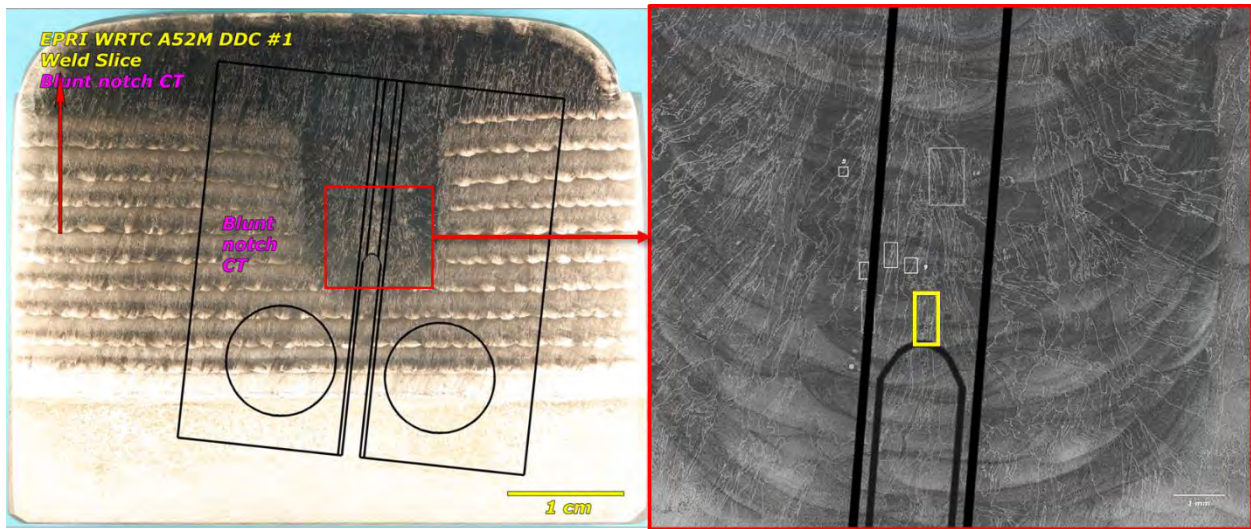
Figure 58. (a) Micrograph illustrating the blunt notch position for CT149, the EPRI WRTC Alloy 52M DDC Mockup specimen. (b) A zoom-in micrograph of the notch location.
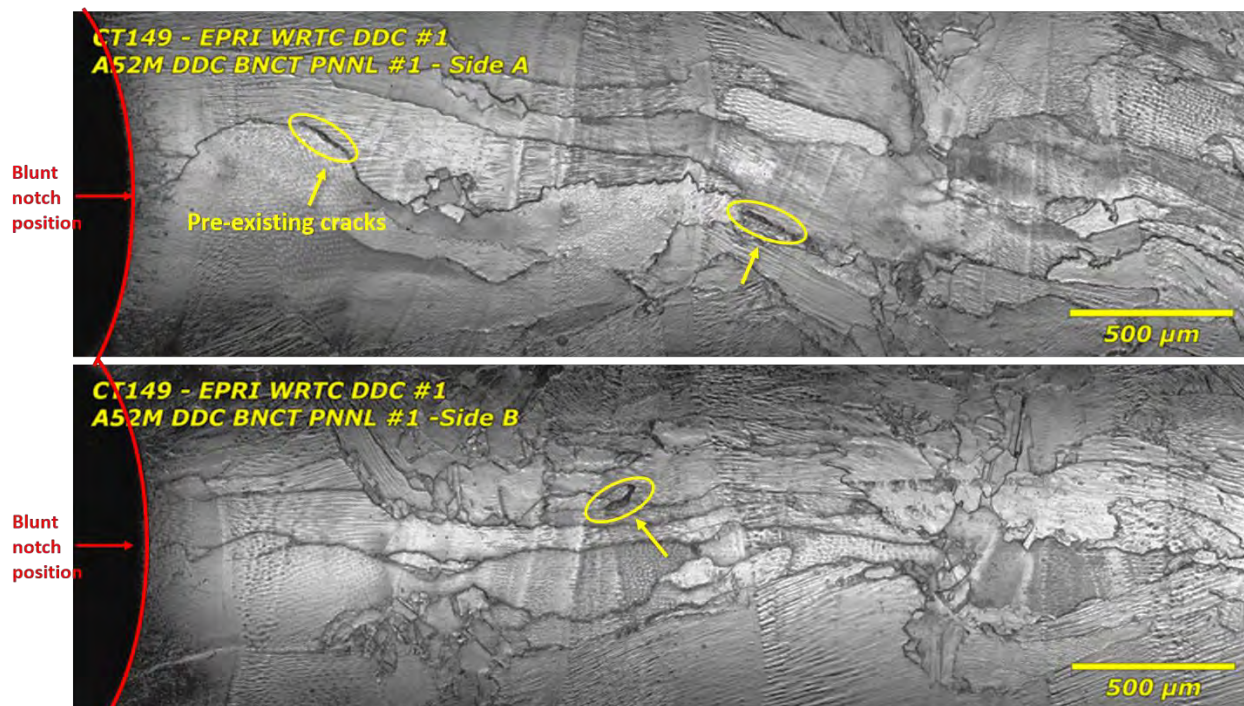
Figure 59. Micrographs revealing cracks identified in the side groove of CT149 just below the notch.
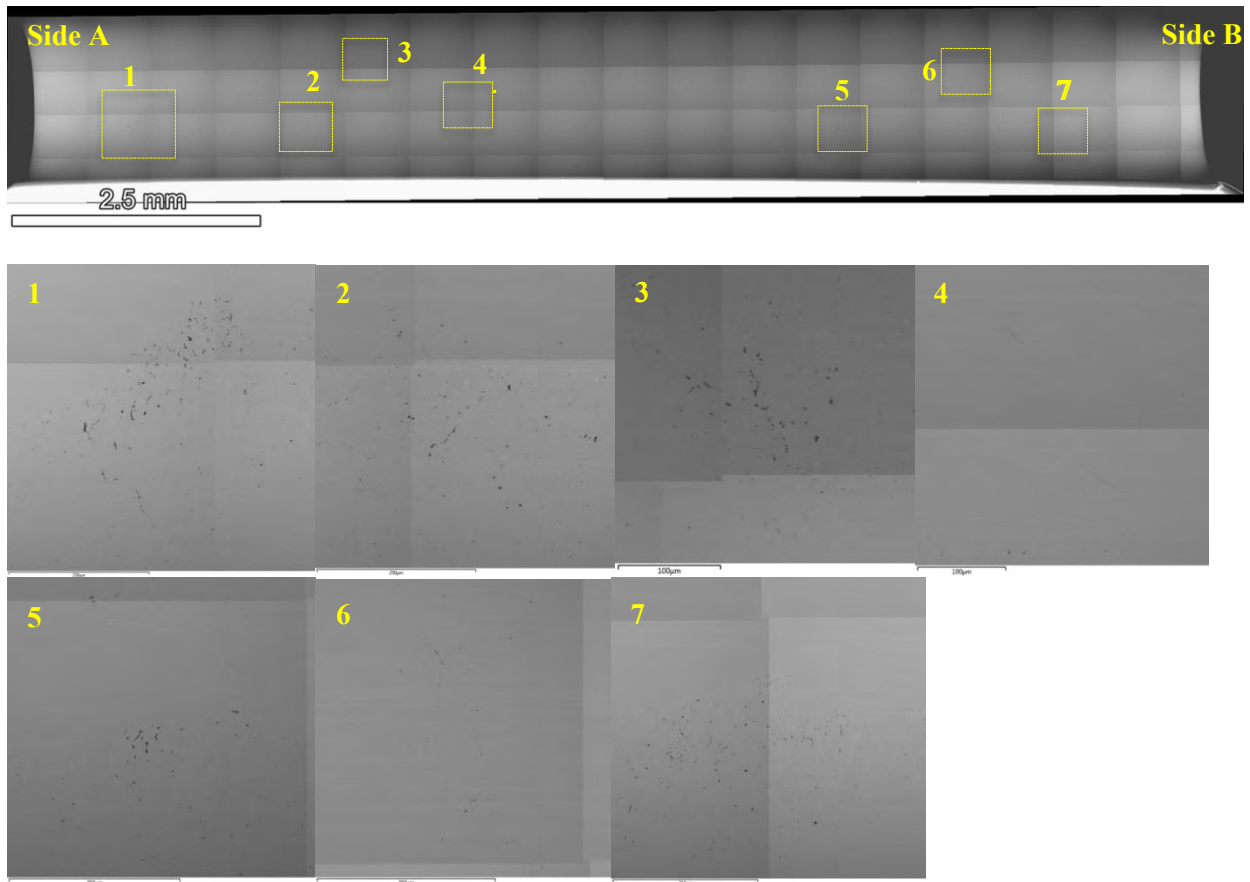
Figure 60. SEM-BSE montage image of the pre-test blunt notch surface of CT149 showing possible regions of pre-existing DDC cracking and defects intersecting the surface.

4.2.2   Test Method

The two BNCT specimens were loaded in series in an NRC SCC test system equipped with active load control via a high-precision servo-electric load control system and in-situ monitoring using DCPD. The test environment simulates PWR primary water (1000 ppm of boron, 2 ppm of lithium) at 360°C and 20.4 MPa with a dissolved hydrogen content of 25 cc/kg to maintain a corrosion potential at the Ni/NiO stability line. The test has been primarily conducted at constant load with high stress intensity (K) levels in the attempt to initiate or grow SCC from existing DDC cracks, including two load raises and a few load cycles which will be detailed later. Since the blunt notch was slightly longer in CT148 to better intersect DDC cracks, the applied load produced a slightly higher estimated K level in CT148 than in CT149. These K levels are better described as a "pseudo K" as they are calculated assuming a tight crack is present across the specimen versus a blunt notch with a smooth surface. The DCPD measurement of crack length is different for the blunt notch specimens because growth from a sharp crack is probably not occurring.

To document the evolution of pre-existing defects on the notch surface and to verify DCPD response, the test was stopped every ~4,000 hours for detailed SEM examinations for the first 19,500 hours of the test. In addition, a thin slice was removed from Side B at 3,810 hours and again from Side A at 16,000 hours in both specimens for detailed characterizations of crack distribution and morphology in the cross-sections.

4.3 Precursor Damage Evolution on Specimen Notch Surface: Previous Characterization Results

As mentioned in Section 4.2.2, the test was stopped every ~4,000 hours for detailed SEM examinations to document the evolution of pre-existing defects on the notch surface and verify DCPD response, with the last stop taking place in April 2021 when the total exposure time reached 19,500 hours. Routine SEM examinations were performed on the notch surface and the side grooves of the specimens

An overview of the evolution of notch surface morphology in CT148 is provided in Figure 61. Higher magnification SEM-BSE images at selected sites obtained at each test interruption are also presented in Figure 62. Several pre-existing DDC were observed (marked in green in Figures 61 and 62) on the blunt notch surface before the SCC test. After 3,810 hours of exposure at constant load, a few more small cracks formed (highlighted in yellow), followed by little growth of existing cracks at 8,000 hours with the formation of more minor cracks (highlighted in red in Figures 61 and 62). No obvious change was found after 12,000 hours of exposure. The load was increased by 5% twice at 13,000 and 15,000 hours, but the observation after 16,000 hours of exposure still did not reveal any change in surface crack morphology. A similar situation was again found after 19,500 hours, where the load was further increased with the implementation of periodic load cycles to compensate for stress relaxation around the notch region during the latest test period.

The other blunt notch specimen CT149 from the EPRI Alloy 52 DDC weldment did not exhibit obvious cracks on the notch surface before the test. SEM characterizations were performed on the notch surface at each test interruption and only revealed the formation of a few crack-like features at ~3,810 and 8,000 hours (Figure 63). High-magnification images of these cracks are provided in Figure 64, where discontinuous welding defects on the order of tens of micrometers were revealed. Unfortunately, as shown in Figures 63 and 64, Fe-Ni-rich spinel oxides were continuously deposited onto the notch surface of CT149 during the interim of the test, gradually forming a thick oxide layer after 19,500 hours of exposure. These surface oxides obscured clear identification of precursor damage and crack distributions on the surface. Therefore, it is impossible to unambiguously determine the extent of new crack formation and crack growth after the latest testing period, although it is believed that any opened cracks should be visible through the thick oxide layer if their sizes are sufficiently large. Results of these notch surface observations after every test interruption performed to date are summarized in Table 11 to facilitate the comparison of crack evolution in these two specimens as a function of time.
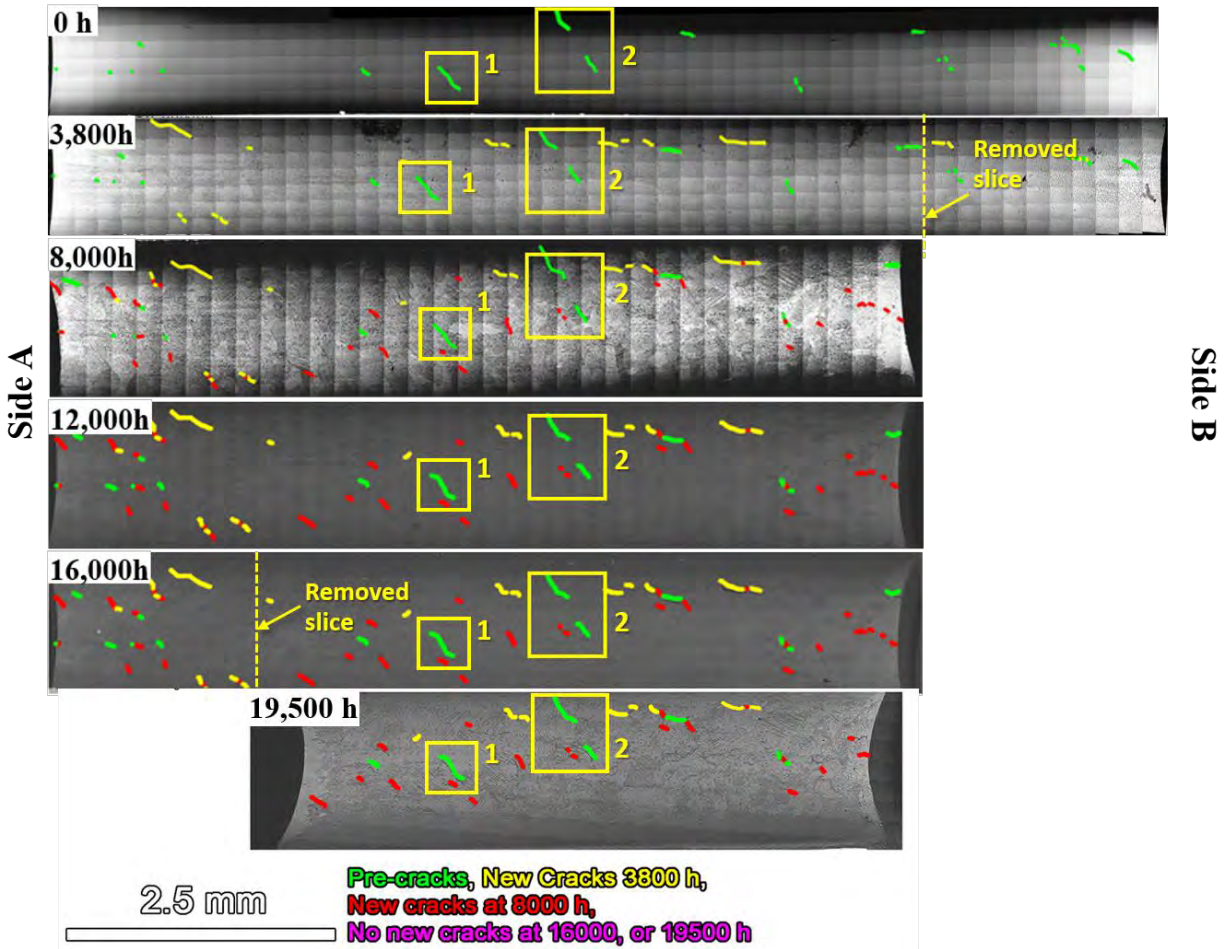
Figure 61. SEM-BSE montage imaging of the evolution of cracks on the blunt notch surface of CT148 from the EPRI WRTC A52M-316L-1 V-groove weld during the 19,500 hours of exposure at high stress in 360°C simulated PWR primary water. Side A is always presented on the left and side B on the right.
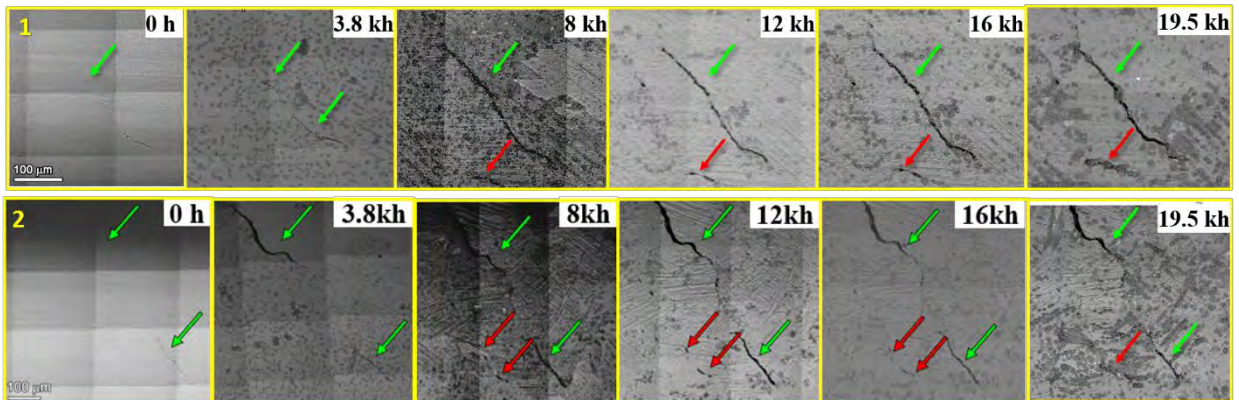
Figure 62. Higher magnification SEM-BSE image showing the evolution of cracks over ~16,000 hours of exposure in regions 1 and 2 highlighted in Figure 61 in the notch surface of CT148. Green arrows indicate pre-existing cracks and red arrows indicate cracks observed at 8,000 hours of exposure.
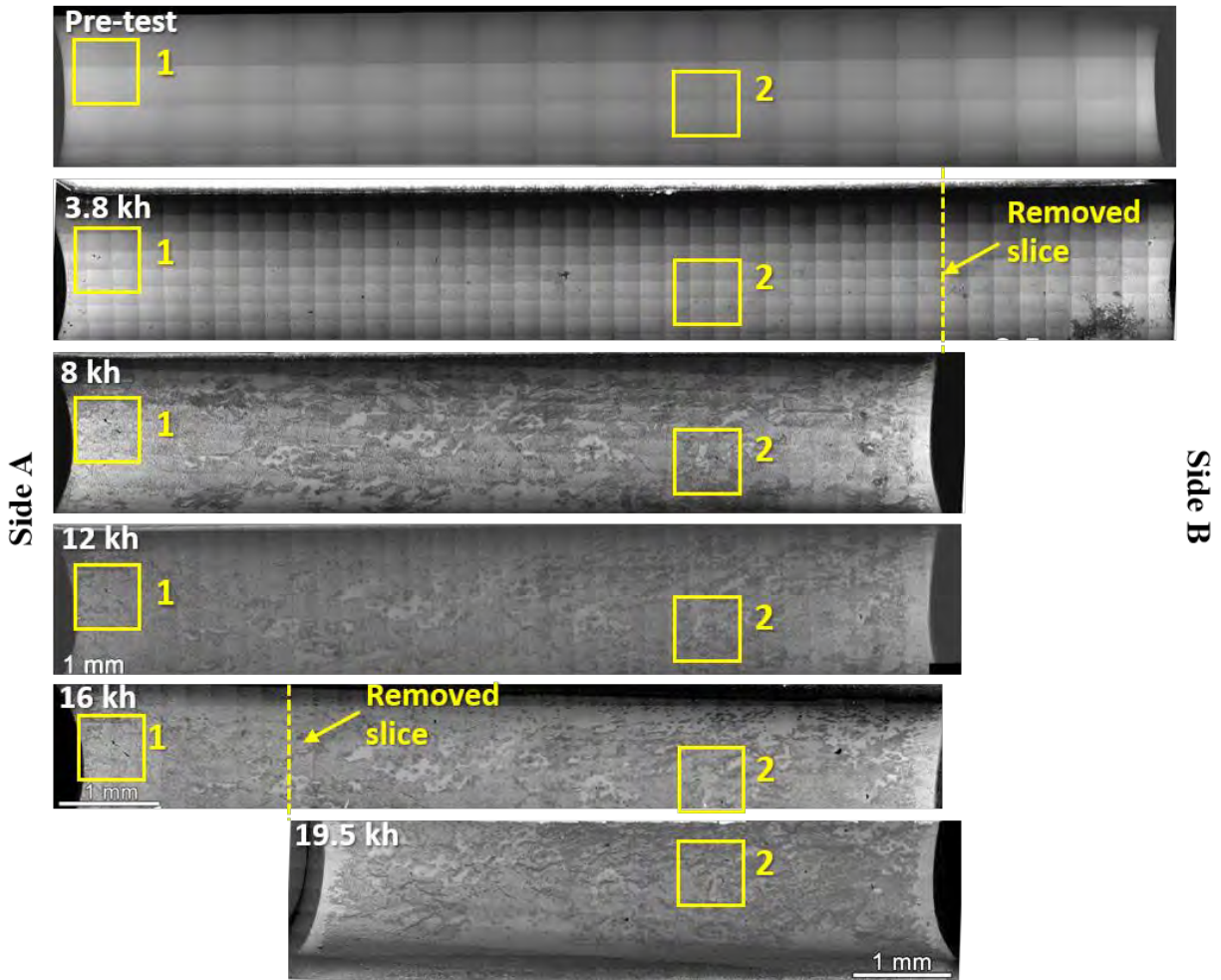
Figure 63. SEM-BSE montage imaging of the evolution of cracks on the blunt notch surface of CT149 from the EPRI A52 DDC weldment during the 19,500 hours of exposure at high stress in 360°C simulated PWR primary water. Side A is always presented on the left and side B on the right.
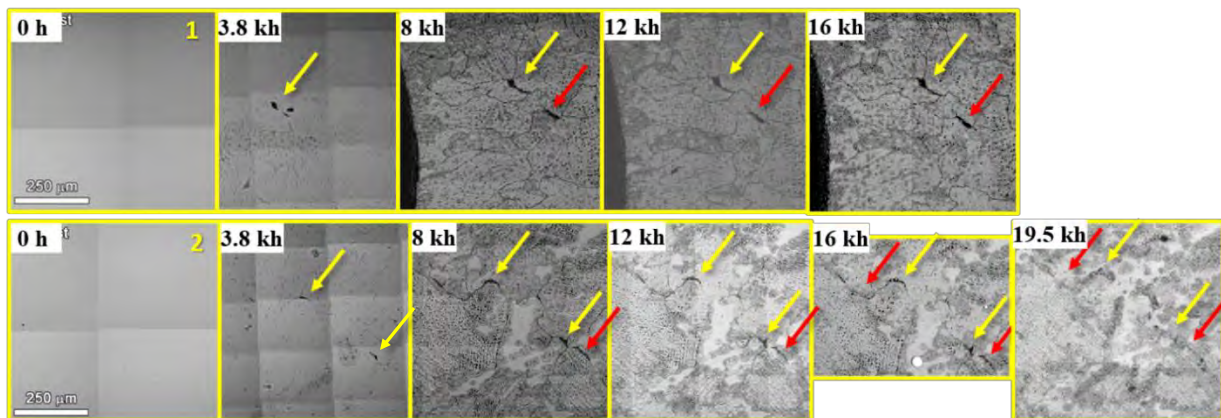
Figure 64. Higher magnification SEM-BSE image showing the evolution of possible cracks during the 19,500 hours of exposure in regions 1 and 2 highlighted in Figure 63 in the notch surface of CT149. Yellow arrows indicate cracks observed at 3,810 hours and red arrows indicate cracks observed at or after 8,000 hours.

Table 11. Summary of the evolution of cracking morphology observed by SEM on the notch surface of CT148 & 149 after each test interruption.

SEM Results Exposure Time	CT148 (EPRI DMW WRTC-52M-316L-1 V-groove DDC)	CT149 (EPRI A52 DDC Weldment)
0 hours	Several DDCs (10–100s μm long) found on notch surface	No DDCs found on notch surface
3,810 hours	Some new cracks (10–100s μm long) formed with minor growth (opening up) of existing cracks	A few minor precursor IG damage features (<10 μm long) developed on the surface
8,000 hours	More new cracks (generally <100 μm long) formed with most existing cracks opened up wider or linked together	Slight growth of minor precursor damage to short cracks of ~50 μm long. No new crack formation.
12,000 hours	No new crack formation or obvious growth of existing cracks	No new crack formation or obvious growth of existing cracks
16,000 hours	No new crack formation or obvious growth of existing cracks	No new crack formation or obvious growth of existing cracks
19,500 hours	No new crack formation or obvious growth of existing cracks	Thick oxide layer formed on the surface obscuring a clear identification of crack distribution, but likely no or only minor new crack formation or growth of existing cracks

4.4   Specimen DCPD Response: FY 2024 Update

An overview of the non-reference corrected DCPD-based crack length response is provided in Figure 65. Both specimens exhibited a decreasing DCPD-indicated CGR over time, more rapid at the early stages of the test (<12,000 hours) and gradually slowed down as the test progressed. Since finite element modeling results predict that creep will cause the stress in the notch region to drop by as much as 20%, the applied load was increased by 5% at test times of 13,000 and 15,000 hours as identified in Figure 65. A very small immediate jump in the DCPD estimated crack length was observed with these load increases, but no detectable change was observed in the subsequent CGR. Therefore, at the beginning of the last testing phase starting from 16,000 hours, the K level was further increased to ~49.8 MPa√m in CT148 and ~46.2 MPa√m in CT149. In addition, one 980s/20s load cycle with an R ratio (i.e., K_{max}/K_{min}) of 0.3 was implemented every 280 to 500 hours. This is another means we tested to maintain a relatively stable stress around the blunt notch to compensate for stress relaxation in the crack tip region due to creep. The cycling condition was determined to avoid producing significant fatigue crack extension. A total of five individual load cycles were implemented over an interim of 2000 hours. No measurable crack extension occurred immediately after any of the load cycles, and no measurable increase in CGR was found in either specimens. More details regarding this exercise can be found in [25]. The test was stopped after reaching 19,500 hours in March 2021 for another round of specimen examination. As summarized in Section 4.3, no new crack formation or growth of existing cracks was seen on the notch surface, which is consistent with the specimens' DCPD response.

The current phase of testing began in late April of 2023. The long gap between these two testing phases was due to (1) test system availability and (2) our multiple attempts to document the depth profile of the cracks observed on the specimen notch surface using non-destructive three-dimensional X-ray computed tomography (XCT). A number of different XCT instruments and scan methods were experimented at both PNNL and external services. Unfortunately, none was able to provide satisfactory

results due to the challenging geometry of the specimens as they are too thick to allow enough signals to be collected.

At the restart of the test, the specimens were loaded to the same estimated K values used in the previous test phase, i.e., 49.8 MPa√m for CT148 and 46.2 MPa√m for CT149. One task performed during this testing phase is to quantify the contribution of electrical resistivity evolution to the non-referenced DCPD-indicated crack extension. There are two major contributors to the change in DCPD response. The first is crack growth since propagation of the crack will change the cross-sectional surface area being monitored and reflected in DCPD as a change in electrical resistance. The other is electrical resistivity evolution due to microstructural aging during high-temperature exposure. This is a known phenomenon for Ni-base alloys 600/690 and their weld metals, which will lead to a decreasing DCPD propagation rate over time. This latter component usually can be corrected by monitoring the resistivity change in low load region away from the notch where no crack is present, but this is only applicable to specimens made of uniform material but not specimens containing different materials like these two BNCT specimens machined from dissimilar metal weld mockups. This is also the reason for using the non-referenced DCPD response to track specimen behavior in this test. Since the specimens have already undergone long-term exposure in simulated primary water, it is assumed that the electrical resistivity evolution of these materials has dwindled. However, it would be helpful to double-check so we can better interpret the DCPD data. As shown in Figure 66, once the CGRs of the two specimens under high load were established after the first ~1000 hours of exposure of the restart of the test, the load was dropped to a very low value at 20408 hours and held for ~900 hours. No contribution due to crack growth to the DCPD signal should occur at the low load condition. Therefore, electrical resistivity drift is believed to fully account for any CGRs estimated during this period. Interstingly, the CGR values of CT149 remained almost constant across the low load period and the high load periods preceding and following it (Figure 66), suggesting the measured non-reference DCPD CGR is primarily due to electrical resistivity evolution. As a result, CT149 exhibited essentially no crack growth. Meanwhile, the CGR of CT148 during the low load period was more than >50% lower than those measured during the high load periods before and after it, indicating a crack growth-related component is still involved in the measured CGRs in CT148. Nevertheless, given that the absolute CGR values are extremely low (less than 1×10^{-9} mm/s), the actual crack growth is considered to be negligible.

Given the very low CGRs measured during the new testing phase and the fact that the SEM examination at 19,500 hours observed no crack growth in either specimen, it was decided to continue the test without stopping it again after reaching another 4,000 hours. At the time of this writing, the test has just reached 10,000 hours of exposure during this phase and is still ongoing. As shown in Figure 67, a small strain jump occurred in CT149 at ~26,480 hours, indicating a small ligament break-up inside the specimen. Nevertheless, the CGR dropped afterward (from ~1.0×10^{-9} and 7×10^{-10} mm/s), suggesting that the strain jump did not lead to sustainable crack growth. In the meantime, the CGR of CT148 remained extremely low in the ~4–5×10^{-10} mm/s range. The next step of this test will be determined in collaboration with NRC, and new results will be reported in the future.
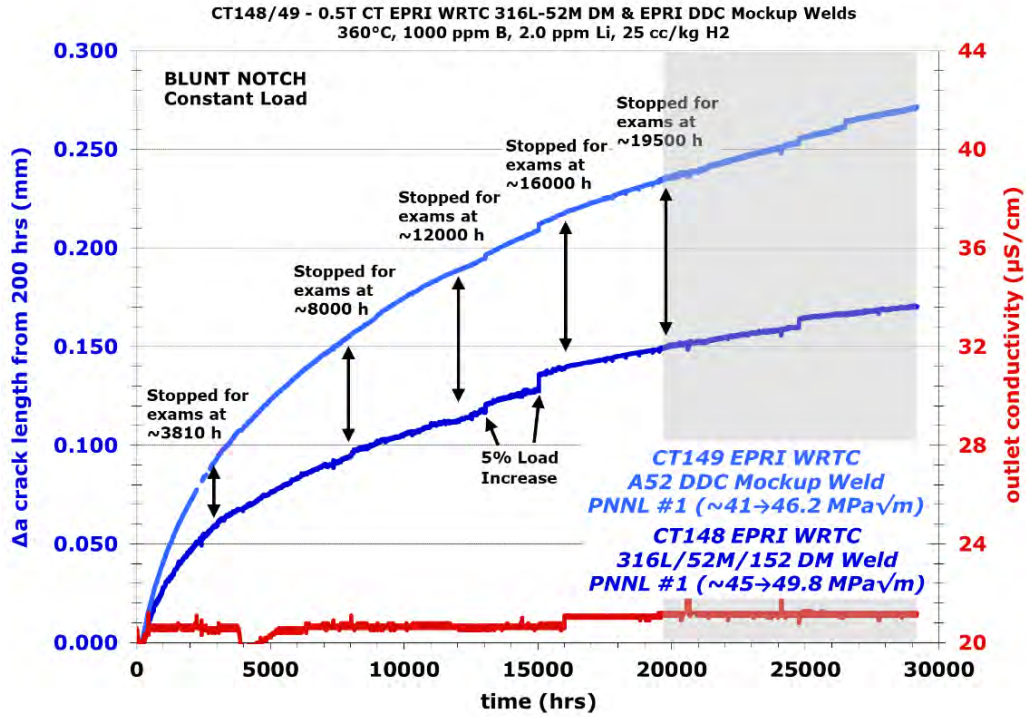
Figure 65. Overview of the non-referenced DCPD-estimated crack length for the two BNCT specimens CT148 and CT149 tested at constant load in 360°C simulated PWR primary water. Current test phase (ongoing) is shaded in light grey.

Figure 66. 1ˢᵗ part of the non-referenced DCPD-estimated crack length during the current test phase for the two BNCT specimens CT148 and CT149 tested at constant load in 360°C simulated PWR primary water.

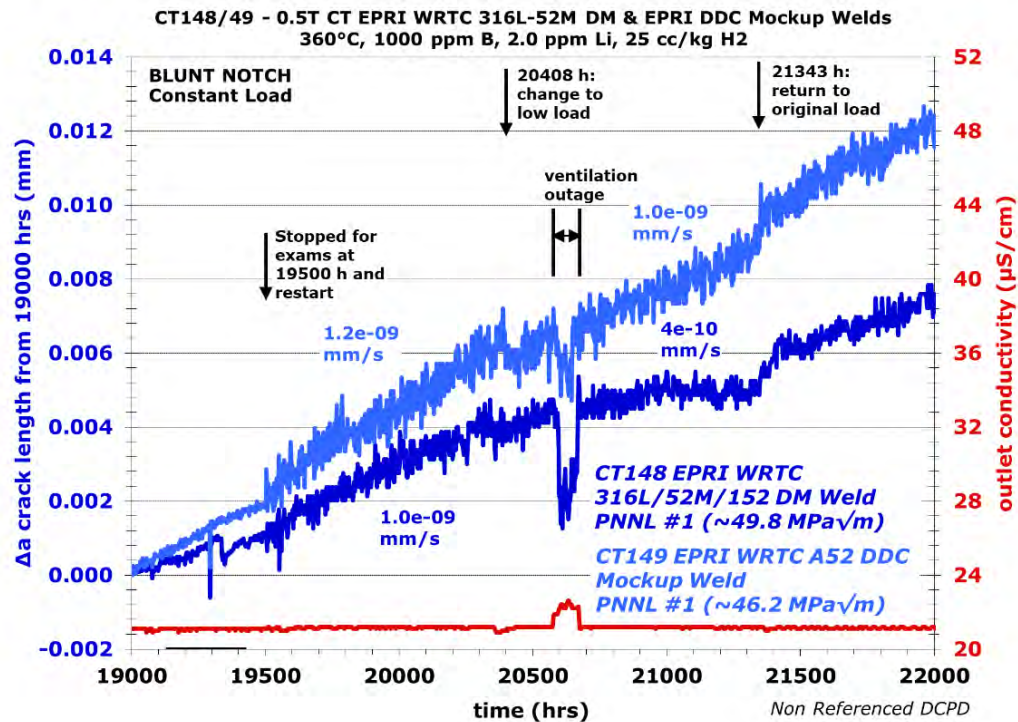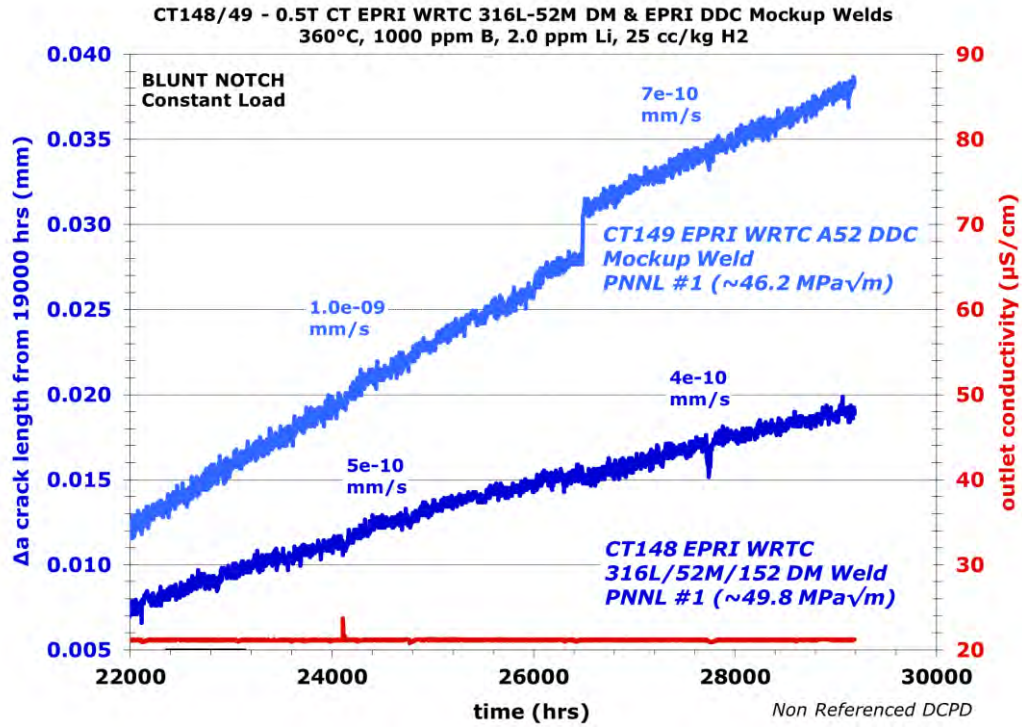Figure 67. 2nd part of the non-referenced DCPD-estimated crack length during the current test phase for the two BNCT specimens CT148 and CT149 tested at constant load in 360°C simulated PWR primary water.

5.   Summary

This report summarizes the progress made from October 2023 to June 2024 on SCC initiation and air creep testing of CW Alloy 690 using tensile specimens and SCC initiation testing on high-Cr weld metals Alloy 52/52M mockups using BNCT specimens.

The first part of this report provides a status update on the ongoing Phase V SCC initiation testing on CW Alloy 690 materials in 360°C simulated PWR primary water, where the effects of various material and environmental factors on the long-term GB degradation and crack initiation behavior are being evaluated on forty Alloy 690 specimens from seven commercial Alloy 690 heats. Macroscopic crack initiation was detected in a new Alloy 690TT heat in 31%CF condition after 4.7 years of testing at yield stress. This material also features a semi-continuous distribution of IG carbides, and creep-induced GB cavities have been confirmed to be the root cause for crack initiation. This data point complements the initiation time data obtained during previous testing from three other Alloy 690TT heats following the same mechanism, and an obvious trend is revealed: for highly CW Alloy 690TT materials featuring a susceptible GB microstructure to creep cavity formation, their crack initiation time seems to be primarily dependent on applied stress. As shown in Figure 68, for specimens from different Alloy 690TT heats and tested at their corresponding YS, crack initiation time increased with the decrease in material strength. A preliminary power law fit was performed on these initiation data, leading to a stress exponent of ~7 for the crack initiation time in 31%CF Alloy 690TT materials tested at 100% YS. The test is continuing, and adjustments will be made in the future if new initiation data is obtained. Another important task pertaining to the long-term SCC initiation testing is the collaboration with EPRI on the long-term aging evaluation of LWRS Alloy 690 specimens using SXRD. Two commercial Alloy 690TT heats with variation in exposure time, cold work level, and thermal-mechanical history and one Ni-30Cr binary model alloy in SA+20%CF condition were selected for this analysis. The analysis is yet to be completed for all specimens, but the initial results only confirmed the LRO phase in an SA+20%CF Ni-30Cr binary specimen, while the Alloy 690 specimens showed indications of short range ordering. Both SXRD measurements and data analysis are underway, with the aim to not only evaluate LRO phases but also to quantify the evolution of precipitates, lattice parameters, and microstrain evolution as a function of time to provide a more comprehensive understanding of Alloy 690 aging in service.
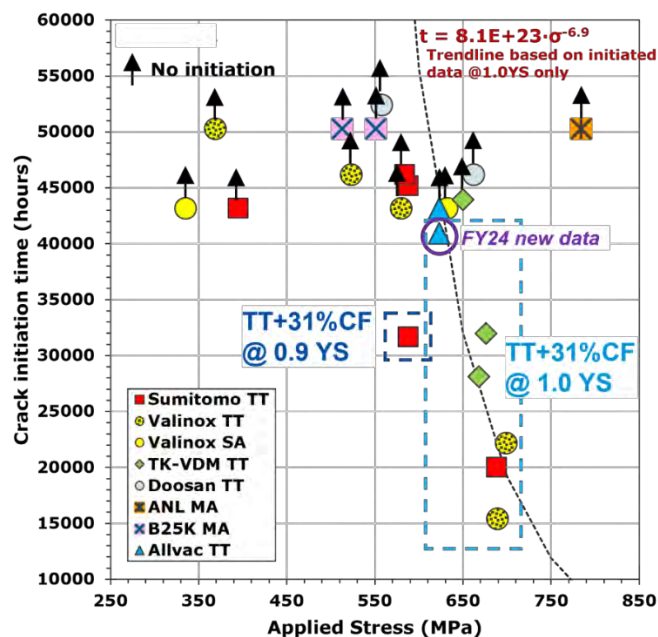
Figure 68. Crack initiation time of CW Alloy 690 tested in 360°C simulated PWR primary water as a function of applied stress.

The second part of this report summarized the testing and characterization results for the 1st-year creep testing of CW Alloy 690 specimens in 330, 360, and 400°C air. The objective of this testing is to better understand the mechanism and kinetics of creep-induced cavity evolution and to accelerate data collection for predicting the long-term behavior of Alloy 690 in service. Two Alloy 690TT heats known for their high susceptibility to creep cavity formation were selected for this study. One heat was tested in three CF conditions (12, 21, and 31% reduction in thickness), and the other heat was tested in a single 29% CTS condition. The materials are tested at their corresponding YS at each specific temperature. The tests are performed in deadweight creep test systems equipped with in-situ DCPD measurements of creep rates and crack initiation time. Figure 69 summarizes the steady-state creep strain rates estimated by non-referenced DCPD data on all specimens, showing that the steady-state strain rates increased with increasing cold work level and applied stress at every temperature, consistent with expected creep behavior. After completion of the 1st-year exposure, all specimens were removed from tests for detailed SEM/FIB characterization to document IG damage. Obvious IG cracks were first found in Alloy 690 TT+31%CF specimens tested at 360°C after ~9,000 hours, and prevailed in the same material in all cold forge levels tested at 400°C after the same exposure time, of which the density increased rapidly with the increase in cold work. All cracks were confirmed to be formed due to the coalescence of creep-induced GB cavities, and macroscopic crack initiation occurred in all three TT+31%CF specimens tested at 400°C within 2,000 hours of exposure. These initiation data were plotted with crack initiation times of similar material measured in 360°C primary water for a preliminary fit for the Arrhenius equation. The result suggests a thermal activation energy of ~215 kJ/mol·K for creep-induced crack initiation in Alloy 690TT+31%CF materials (Figure 70).
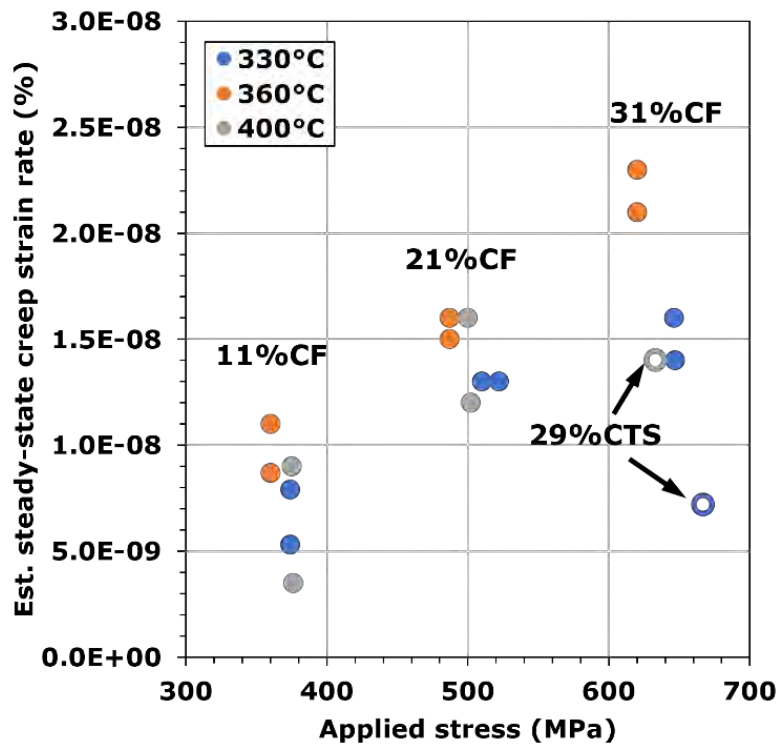
Figure 69. Steady-state creep strain rates estimated using the last 2000 hours non-referenced strain rate measured by DCPD in the creep tests. The closed symbols are for CF Valinox WP142 Alloy 690TT specimens, and the open symbols are for CTS Valinox RE243 Alloy 690TT specimens.
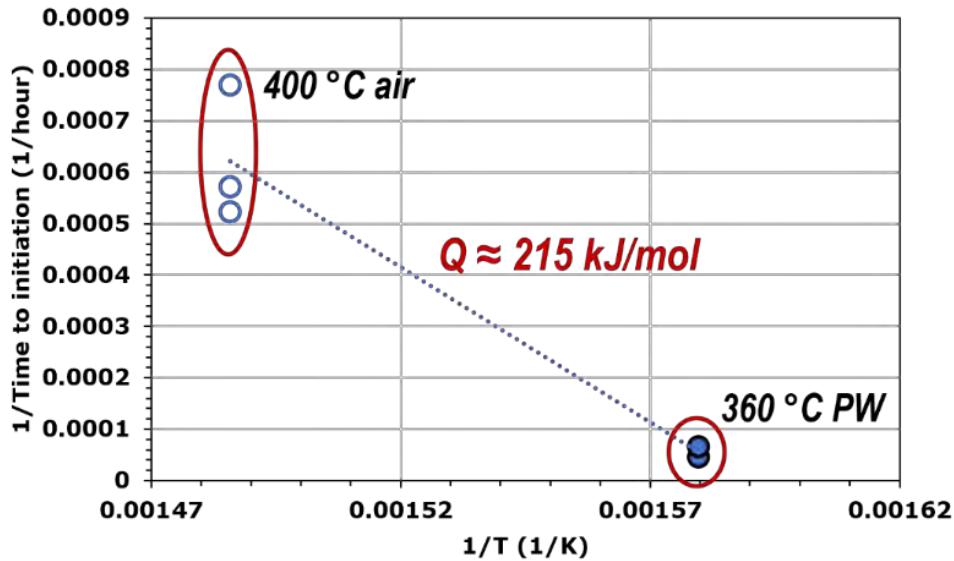
Figure 70. Thermal activation energy estimated using the crack initiation time data measured by DCPD in 400°C air and 360°C primary water fromValinox TT+31%CF specimens.

The third part of this report gave an update on the long-term SCC initiation testing performed in collaboration with NRC on two blunt notch compact tension specimens machined from DDC-containing Alloy 52/52M weld mockups. The test is designed to evaluate the role of pre-existing weld defects on SCC initiation and growth in high Cr, Ni-base weld metals Alloy 52 and 52M. The test has recently reached 29,00 hours and is still ongoing due to the high value in obtaining long-term exposure data on Alloy 52/52M. DCPD-indicated CGR remained negligibly low for both specimens even after increased load or load cycles to compensate for creep-induced stress relaxation around the notch region. The lack of crack growth is consistent with the high SCC resistance known for these high-Cr Ni-base weld metals.

References

[1] Z. Zhai, M.B. Toloczko, M.J. Olszta, S.M. Bruemmer, Stress corrosion crack initiation of alloy 600 in PWR primary water, Corrosion Science, 123 (2017) 76-87.

[2] M.B. Toloczko, M.J. Olszta, Z. Zhai, S.M. Bruemmer, Stress corrosion crack initiation measurements of alloy 600 in PWR primary water, in: 17th International Conference on Environmental Degradation of Materials in Nuclear Power Systems - Water Reactors, Canadian Nuclear Society, 2015, pp.

[3] Z. Zhai, M.J. Olszta, M.B. Toloczko, S.M. Bruemmer, Summary of Stress Corrosion Crack Initiation Measurements and Analyses on Alloy 600 and Alloy 690, Pacific Northwest National Laboratory: Technical Milestone Report M2LW-15OR0402034, Light Water Reactor Sustainability Program, DOE Office of Nuclear Energy, September 2015.

[4] K. Arioka, 2014 Whitney Award Lecture: Change in Bonding Strength at Grain Boundaries before Long Term SCC Initiation, Corrosion (Houston), 71 (2015) 403-419.

[5] K. Arioka, T. Miyamoto, T. Yamada, M. Aoki, Role of Cavity Formation in Crack Initiation of Cold-Worked Carbon Steel in High-Temperature Water, Corrosion (Houston), 69 (2013) 487-496.

[6] K. Arioka, T. Yamada, T. Miyamoto, T. Terachi, Dependence of Stress Corrosion Cracking of Alloy 690 on Temperature, Cold Work, and Carbide Precipitation—Role of Diffusion of Vacancies at Crack Tips, Corrosion (Houston), 67 (2011) 035006-035001-035006-035018.

[7] K. Arioka, R.W. Staehle, T. Yamada, T. Miyamoto, T. Terachi, Degradation of Alloy 690 After Relatively Short Times, Corrosion (Houston), 72 (2016) 1252-1268.

[8] Z. Zhai, M. Toloczko, K. Kruska, S. Bruemmer, Precursor Evolution and Stress Corrosion Cracking Initiation of Cold-Worked Alloy 690 in Simulated Pressurized Water Reactor Primary Water, Corrosion (Houston), 73 (2017) 1224-1236.

[9] Z. Zhai, M. Toloczko, K. Kruska, D. Schreiber, S. Bruemmer, Grain Boundary Damage Evolution and SCC Initiation of Cold-Worked Alloy 690 in Simulated PWR Primary Water, in: J.H. Jackson, D. Paraventi, M. Wright (Eds.) Proceedings of the 18th International Conference on Environmental Degradation of Materials in Nuclear Power Systems – Water Reactors: Volume 1, Springer International Publishing, Cham, 2018, pp. 457-483.

[10] Z. Zhai, M.B. Toloczko, K. Kruska, D.K. Schreiber, M.J. Olszta, N.R. Overman, S. Bruemmer, Precursor damage evolution and stress corrosion crack initiation of cold-worked alloy 690 in PWR primary water, Pacific Northwest National Laboratory: Technical Milestone Report M2LW-16OR0402034, Light Water Reactor Sustainability Program, DOE Office of Nuclear Energy, September 2016.

[11] Z. Zhai, M.B. Toloczko, S.M. Bruemmer, Stress corrosion crack initiation behavior of Alloy 600 and Alloy 690 in PWR primary water, Pacific Northwest National Laboratory: Technical Milestone Report M2LW-18OR0402034, Light Water Reactor Sustainability Program, DOE Office of Nuclear Energy, September 2018.

[12] Z. Zhai, M.B. Toloczko, M.J. Olszta, S.M. Bruemmer, Grain boundary microstructure effects on stress corrosion crack initiation mechanisms in Alloy 600 and Alloy 690, Pacific Northwest National Laboratory: Technical Milestone Report M2LW-19OR0402031, Light Water Reactor Sustainability Program, DOE Office of Nuclear Energy, September 2019.

[13] Z. Zhai, M.J. Olszta, M.B. Toloczko, S.M. Bruemmer, Long-term crack initiation behavior of Alloy 690 and its weld metals in PWR primary water, Pacific Northwest National Laboratory: Technical Milestone Report   M3LW-20OR0402037, Light Water Reactor Sustainability Program, DOE Office of Nuclear Energy, April 2020.

[14] M.B. Toloczko, N.R. Overman, M.J. Olszta, S.M. Bruemmer, Pacific Northwest National Laboratory Investigation of Stress Corrosion Cracking in Nickel-Base Alloys, Volume 3: Stress Corrosion

Cracking of Cold-Worked Alloy 690, NUREG/CR-7103 Vol. 3, Nuclear Regulatory Commission, Office of Nuclear Regulatory Research, 2015.

[15] S.M. Bruemmer, M.B. Toloczko, M.J. Olszta, Pacific Northwest National Laboratory Investigation of Stress Corrosion Cracking in Nickel-Base Alloys, Volume 2, NUREG/CR-7103 Vol. 2, Nuclear Regulatory Commission, Office of Nuclear Regulatory Research, 2012.

[16] P.L. Andresen, I.P. Vasatis, F.P. Ford, Behavior of short cracks in stainless steel at 288°C, in: CORROSION 1990, NACE, 1990, pp.

[17] E. Richey, D.S. Morton, M.K. Schurman, SCC initiation testing of nickel-based alloys using in-situ monitored uniaxial tensile specimens, in: 12th International Conference on Environmental Degradation of Materials in Nuclear Power Systems - Water Reactors, The Minerals, Metals & Materials Society, 2005, pp. 947-956.

[18] S.M. Bruemmer, M.J. Olszta, D.K. Schreiber, M.B. Toloczko, Stress Corrosion Crack Initiation of Cold-Worked Alloy 600 and Alloy 690 in PWR Primary Water, Pacific Northwest National Laboratory: Technical Milestone Report M2LW-14OR0404023, Light Water Reactor Sustainability Program, DOE Office of Nuclear Energy, September 2014.

[19] Z. Zhai, M.B. Toloczko, F. Cintron-Colon, R.A. Bouffioux, Evaluation of Stress Corrosion Cracking Behavior of Ni-Base Alloys in PWR Primary Water Containing KOH vs. LiOH, Pacific Northwest National Laboratory: Technical Milestone Report M2LW-21OR0402036, Light Water Reactor Sustainability Program, DOE Office of Nuclear Energy, September 2021.

[20] Z. Zhai, M. Toloczko, F. Cintron-Colon, R.A. Bouffioux, Stress Corrosion Cracking of Ni-Base Alloys in PWR Primary Water Containing KOH vs. LiOH, Pacific Northwest National Laboratory: Technical Milestone Report M3LW-22OR0402033, Light Water Reactor Sustainability Program, DOE Office of Nuclear Energy, July 2022.

[21] Z. Zhai, M.B. Toloczko, FY 2023 Progress on Stress Corrosion Crack Testing of Ni-Base Alloys in PWR Primary Water, Pacific Northwest National Laboratory: Technical Milestone Report M2LW-23OR04020311, Light Water Reactor Sustainability Program, DOE Office of Nuclear Energy, August 2023.

[22] A. Marucco, Atomic ordering in the Ni☐Cr☐Fe system, Materials Science and Engineering: A, 189 (1994) 267-276.

[23] G. Young, J. Tucker, D. Eno, The Kinetics of Long Range Ordering in Ni-Cr and Ni-Cr-Fe Alloys, in: 16th International Conference on Environmental Degradation of Materials in Nuclear Power Systems - Water Reactors, NACE International, 2013, pp.

[24] F. Delabrouille, D. Renaud, F. Vaillant, J. Massoud, Long range ordering of alloy 690, in: 14th International Conference on Environmental Degradation of Materials in Nuclear Power Systems - Water Reactors, 2009, pp. 888-894.

[25] Z. Zhai, M.J. Olszta, M.B. Toloczko, Quantitative Analysis of Precursor Damage and Crack Evolution in Alloy 690 and Its Weld Metals after Long-Term SCC Initiation Testing in PWR Primary Water, Pacific Northwest National Laboratory: Technical Milestone Report M3LW-21OR0402033, Light Water Reactor Sustainability Program, DOE Office of Nuclear Energy, April 2021.

[26] M.J. Olszta, Z. Zhai, S.M. Bruemmer, M.B. Toloczko, Understanding and Assessing Possible Long-Term Aging Effects in Alloy 690 and Its Weld Metals, PNNL-29794, March 2020.